UNIVERSITY OF CALGARY

PS-wave processing in complex land settings: statics correction, wave-mode separation, and migration

by

Saul Ernesto Guevara

A THESIS

SUBMITTED TO THE FACULTY OF GRADUATE STUDIES

IN PARTIAL FULFILLMENT OF THE REQUIREMENTS FOR THE

DEGREE OF DOCTOR OF PHILOSOPHY

GRADUATE PROGRAM IN GEOLOGY AND GEOPHYSICS

CALGARY, ALBERTA

NOVEMBER, 2017

Abstract

This thesis concerns processing issues with elastic waves in complex land settings, characterized by rough topography and geological structures with irregular geometry, and proposes some solutions. It is focused on PS-waves (converted from P to S at the reflection point).

The near-surface layer (NSL) is addressed first. An uphole field experiment using explosive sources, located at a surface 2D-3C seismic line, allowed detailed local analysis of the NSL S-wave velocity (V_S) model. S-waves generated by the sources were identified, from which a local V_S model was obtained. Analogous S-waves were also identified on the surface seismic line (which is not usually expected). Tomographic inversion of S-wave refractions from the seismic line enabled the generation of a NSL V_S model for the complete line. However, because of the line sampling, it lacked the critical low velocity of the shallowest zone provided by the uphole.

Statics correction for PS waves is focused on next. This is a demanding processing effort for PS waves, due to the S-wave properties in the NSL. A new statics correction method is proposed, based on the cross-correlation of traces from adjacent receivers, assuming that the only delay time is the receiver statics. This method, termed CRGS (for Common Receiver Gather Statics), was first tested and validated on synthetic data, after which it was applied to real data with encouraging results. This new method overcomes shortcomings of other methods currently used since, in addition to being automatic, it requires neither velocity information nor identification of PS reflections.

Topography and wave-mode separation are also addressed. A wave-mode separation method is proposed which considers the free-surface effect for a zone with rough topography and lateral variations in its elastic properties. This method was tested on synthetic data with promising results.

Finally, PreStack Depth Migration (PreSDM) methods are tested for PP and PS-waves

in the presence of topography. Two scalar PreSDM methods, Kirchhoff and PSPI (for phase-shift plus interpolation), were implemented. The resulting images on synthetic data with and without wave-mode separation proved their reliability for accurately locating seismic events.

Acknowledgements

This work was made possible by the support in many ways of many people and institutions. It originated when I was an employee at Ecopetrol (Colombia), at the Colombian Petroleum Institute (ICP), by the exploration problems we faced. From the very beginning, I had the support of Nestor Saavedra, at that time the Director of the ICP, to undertaking this uncertain journey. Ecopetrol also provided the data of the Tenerife 3-C project, allowed me to use a modeling software, and authorized me the publication of results. My Supervisor, Dr. Gary Margrave, contributed greatly to this result, especially at some critical points. He also kept me focused as much as he could along the trip through the dense forest of the previous research, and about the language of science, mathematics. Hopefully, I learned from him.

Besides that, the faculty, staff, and students of CREWES (Consortium for Research in Elastic Wave Exploration Seismology) of the University of Calgary, contributed greatly to an appropriate environment for research, starting with Dr. Robert Stewart, who welcomed me back. CREWES supported me in many ways. The computer support from Kevin Hall (and Henry Bland at the very beginning), as much as the opportune advice from Rolf Meir, were essential. Han-Xing Lu and Helen Isaac provided me with valuable processing hints. I also enjoyed interesting conversations with CREWES members such as Peter Manning, Joe Wong, Roy Lindseth, and Pat Daley. Louise Forgues at the very beginning, and Laura Baird along most of the time, contributed with invaluable help and support, even beyond the expectations. I also enjoyed time spent and projects collaborating with CREWES students and postdocs, including Alejandro Alcudia, Maria Fernanda Quijada, Gabriela Suarez, Joanna Cooper, Zaiming Jiang, Faranak Mahmoudian, Liliana Zuleta, Thais Guirigay, Rafael Asuaje, Hassan Khaniani, Raul Cova, Michelle Montaño, Adriana Gordon, Huaizhen Chen and Marie Macquet. The friendship of Babatunde Arenrin was much appreciated.

I also thanks to the Committee members, Drs. Robert Stewart, Cristian Rios, Larry

Lines and Daniel Trad, whose analyzes and comments contributed to a better outcome of my work. I received also enlightening comments from experts like Peter Cary, Richard Bale, Don Lawton, and Eduard Krebes. I also appreciate the proofreading support of Helen Isaac, Dave Henley, Rolf Meier, Roy Lindseth, and Mark Kirtland. William Agudelo from Ecopetrol ICP provided ideas and interesting discussions, besides sharing the Tenerife Project development. Fausto Gomez contributed with analyses. Felix Cordoba, from Numerica Ltda, provided me continuous support with the EcoElas2D modeling software. Gloria Ruiz, from the Colombian Geological Service, provided useful comments. Jorge Monsegny gave me advice on computer issues, from Linux to any other. Carlos Montaña gave me advice and friendship from the beginning of this enterprise. Graziella Grech and Xin-Xiang Li, besides their invaluable friendship, contributed greatly with ideas and geophysical advice.

Finally, my wife Maria Clemencia and my son Lino gave me the support and motivation that made this work possible.

Table of Contents

List of Tables

List of Figures and Illustrations

List of Symbols, Abbreviations and Nomenclature

2-D **:** Two dimensions, bi-dimensional.

2D-3C **:** Two dimensional and with three-component sensors.

3-D **:** Three dimensions, three-dimensional.

3-C **:** Three component, referred to a geophone or seismic sensor.

3D-3C **:** Three dimensional and with three-component sensors.

δ_t Anisotropic δ Thomsen's parameter.

ϵ_t Anisotropic ϵ Thomsen's parameter.

γ_t Anisotropic γ Thomsen's parameter.

γ V_P/V_S ratio.

γ_{eff} **:** Effective V_P/V_S ratio.

γ_0 **:** Zero offset V_P/V_S ratio.

ϕ **:** Angle of a S-wave with the normal to an interface.

λ **:** Wavelength.

λ **:** First Lame's elastic constant for an isotropic medium.

μ **:** Rigidity or second Lame's elastic constant.

ω **:** Angular time frequency (radians/s).

ρ **:** Density.

σ **:** Standard deviation for the gaussian function. In another context, *stress* in one-dimension.

σ_{ij} **:** *stress* in the direction i on the plane normal to j.

θ **:** Angle of a P-wave with the normal to an interface.

AVO **:** Amplitude versus offset method.

c **:** Wave propagation velocity, in a general sense.

C**-wave :** Converted wave P to S (see PS).

c_{ijkl} : General form of the elastic constants for any 3-D medium.

CCP : Common conversion point.

CDP : Common depth point.

CMP : Common mid-point. Can be referred to a trace gather.

CRG : Common receiver. Can be referred to a trace gather.

CRP : Common reflection point.

CSG : Common shot gather.

DMO : Dip Move-out, a correction of seismic events for geological dip.

E **:** Elastic constant for a 1-D medium.

f **:** Frequency in cycles per second (Hertz).

FB : first breaks, the seismic events that arrive first in a trace.

FD : Finite difference method.

FT **:** Fourier transform.

g **:** Receiver location.

$i\ j\ k$ **:** As a subindex, any of the directions x, y or z.

k **:** Wave number (space frequency).

NSL : Near surface layer.

NS-LVL : Near surface low-velocity layer.

NMO : Normal move-out.

PreSTM : Pre-stack Time Migration.

PreSDM : Pre-stack Depth Migration.

PS **:** Converted wave P to S generated at the reflector.

R_P^z **:** Free surface response coefficient in the vertical component for incident P wave.

R_P^x **:** Free surface response coefficient in the horizontal component for incident P wave.

R_S^z **:** Free surface response coefficient in the vertical component for incident S wave.

R_S^x **:** Free surface response coefficient in the horizontal component for incident S wave.

$\underset{\sim}{R}$ **:** Inverse *Tau-p* matrix operator with discrete elements R_{jk}

R_{jk} **:** Discrete element of $\underset{\sim}{R}$, defined as $R_{jk} = e^{i\omega p_j x_k}$.

RT : Ray tracing method.

RMS **:** Root Mean Square value.

s **:** Source location.

S **:** Shear or secondary wave.

t_0 **:** Zero offset time for a seismic reflection trace gather.

V_C **:** PS-wave NMO velocity.

V_P **:** P-wave velocity.

V_S**:** S-wave velocity.

V_{Pn} **:** P-wave NMO velocity.

W **:** Weight gate used for the local Tau-p Transform.

x **:** Coordinate direction x on the horizontal surface. Identified also with number 1.

y **:** Coordinate direction y on the horizontal surface. Identified also with number 2.

z **:** Coordinate direction z downward. Identified also with number 3.

Chapter 1

Introduction

1.1 Seismic waves and natural resource exploration

Seismic waves are energy disturbances that propagate through a material medium without altering it permanently. Since seismic wave theory relates the medium properties to wave propagation, information about these properties can be derived from observed seismic events. It is analogous to the human sight, whereby light (electromagnetic waves) provides images (information) about the world. As an example, the interior structure of the earth, in layered spherical shells, was discovered by analyzing the strong energy of natural seismic waves generated by *earthquakes* (see e.g. Shearer, 1999, Ch. 1).

The *seismic method of exploration* is a sophisticated technology developed to obtain information about the earth's crust from seismic waves. With this technology, artificial seismic waves generated by controlled sources and detected by sensors located according to a plan, are processed to obtain a meaningful image. The resulting data, interpreted in terms of geological information, can reveal possible locations of natural resources. This technology has been widely applied to hydrocarbon exploration.

Two basic seismic *wave modes* propagate through a solid medium: P or *compressional* and S or *shear*, each one affected in a different way by the medium's properties. The seismic method of exploration has traditionally relied only on P-waves, detected by one component sensors, but the S-wave information content has been neglected.

Sensors with three components, developed later, can detect S-waves in addition to P-waves. These sensors, also referred as *multicomponent* or 3-C, have allowed the development of the *multicomponent method* (e.g. Stewart et al., 2003; Garotta, 1999), to meet the increasing demand for information by the industry. However, application of this technology has been relatively limited. This thesis explores the multicomponent method applied to the land surface, aiming to extend and improve its application. It is focused on the more promising event, the PS-waves, which are waves generated as P and reflected as S. Near surface effects and deep geology imaging in complex areas are addressed. Analysis of theoretical models and experimental data have allowed the development of processing methods and to proposing potentially rewarding techniques.

1.2 Acoustic waves and elastic waves

Seismic waves have been the subject of extensive research, resulting in remarkably robust theoretical models. Some concepts relevant to the subject of this work are outlined in this section. Appendix A includes additional details.

1.2.1 Elastic wave propagation principles

The mathematical model of wave propagation applied to this work assumes an isotropic elastic medium. *Isotropic* means properties do not change with direction, and *elastic* means the medium recovers its exact original shape after deformation, without energy loss. Even though this is a simplification, it has proven successful in practical seismic exploration applications. The 2-D wave equations, which can be considered to be a backbone of this work, is introduced next.

Two coupled wave modes are obtained from the elastic wave propagation laws (see Appendix A), compressional or P wave, and shear or S wave. Using Cartesian coordinates in 2-D, the decoupled P wave is described by

$$(\lambda + 2\mu)\nabla^2\theta = \rho\frac{\partial^2\theta}{\partial t^2} \quad , \tag{1.1}$$

where t is time, ρ is density, and λ and μ are the *Lame* isotropic elastic constants or constitutive properties of the medium (Krebes, 1989); ∇^2 is the Laplacian operator, defined as

$$\nabla^2 = \frac{\partial^2}{\partial x^2} + \frac{\partial^2}{\partial z^2} \quad , \tag{1.2}$$

and θ is the *divergence*, defined as

$$\theta = \left(\frac{\partial u_x}{\partial x} + \frac{\partial u_z}{\partial z} \right) \quad , \tag{1.3}$$

which describes the compression or volume change, where u_i is the displacement component in direction i.

The P wave velocity (Appendix A, Section A.1.1) is expressed by

$$V_P = \sqrt{\frac{\lambda + 2\mu}{\rho}} \quad . \tag{1.4}$$

The decoupled S wave equation is

$$\mu \nabla^2 \omega = \rho \frac{\partial^2 \omega}{\partial t^2} \quad , \tag{1.5}$$

where ω is the 2-D *rotational* whose strain components are

$$\omega = \left(\frac{\partial u_x}{\partial z} - \frac{\partial u_z}{\partial x} \right) \quad . \tag{1.6}$$

The S wave velocity is

$$V_S = \sqrt{\frac{\mu}{\rho}} \quad . \tag{1.7}$$

Remarkable properties pertaining to these two wave modes are:

1. The velocity of a P wave is faster than the velocity of an S wave by a factor of about two in a consolidated medium.

2. The displacement caused by P waves is in the direction of propagation, while the displacement caused by S waves is normal to the direction of propagation.

3. S waves do not propagate in fluids since their rigidity μ is zero (fluids do not appreciably support tangential deformation).

1.2.2 Reflections and amplitudes in elastic waves

Seismic wave propagation depends on the medium's properties. If there is a sharp change of elastic properties in the medium, part of the wave energy returns backward as a *reflection*, and part of the energy continues forward (is *transmitted*) with a change of direction, as a *refraction*. The surface defined by such a change in properties is known as an *interface*. Reflected energy is the raw material of the seismic method of exploration.

Wave propagation can be represented by *rays*, which describe the progress in time and space of a point in a wave front. Ray theory is derived from a *high frequency* approximation to the wave equation (see e.g. Shearer, 1999), and *ray tracing* is the resulting modeling technique. [1]

A useful relation obtained from ray tracing is the *Snell's Law*, which reads

$$\frac{V_1}{\sin\theta_1} = \frac{V_2}{\sin\theta_2}\,, \tag{1.8}$$

where V_1 is the velocity of the incident ray, θ_1 is the angle of incidence to the interface normal, V_2 is the velocity of the reflected or refracted ray, and θ_2 is the angle of reflection (or refraction) to the normal (Fig. 1.1).

If a P-wave traveling in an elastic medium ($\mu \neq 0$) hits an interface at a non-normal angle, reflected and refracted P and S waves are generated, as illustrated by Figure 1.1. This is a relevant process in the seismic exploration method, and the cause of the wave conversion from P to S, addressed by this thesis.

The displacement *amplitude* of a reflection depends on changes in elastic properties, therefore contains geological information about the interface. Amplitude and its relation to the rocks' lithology is the basis of the AVO (*amplitude versus offset*) method (e.g. Ostrander, 1984), which has been applied extensively. The relations between amplitudes and interface

[1] Following Shearer (1999, p. 36), "Seismic ray theory is analogous to optics ray theory and has been applied for over 100 years to interpret seismic data. It continues to be used extensively today, due to its simplicity and applicability to a wide range of problems (...) Ray theory is intuitively easy to understand, simple to program and very efficient".

properties as a function of the angle of incidence and the elastic properties of the two media are established by the *Zoeppritz equations* (see e.g. Aki and Richards, 1980; Sheriff and Geldart, 1995; Krebes, 1989) [2].

The *reflection coefficient* is a parameter that characterize an interface, defined as the amplitude ratio between the reflected and the incident wave for a *normal* (zero degrees) angle of incidence. For a P-wave the reflection coefficient R, in terms of displacements, is defined as

$$R = \frac{U_R}{U_I} = \frac{\rho_1 V_1 - \rho_2 V_2}{\rho_1 V_1 + \rho_2 V_2} \tag{1.9}$$

Reflectivity is the property of a zone of interest described by the reflection coefficients as function of space or time.

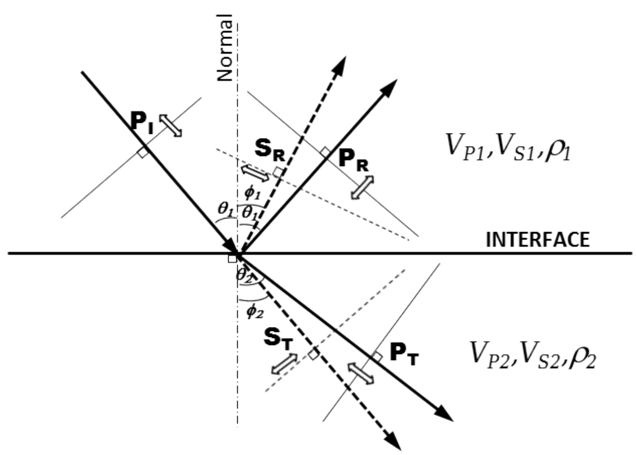

Figure 1.1: Wavefronts and rays for a P-wave incident (P_I) at an *interface*, which is the boundary between two media or *layers*, with different elastic properties V_P, V_S and ρ (layer 1 above and layer 2 below). Plane wavefront are represented by lines (continuous for P-wave and dashed for S-wave), and by the arrows normal to the wavefronts or *rays*. Under non-normal incidence to the interface, S-waves are generated and P and S-waves are reflected through layer 1 (P_R and S_R) and transmitted through layer 2 (P_T and S_T).

Factors that affect the reflection amplitudes, following O'Doherty and Anstey (1971), are:

[2] An example of their derivation for a particular case is in Appendix C

- Geometrical spreading, that is the amplitude decrease as the same energy is distributed over a larger area due to the radial expansion of the wavefront from the origin.

- Interface reflection coefficients.

- Inelastic attenuation or absorption, which reduces energy and the frequency range. It is considered in viscoelasticity.

- Transmission and scattering losses.

- Multiple reflection events.

Seismic processing methods addressed to improve the reflectivity information, such as true amplitude recovery and deconvolution, are discussed below.

1.3 Land seismic exploration

In land seismic exploration, seismic waves are generated by artificial sources of energy located at (or near) the surface. These waves can be reflected from geological interfaces, and then eventually recorded back at the surface by sensors deployed for the purpose. From these records an image of the geology can be generated. This method can survey extended regions with remarkable accuracy at relatively low cost, and analogously can be applied over land and marine settings. However land data presents additional challenges, such as the topography and the weathering of the near surface region.

Three stages can be identified in the seismic exploration method: *acquisition*, the recording of the data in the field; *processing*, which transforms the raw field data into a meaningful image; and *interpretation*, to derive a geologic model from the seismic image. The first two, which are part of the geophysical realm, are discussed below.

1.3.1 Data acquisition

Land *data acquisition* is illustrated in Figure 1.2. At the surface, in location s, an energy source generates a seismic wave, which is reflected at the interface and is then recorded at the sensor in g, located at a distance h from the source, known as the *offset.* As a result, the time variation of the seismic perturbation, known as a *trace*, is recorded as illustrated in Figure 1.2b.

Energy sources (*shots*) typically used on land-surface are explosives and vibratory machines. In practice, sensors (*receivers* or *geophones*) are deployed regularly on the surface, either in straight *lines* or in *areal* spreads. Sensors in straight lines generate 2-D profiles, while areal spreads generate 3-D data volumes (which lie beyond the scope of this thesis).

As illustrated in Fig. 1.2, there is usually a near-surface layer (NSL) with a low wave velocity, which results in a low angle of incidence to the surface, close to the normal, following Snell's Law (Eq. 1.8).

Traditionally, one-component sensors (1-C) that detect only vertical signals have been used. P-waves are recorded this way, since their displacement is closely normal to the surface (see Figure 1.2a). On the other hand, three-component (3-C) sensors detect signals in three orthogonal directions, one vertical and two horizontal. Hence, in addition to P waves, they can record the horizontal displacement of S-wave reflections.

Thus, as a shot generates seismic waves, a number of receivers are activated and each one of them records a *trace* (Figure 1.2b). The set of traces recorded by many receivers resulting from a single shot is a *shot record.* In 2-D acquisition one of the horizontal sensors usually is in the source-receiver direction, and is called *radial* and the other one, orthogonal to it, is called *transversal.* Figure 1.3 illustrates a synthetic shot record corresponding to a 2D-3C survey, with the vertical (Fig. 1.3a) and radial (Fig. 1.3b) components. The horizontal axis corresponds to the surface location of the receiver, and the vertical one to time, therefore there is a trace at each receiver location. These data were generated with a *finite difference*

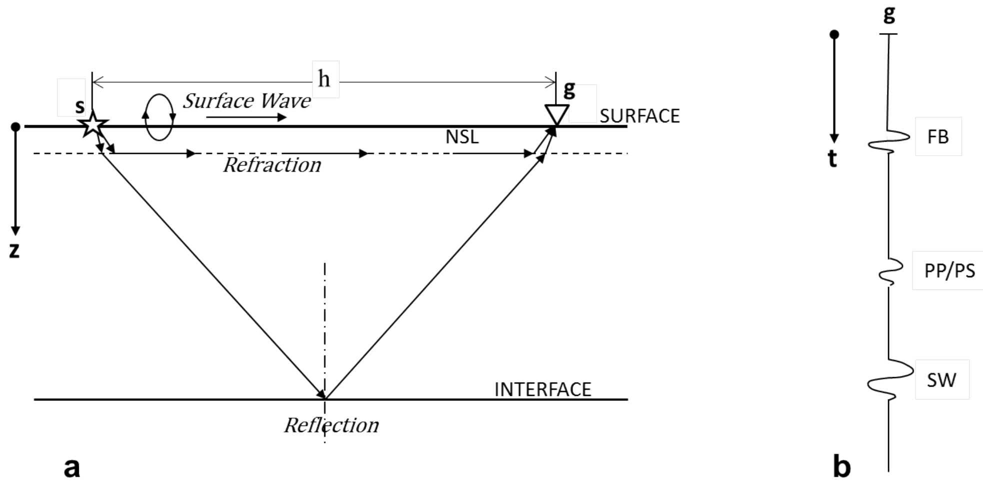

Figure 1.2: Elements of a *shot* in seismic exploration on land. (a) Shot profile, with the medium represented by a low velocity near surface layer (NSL) and a reflecting interface, dividing two layers with different elastic properties. The source (star, **s**) and the receiver (triangle, **g**) are on the surface, separated by the *offset* distance h. Three seismic events are illustrated with their raypath: a surface wave, a refractions in the NSL, and a reflection from the interface. (b) The *seismic trace* as recorded in time by the receiver, with the same events: a refraction, (signified by FB for First Break), reflections (PP/PS) and the surface wave (SW). Typically SW and FB are stronger, and SW is delayed by its low velocity.

isotropic elastic 2D algorithm (see details in Appendix D).

The shot record is the raw material for processing. A number of seismic events can be identified in Figure 1.3 (see e.g. Shearer, 1999). The first arrivals (FB, for *first breaks*), are mostly near surface refractions, whose arrival time increases linearly with the distance to the source (located at about $x = 2500$ in the Figure); a cone in the middle (GR for *ground roll*), corresponds mostly to surface (or *Rayleigh*) waves; the curved events in the middle correspond to reflections, mostly P-waves (labeled as PP) on the vertical component, and S-wave on the horizontal (labeled as PS and SS). These reflections are the source of information in the seismic method.

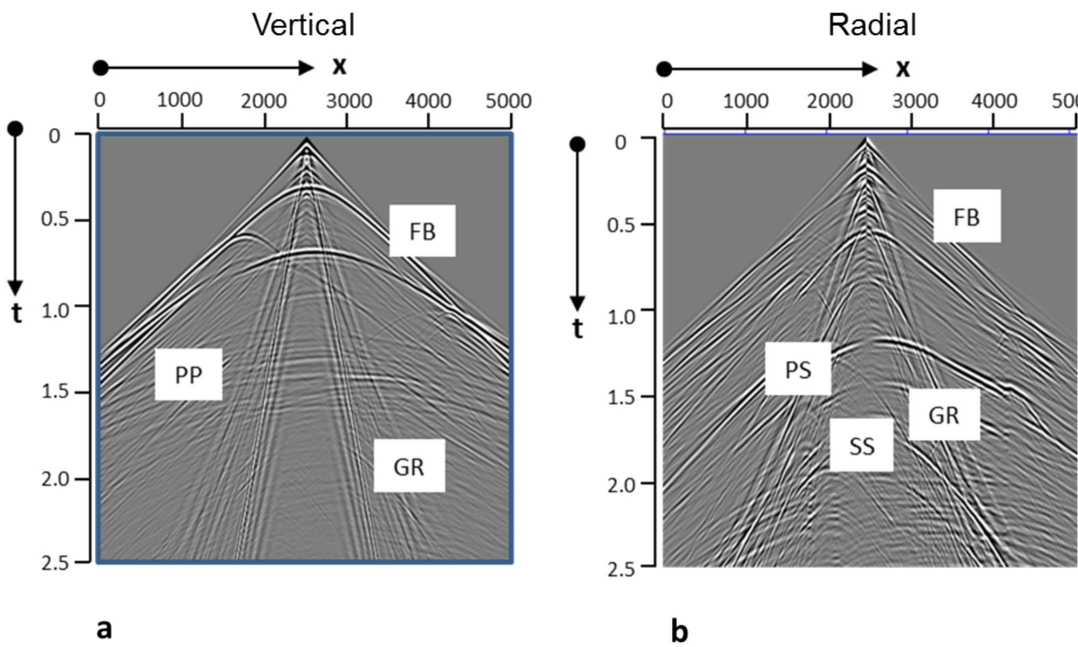

Figure 1.3: Shot records of the vertical and the radial horizontal components illustrating seismic acquisition experiment. (a) The vertical component shows most of the reflected P-wave energy (PP), and other events such as Ground-roll (GR) and refractions (FB). (b) The horizontal component right shows most of the S-wave energy, that can include PS and SS reflections. Note the curvature of the reflections.

1.3.2 Data processing

The expected outcome of seismic data processing is a reliable image of the geology and, perhaps, information about the lithology. Therefore, the goal is to obtain the seismic reflections at the right location, with the most detail (*resolution*) possible, and, hopefully, recovering the true reflection coefficients.

From a signal processing approach (see e.g. Robinson and Treitel, 2000), the data is composed of signal and noise, where signal contains the desired information and noise interferes with it. Seismic reflections are identified as the signal, any other events are considered to be noise. Thus, in Figures 1.2 PP and PS events are signal, while ground-roll (surface waves) and refractions are *coherent noise*. Additionally there are other sources of *incoherent* noise, such as the environment, human activity, and even anomalous signals of the electronic devices. Noise can be much stronger than signal. In fact, in a shot coherent noise events can contain more that 70% of the energy; in turn, reflections are relatively weak: using Equation 1.9, for a reasonable velocity change of 15%, the reflected strength is about 7% of the incident.

A technique to enhance the signal and attenuate the noise, that takes advantage of the redundancy of reflection information is illustrated in Fig. 1.4. According to Snell's Law, if the reflector is horizontal, PP waves are reflected at the midpoint between source and receiver (Fig. 1.4(a)). Traces of many shots with the same midpoint (Fig. 1.4(b)) can be gathered, forming a new data set called *common midpoint* (CMP) gather. Therefore the seismic events reflected at the same point are added together or *stacked*, increasing the power of the reflection by constructive interference and attenuating the noise by destructive interference. This technique is called *common midpoint stacking* (see e.g. Margrave, 2007).

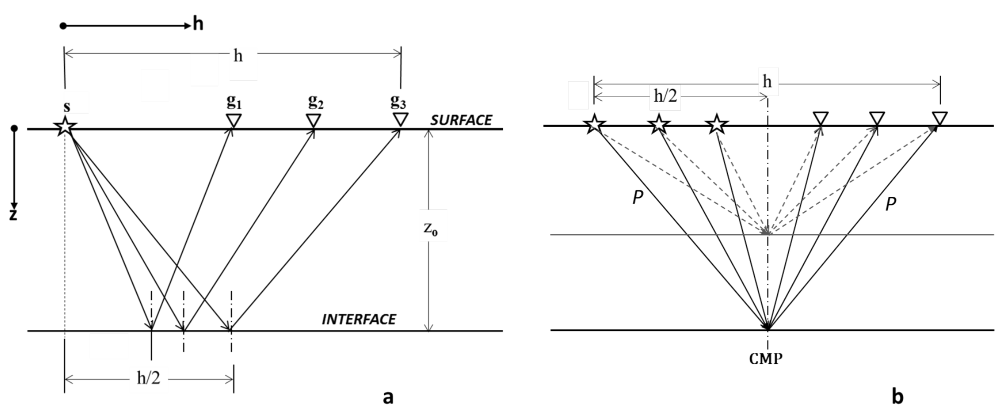

Figure 1.4: Shot gather with a flat reflector, CMP gather: flat reflector with constant velocity. (a) The *common shot gather* (CSG), composed by PP reflections generated by a shot. (b) The *common midpoint gather* (CMP), composed by PP events reflected at the same depth midpoint (half-offset distance) location, on a flat interface.

However, each source-receiver pair in a CMP gather has a different travelpath (Fig. 1.4b), therefore a different arrival time, which depends on the offset h. This delay is called *normal moveout* (*NMO*), and is the cause of the curvature of reflections noticed in Figure 1.3. Thus, to stack the reflections, compensation for this time delay is required, in a procedure called *NMO correction* (see e.g. Sheriff and Geldart, 1995; Yilmaz, 2001). The equation of the time delay as a function of the offset h is

$$t(h) = \sqrt{t_0^2 + \frac{h^2}{V_{NMO}^2}} \quad , \tag{1.10}$$

where t_0 is the arrival time for offset zero, and V_{NMO} is a sort of average of the velocities of the upward layers. Considered as a function of h this is a hyperbola (see Section A.4). An estimation of V_{NMO} is the *root mean squares* velocity or V_{RMS}, which for PP waves and the n layer is

$$V_{RMSn}^2 = \frac{\sum_{i=1}^{n} V_{Pi}^2 t_i}{\sum_{i=1}^{n} t_i} \quad , \tag{1.11}$$

where t_i is the zero offset (two-way) time spent through layer i.

However, in principle, the velocity V_{NMO} is unknown. Fortunately, the stacking method and Equation 1.10 can be used to get information about the velocity. Taking into account that the NMO correction, and therefore the corrected stack, depends on V_{NMO}, after testing stacks with a number of trial velocities, the appropriate V_{NMO} should correspond to the highest energy stack. This is the basic principle of a key step in seismic data processing known as the *velocity analysis*, an additional product of the stacking technique (see e.g. Sheriff and Geldart, 1995; Yilmaz, 2001).

As shown above, *reflectivity* contains geologic information about specific interfaces (Eq. 1.9). In practice, the seismic trace results from the interaction between reflectivity and a short duration energy packet generated by the source (see Fig. 1.2b), known as *wavelet* or *source signature*. Signal processing technology provides a mathematical model for this interaction, the operation of *convolution* (e.g. Robinson and Treitel, 2000), such that each trace can be considered the result of convolution between a wavelet and the reflectivity over time. This model allows the application of *deconvolution*, the inverse operation, to obtain the reflectivity. In practice, deconvolution increases the resolution of seismic data (see Yilmaz, 2001), and can compensate for amplitude and frequency variations related to anelastic attenuation (see e.g. Margrave et al., 2011), among other benefits.

The previous methods are based on a relatively simple model of wave propagation, and strictly speaking, are valid only for a flat geology. However, geology is frequently far from flatly layered, and wave propagation can be much more complicated. *Migration* is the name of a technique developed to consider these complications (Bancroft, 2007; Yilmaz, 2001).

Migration is defined by Gazdag and Sguazzero (1984a) as "the process of constructing the reflector surface from the recorded seismic data". It can handle phenomena like diffractions, dipping interfaces, and complex geological structures, using algorithms that better honor the wave equation. That such a methods were needed was identified early in seismic exploration. Firstly empirical methods were developed, and later were systematized, with robust theoretical support, in the 1970s (see e.g. Schneider, 1971; Gray et al., 2001). A number of migration technologies were developed, focused on PP-wave exploration, and greatly supported by progress in computer technology. Initially they were applied to stacked data (*poststack migration*). Now, greater computer power has allowed migration to be commonly applied before stacking (*prestack migration*). Prestack migration provides advantages such as imaging of dipping layers and better amplitude analysis (Gray et al., 2001).

The migration process has two steps: *wave extrapolation*, to rebuild the seismic event propagation, and *imaging condition*, to identify a reflection. Wave extrapolation is carried out by algorithms derived from wave equations. A velocity model of the medium is required. The imaging condition was defined by Claerbout (1971) as: "reflectors exist at points in the ground where the first arrival of the downgoing wave is time coincident with an upgoing wave".

In practice, two main types of migration techniques occur, *time migration* and *depth migration*. Time migration is a robust method from simplified assumptions, that yields an image of the reflector from an approximated velocity model. Depth migration requires a more accurate velocity model, however it enables more reliable images, especially if velocity varies laterally, such as occurs in complex areas (see e. g. Gray et al., 2001; Biondi, 2006).

Summarizing, following Yilmaz (2001), seismic data processing involves three major techniques: *deconvolution*, *stacking* and *migration*. However, important additional processes are also required, such that compensating for anomalous near-surface time delays, (known as *statics correction*, see more details in chapters 2 and 3), noise filtering, and amplitude correcting (Yilmaz, 2001; Sheriff and Geldart, 1995).

Figure 1.5(a) illustrates a simplified process flow for PP-waves, identified as *conventional processing*, which does not include more advanced methods such as prestack migration and inversion. More details can be found, for example, in Yilmaz (2001) or Sheriff and Geldart (1995), Ch. 9.

1.4 Exploration with S-waves: SS and PS

1.4.1 S-waves and multicomponent data

The feasibility of recording S-wave is probably the most important benefit of multicomponent sensors. S-waves were identified as a potential source of information from at least the mid 1950's onward (e.g. Koefoed, 1955). However the industry ignored S-waves for many years[3]. In fact, somewhat disappointing drawbacks on S waves were identified from early studies. Among them, high sensitivity to anisotropy (Jolly, 1956), and strong attenuation (White and Sengbush, 1963)[4]. Furthermore, the near-surface layer affects S waves more strongly than P-waves (Wiest and Edelmann, 1984; Anno, 1986), since S-waves are slower and more susceptible to the solid matrix properties (see section 2.1), making their statics correction much harder to obtain (see section 3.1 and 3.2). In addition, at or near to the surface, strong seismic events are generated, and strong anisotropy and attenuation are common, which interferes greatly with S-waves.

[3]Claerbout (1985), p.42, says "It is remarkable that more than 99% of industrial petroleum prospecting ignores the existence of shear waves".

[4]Polškov et al. (1980) do not agree that S-waves have generally strong attenuation, considering that this is only valid for the near-surface layers.

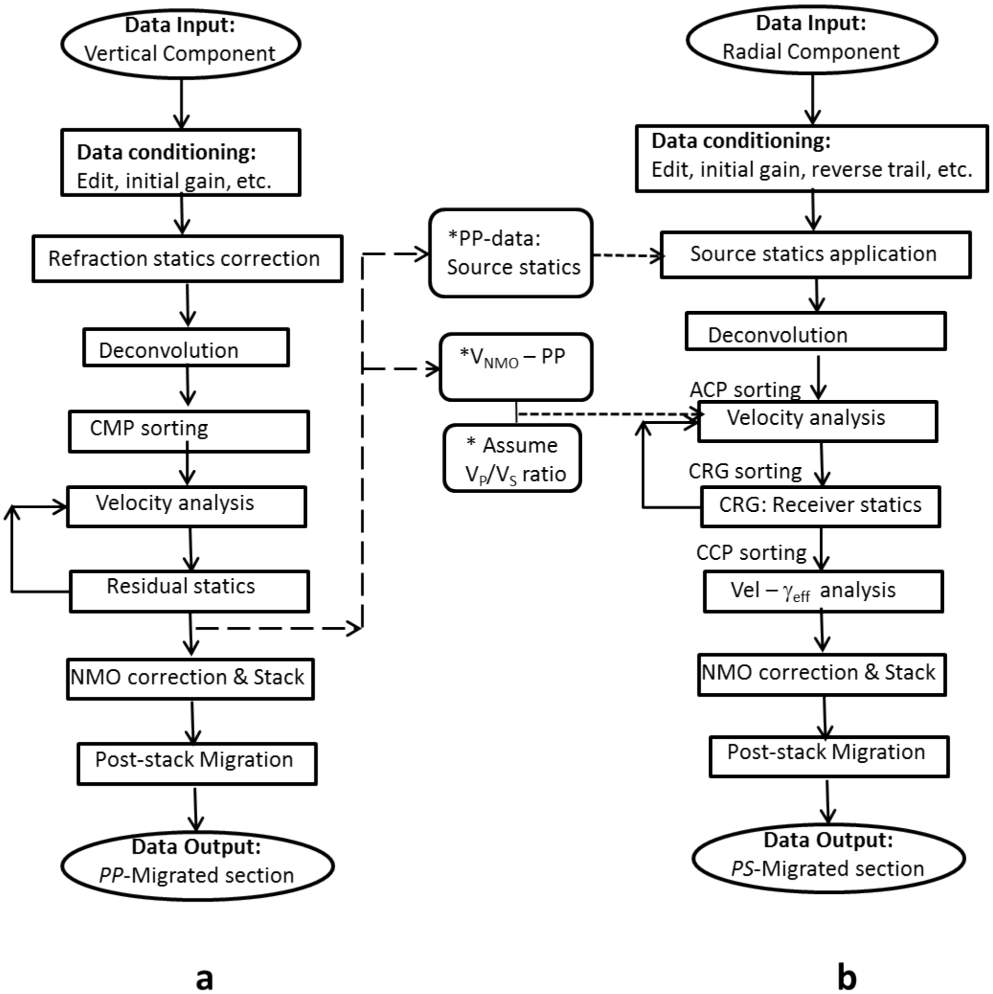

Figure 1.5: Simplified conventional seismic processing flow. (a) PP processing, (b) PS processing. Notice that PS processing requires results from PP processing.

Nonetheless, research developments in the 80s and 90s (e.g. Polškov et al., 1980) have enabled practical applications of S-waves as shown, for example, by Garotta (1999), Stewart et al. (2003) and Barkved et al. (2004). Two S-wave reflection types have been the subject of interest in exploration: *pure* S-waves, called SS, generated and reflected as such, and *converted* S-waves, called PS-waves, generated as P-waves and converted to S at the reflector (see Fig. 1.1).

SS waves seem more convenient in principle, since they are analogous to PP-waves[5].

[5]Much research efforts were directed at the SS-wave known as SH, polarized normal to its plane of

However, SS-wave acquisition appears involved (Garotta, 1999), requiring specific energy sources, and the near-surface effect is quite strong, since it affects SS-waves at both source and receiver sides. These issues led to an increased interest in PS-waves, which do not require special energy sources and are least affected by the near-surface (S-waves only at the receiver side). Besides that, their energy content is high, comparable to PP-waves in many cases (Garotta, 1999). This work focuses on PS-waves as well, taking into account these practical advantages. Converted PS-wave has been identified with acronyms like $P-SV$, or C wave (Garotta, 1999; Thomsen, 1999). PS is used in this work, although the letter C appears occasionally in certain situations of practical convenience.

1.4.2 PS-wave processing overview

Figure 1.6a illustrates a key difference between PP and PS reflections, comparing rays reflected at a flat interface. A P-wave source of energy located at s generates waves detected by a sensor at g. The distance between source and receiver or *offset* is h. According to Snell's Law (Equation 1.8) the incidence and reflection angles to the interface are the same for PP-waves, while the PS-wave reflection angle ϕ is smaller than the incidence angle θ, due to the lower S-wave velocity. Therefore, instead of the CMP of PP-waves, we have a *common conversion point* (*CCP*) for PS-waves, which depends on the velocity. In principle, the success of the stacking method depends on correctly identifying the CCP (see e.g. Stewart et al., 2002).

Below is a summary of PS-wave processing, identifying three major stages: the basic or *conventional* processing, the incorporation of the anisotropic approach, and some recent developments including migration and inversion.

A conventional processing flow for a PS-wave is illustrated in Figure 1.5b. It is customarily assumed in conventional processing that the vertical component corresponds to PP-wave

---

propagation, which appears simpler since in principle does not have mode conversions (Jolly, 1956; Garotta, 1999).

and the horizontal radial component to PS-wave, taking into account that they arrive close to normal to the surface, as shown in section 1.3.1 (see Figure 1.2a).

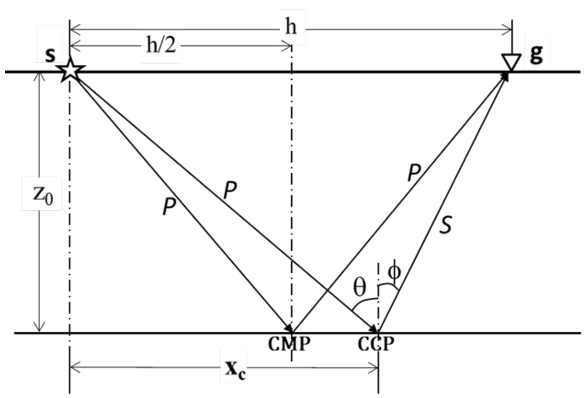

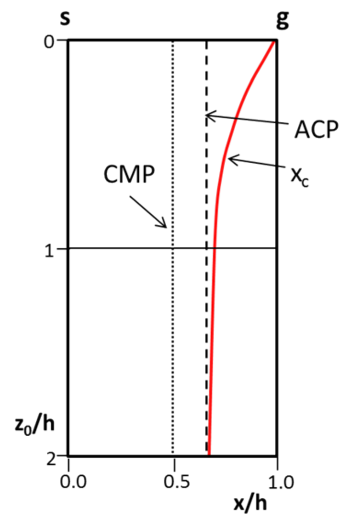

Figure 1.6: PS-wave reflection analysis and the *common conversion point*. (a) PP and PS-waves reflected from a flat horizontal interface, represented by rays generated at a single source and detected at a single receiver. PP is reflected at the midpoint between source and receiver (CMP), and PS is reflected at a *Common Conversion Point* (CCP), which depends on V_P and V_S velocities (After Tessmer and Behle (1988)). (b) The variation of the CCP location with depth, x_c, and the *asymptotic conversion point* approximation, ACP. (after Thomsen (1999))

Basic or *conventional* processing of PS-wave can be traced back to Tessmer and Behle (1988), who identified three steps in common reflection point stacking: common reflection point sorting of the data, definition of traveltimes, and definition of stacking (or RMS) velocities. They developed an expression for the conversion point x_c on a constant velocity flat reflecting interface, using a quartic equation[6]. It is a function of γ, defined as the ratio

[6]The equation is

$$\left(x_c - \frac{h}{2}\right)^4 + \left(z_0 - \frac{h^2}{2}\right)\left(x_c - \frac{h}{2}\right)^2 - z_0^2 h\left(\frac{\gamma^2+1}{\gamma^2-1}\right)\left(x_c - \frac{h}{2}\right) + \frac{h}{16}\left(h^2 + 4z_0^2\right) = 0, \tag{1.12}$$

where the variables are defined in Figure 1.6(a), and γ is the ratio of average V_P and V_S velocities defined in the main text, Equation 1.13.

of average V_P and V_S velocities,

$$\gamma = \frac{\overline{V_P}}{\overline{V_S}} = \frac{\sum_i z_i / V_{Si}}{\sum_i z_i / V_{Pi}} \quad . \tag{1.13}$$

An example of the resulting x_c is illustrated in Figure 1.6b for the case of $\gamma = 2$ (Thomsen, 1999). The *asymptotic conversion point* or ACP is an approximation, indicated by the dashed line in Figure 1.6(b), and defined as

$$x_{c0} = h \frac{\gamma}{1+\gamma} \quad . \tag{1.14}$$

Notice that the ACP is an accurate approximation to x_c for values of z_0/h greater than 1, but not for low values ($z_0/h < 1$). Thus, x_c allows improved sorting of the traces compared to the ACP. Tessmer and Behle (1988) claim that x_c is a reasonable approximation even in the case of many layers.

Tessmer and Behle (1988) also presented an NMO equation for many layers based on a Taylor series approximation:

$$t_{c_n}(h)^2 = t_{0c_n}^2 + \frac{1}{V_{c_n}^2} h^2 + O(h^4) \quad , \tag{1.15}$$

where t_{0c_n} is the zero offset arrival time of the PS wave and V_{c_n} is an RMS approximation to the PS wave velocity in the layer n, then

$$t_{0c_n} = \sum_{i=1}^{n} (t_{Pi} + t_{Si}) \qquad \text{and} \qquad V_{c_n}^2 = \frac{\sum_{i=1}^{n} V_{Pi} V_{Si} (t_{Pi} + t_{Si})}{\sum_{i=1}^{n} (t_{Pi} + t_{Si})} \quad ; \tag{1.16}$$

for short offsets Equation 1.15 can be simplified to the first two terms, resulting in a hyperbolic approximation, analogous to Equation 1.10 for PP waves.

Harrison (1992) states a complete time poststack processing flow until post-stack time migration, which closely agrees with the *conventional* basic processing flow for converted wave, summarized in Figure 1.5b. This processing flow is the basis for any subsequent step, since it generates the parameters required later on. Harrison (1992) also included PS DMO and presented methods of birefringence analysis for fracture detection, spread amplitude compensation and velocity inversion.

Building on these previous achievements, Thomsen (1999) developed an approach with polar anisotropy[7] concepts, addressing many layers and anisotropy. As established above, the basic parameters for gathering PS-waves depend on the NMO velocity. Thomsen (1999) noted that horizontal layering generates a velocity field that corresponds to the polar or VTI anisotropy model, which can be handled with the weak anisotropy framework (Thomsen, 1986) (see section A.3 in Appendix A). Hence, two V_P/V_S ratios are proposed, γ_0 derived from zero offset arrival times,

$$\gamma_0 = V_{P_0}/V_{S_0} = t_{S_0}/t_{P_0} \quad ,$$

and γ_n derived from the NMO correction

$$\gamma_n = V_{P_n}/V_{S_n} \quad ,$$

where the index 0 corresponds to zero offset, and the index n corresponds to the NMO correction. Thus, a derived parameter, called the *effective gamma* or γ_{eff},

$$\gamma_{eff} = \frac{\gamma_n^2}{\gamma_0} \tag{1.17}$$

takes into account these properties for processing. Approximate equations for conversion point and arrival time as a function of offset result from Taylor's series solutions. Thus, the conversion point is given by

$$x_c(h,z) \approx h\left[c_0 + c_2\frac{(h/z)^2}{1+c_3(h/z)^2}\right] \quad , \tag{1.18}$$

where

$c_0 = \dfrac{\gamma_{eff}}{1+\gamma_{eff}}$ is the ACP coefficient (see Eqn. 1.14) and c_2, c_3 are functions of γ_{eff} and γ_0 ; since z is unknown, it is approximated by

$$z = V_{cn}t_{c0} \quad .$$

[7]Polar anisotropy is also known as VTI for Vertical Transverse Isotropy.

The NMO arrival time is given by

$$t_{c_n}(h)^2 = t_{0c_n} + \frac{1}{V_{c_n}^2}h^2 + \frac{A_4 h^4}{1 + A_5 h^2} \quad , \quad \text{where} \quad A_4 = \frac{-(\gamma-1)^2}{4(\gamma+1)t_{c0}^2 V_{c_n}^4} \quad \text{and} \quad A_5 = \frac{-A_4 V_{cn}^2}{\left(1 - \frac{V_{S_n}^2}{V_{P_n}^2}\right)} \quad .$$

More recent advances in converted wave processing focus on pre-stack migration in time, including PS-wave anisotropy with additional parameters that take into account larger offsets (e.g. Li et al., 2007). Further developments include prestack time anisotropic migration and velocity analysis (Cary and Zhang, 2011) and elastic wave equation depth migration in a fractured medium (Bale, 2006). In many cases, obtaining the appropriate parameters is still challenging. These methods are additional to the generalized basic processing flow for converted waves of Figure 1.5b.

Some authors (e.g. Kuo and Dai, 1984; Hokstad, 2000) have proposed elastic migration methods, using the Kirchhoff approach (see section 5.2.1), which in principle can handle the complete vector wavefield. This approach appears promising, however a review of the literature reveals a lack of applications. Etgen (1988) proposed elastic wave migration in the frequency domain, using the Stolt and PSPI methods. More recently, works using the elastic *reverse time migration* (RTM) approach (two-way wave propagation) have been published (e.g. Yan and Sava, 2008; Wang and McMechan, 2015). Also Stanton (2017) proposed a least squares elastic migration, using a one way wave propagation model .

In addition, multicomponent data have been subject to the promising Full Wave Inversion (FWI) approach (e.g. Prieux et al., 2013, on marine data), intended to obtain elastic parameters. Here too, however, applications to real data are not common.

1.5 S-wave exploration challenges and the road ahead

As shown in section 1.2.2, S-waves can provide additional information about the medium (the geology), beyond that supplied by P-waves. It is also shown that use of converted PS-waves appear more convenient in practice (Section 1.4.1). In fact, they have been applied successfully to specific problems, such as bad P-wave image settings caused by gas chimneys, anisotropy to identify fracture trains, or lithology discrimination, among others (see e.g. Garotta, 1999; Stewart et al., 2003; Barkved et al., 2004).

In practice, however, PS-waves are applied less often than PP-waves since they require more effort for 3-C acquisition, their processing is more involved and laborious, and their interpretation appears less profitable (see e.g. Cary, 2001). S-wave properties such as the high sensitivity to anisotropy and the anelastic attenuation can partially explain these shortcomings. In addition, the complex PS-wave travel-path prevents simple solutions based only on geometry. Finally, in land data, the NSL introduces additional hurdles, such as statics corrections and the strong coherent noise of surface waves.

As a consequence, S-waves have been applied more successfully to marine data, to zones with very good signal quality, or to relatively simple geological settings. Land settings with complex NSL, with rough topography, or with complex geology at depth, are more challenging, even though the potential of S-waves to improve the information from complex land environments has been recognized (e.g. Grech, 2002)[8]. This thesis is intended to contribute a step forward in that direction, processing of multicomponent data in land complex settings, focused on PS-waves.

1.6 Thesis overview

A number of questions arise when facing the challenges of multicomponent data in complex land environments. It is apparent that some of the simplified assumptions should be dismissed as much as possible. Among them are the flat free surface, the homogeneous low velocity NSL, and the flat horizontal reflectors. Hence, heterogeneous NSL, rough topography and complex geological structure appear as the leading issues to solve. However, as

[8]Multicomponent data could even provide improvement of PP-wave exploration in complex settings, taking into account their rough topography (e.g. Behr, 2005; Guevara et al., 2007) and their frequently irregular 3-D geometry, and taking advantage of the directional properties of multicomponent data (e.g. Stewart and Marchisio, 1991).

proved by previous efforts, even the simpler assumptions pose a huge challenge. Therefore, other elements need to be simplified, such as the wave propagation model or expectations about advanced results such as high resolution or true amplitude.

1.6.1 Scope

This thesis is focused on processing methods for elastic waves as related to the NSL, the rough topography, and the geological structure, including the following topics:

- Experimental analysis of a near surface S-wave velocity model, and its application to processing.
- Supporting the previous point, an experimental analysis of explosive sources of energy is discussed.
- A study of PS-wave statics correction methods, with the proposal of a new option.
- Overcoming the assumption of identifying P-waves with the vertical component and S-wave with the horizontal components, proposing a method of mode separation in cases of rough topography.
- Development of algorithms for pre-stack depth migration (preSDM) from topography for PP and PS-waves.

The work is focused on PS-waves, and the wave propagation model is isotropic elastic 2-D; anisotropy, anelasticity and 3-D issues are disregarded.

1.6.2 Methodology

The methodology can be summarized as follows:

- Review of the methods currently applied by the industry to the subjects of interest.

- Analysis of each issue, either from real data, synthetic data, and previous research.
- Identification and analysis of possible solutions, taking into account relevant work from the literature.
- Development and coding of algorithms.
- Generation of synthetic data and testing of algorithms with them.
- Application of the solution to real data wherever possible.
- Analysis of the results and derivation of possible extensions.

1.6.3 Contribution

This thesis makes the following contributions to elastic wave exploration, and to processing of PS-reflections on land:

1. A method for analysis of the near-surface Vs model based on borehole data, with possible application to land acquisition.
2. Identification of S-waves generated by common explosive sources in an uphole survey, relating these events to data generated on a surface seismic line. This relation suggests that SS-waves are more common than usually assumed.
3. An automatic method of static corrections for converted waves at the receiver that does not require a PS velocity model, which is promising for low quality data.
4. Development and analysis of a wave-mode separation method taking into account the sloping surface and the free surface receiver response.
5. Implementation and testing of algorithms for PreSDM from topography, and for PP and PS-waves, using PSPI and Kirchhoff migration methods.

1.7 Thesis Plan and Tools used

1.7.1 Thesis outline

The Thesis has the following chapters:

- Chapter 1: An overview of elastic waves and PS-waves within the seismic method of exploration, and a summary of relevant aspects of the thesis.
- Chapter 2: Analysis of an uphole survey experiment to obtain the near surface S-wave velocity model.
- Chapter 3: A new PS-wave receiver statics correction method.
- Chapter 4: A method for wave mode separation with topography, taking into account the free surface response.
- Chapter 5: Two algorithms of PreStack Depth Migration from topography for PP and PS-waves.
- Chapter 6: Conclusions and future work.

The Appendices contain mostly mathematical complementary explanations about the methods used.

1.7.2 Codes produced

The following codes were written, mostly in Matlab®.

- Dix equation for analyzing direct waves generated by explosive sources and the resulting velocity model (Chapter 2).
- Source radiation patterns calculation for a borehole filled with fluids, according to Lee and Balch (1982) (Chapter 2).

- Trace interpolation using the τ-p transform for a CRG (Chapter 3).
- Calculation of the receiver statics, by crosscorrelation of adjacent CRGs, stacking of crosscorrelations, and calculation of the differential receiver statics (Chapter 3).
- Wave mode separation algorithm by data conditioning, data rotation, gaussian gate application, free surface response calculation, and inversion using the τ-p transform in the frequency domain (Chapter 4).
- Prestack depth Kirchhoff migration from topography code for PP and PS waves, based on a prestack time migration code for PP waves in flat areas provided by CREWES (Chapter 5).
- Phase-shift plus interpolation depth migration code from topography for PP and PS waves, developed from CREWES prestack time migration code for PP waves in flat areas (Chapter 5).
- I also contributed to the development of EcoElas2D, the elastic FD 2D code of Ecopetrol.

1.7.3 Tools used

A number of software programs were used to carry out numerical analyses for this Thesis. Matlab®, and the CREWES Matlab toolkit, were instrumental to developing most of the experimental code. Among the CREWES utilities used for the experiments are the prestack migration codes for PSPI and Kirchhoff prestack migration, and the FD elastic modeling code. In addition, ProMAX®by Halliburton was instrumental for conventional data processing, and data format transfer. Seismic Unix (SU) utilities, from the CWP at the Colorado School of Mines, were used for format transfer and data graphics. $\tau - p$ transform forward and inverse codes, by the Signal Analysis and Imaging Group of the University of Alberta, were also quite useful. The modeling software EcoElas2D of Ecopetrol, an elastic isotropic FD 2-D modeling code including topography, was also used for the generation of synthetic data. Norsar 2-D and 3-D was used for ray tracing modeling.

Chapter 2

Shear-waves from an uphole experiment: V_S in the near surface and its relation with a conventional 2-D line

2.1 Introduction

As stated previously, the Near Surface Layer (*NSL*) on land affects more severely the seismic image obtained with S-waves than with P-waves. This is a critical matter in PS-wave processing (e.g. Garotta, 1999; Anno, 1986). The analysis of S-waves in the NSL is relevant, since it can contribute to the understanding of the shortcomings of the processing methods and can provide clues to improve them.

S-waves in the NSL are investigated in this chapter by using a field experiment, comprised of a shallow borehole with explosive sources of energy inside, and 3-C receivers on the nearby land surface. P and S-waves generated by the explosive sources were identified, which allowed the building of an elastic velocity model of the NSL. The model appears robust, supported by tests, and can be related to the lithology. Analyzing its relationship to land surface data shows shortcomings of the latter for generating a NSL V_S model. On the other hand, it supports the possibility of direct S wave generation in any land surface survey using explosive sources inside boreholes.

2.1.1 Near surface layer characteristics

The earth's surface is subject to environmental factors such as temperature, rainfall, and wind, which interact with features such as slope, parental rock, or water currents, generating processes of weathering, erosion, and deposition of sediments (Cox, 1998). As a consequence, typically an unconsolidated, heterogeneous layer with variable thickness, covers the consolidated rock. This NSL usually includes a water saturated zone, whose top is known as the *water table*. These are the features of the zone identified as the *weathering* or *near-surface layer* (NSL).

2.1.2 Effect of the NSL on P and S-waves

Since P and S waves depend on different properties of the medium, they are affected in a different way by the NSL, which is illustrated in Figure 2.1. Recalling section 1.2.1, P-waves depend on compressibility, which is present in solids and fluids, while S waves depend on rigidity, a property of solid media. In addition, P-waves are about two times faster than S-waves in consolidated rocks.

Therefore, the water saturated zone affect P-wave propagation, but not S-wave propagation. In turn, S-waves are affected by the heterogeneous unconsolidated terrain and, because of their lower velocity, the wavelength is shorter for comparable temporal frequency (Equation A.21), and hence S-waves are affected by smaller heterogeneities of the medium.

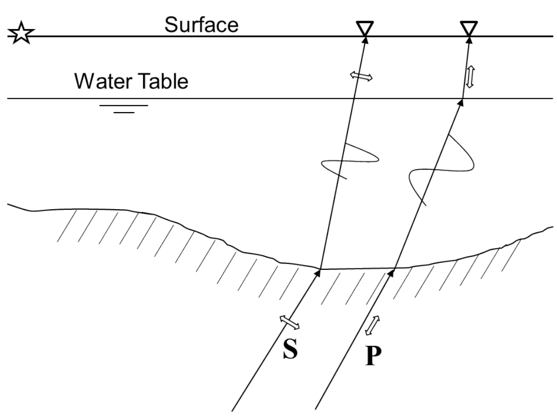

Figure 2.1: P and S waves in a typical near-surface layer: S wave propagate directly through the heterogeneous near surface medium, unaffected by the water table, while P wave is affected by the presence of the water, more homogeneous. Since S waves are slower, their wavelength is shorter, then are affected along a longer travel-path by smaller heterogeneities than P waves.

In fact, Wiest and Edelmann (1984) and Stümpel et al. (1984) confirm these properties of elastic waves in the NSL from real case histories. They found that the V_P/V_S ratio, can be 5 and higher in the NSL. Wiest and Edelmann (1984) also noted that V_S increases more gently with depth, while V_P usually shows a sharp increase at shallow depth, which is explained by the presence of the water table. The real data near-surface S-wave propagation analyzed in this chapter agrees with this model, as shown below.

Anisotropy and attenuation also have meaningful effects on S-waves in the NSL (see e.g. Jolly, 1956; White and Sengbush, 1963). Even though they are beyond the scope of this work, some comments about attenuation will be included below..

2.1.3 Problems for exploration generated in the shallow layer and their solution methods.

Time delays caused by the NSL affect seismic data generated and recorded at the surface. In particular they have a very important effect on the stacking process, part of conventional processing, referred to in Section 1.3.2. At this stage, traces of many sources and receivers, reflected at the same common midpoint (CMP), as illustrated in Fig. 1.4b, are stacked to increase the strength of the signal. But each trace has a different NSL delay due to its source and receiver locations; therefore the stack waveform is damaged. Hence, the time delays caused by the NSL should be removed to obtain the right image of the reflections at the CMP. Additionally, since S-waves are slower and not affected by fluids, the effect of the NSL on S-waves is more severe than on P-waves. This is a serious issue for PS-wave processing, currently the subject of academic and industrial research efforts (e.g. de Meersman and Roizman, 2009; Al-Dulaijan and Stewart, 2010).

Statics correction is the name of the method developed to make up for the time delay on seismic events affected by the NSL[1]. Statics correction was developed firstly for P reflection seismic imaging, providing effective and robust results. This technique is based in the property that, due to the low velocity of the NSL, waves arrive closely normal to the surface.

[1]The name *statics correction* originates in that it is a time shift of all the trace.

Thus, at each source or receiver location it is possible to define a unique value for the statics correction, namely it is *surface consistent*. More details and methods are in Chapter 3.

Statics correction is a good approximation if the NSL has low velocity compared to the underlying consolidated rock, if it is not very thick and if the topography is relatively flat, which has been proved in practice. However, it is less appropriate for thick or high velocity near surface layer, or for rough topography. In such cases methods more closely based on the wave propagation physics are more appropriate, such as *wave equation datuming* (see e.g. Berryhill, 1979) and migration from the surface (e.g. Al-Saleh et al., 2009; McMechan and Chen, 1990). Chapter 5, which addresses complex areas issues such as elevation variations, provides more details.

2.1.4 Methods to obtain S-wave velocity in the the NSL

The velocity model is a required input for some methods that correct the effect of the NSL in seismic data. Methods to obtain the near-surface V_S model can be classified as indirect and direct. The velocity in indirect methods is obtained by analyzing seismic events that propagate through the NSL, like Rayleigh waves (Socco et al., 2010; Askari, 2013) or refractions (Dufour et al., 1996). They can give velocities of large areas at a low cost. However their accuracy is not always satisfactory for S-waves (e. g. Schafer, 1993; Al-Dulaijan and Stewart, 2010).

In the direct methods sources and receivers are located in a borehole and on the land surface (Cox, 1998), and the velocity is obtained by measuring the time of a seismic event between them. These methods allow relating V_S to depth and to lithological properties for a specific location. There are two modes: *downhole surveys*, with sources on the surface and receivers inside the borehole, and *uphole surveys* (also known as reverse VSP), with sources in the borehole and receivers on the surface (Cox, 1998). Downhole surveys have had engineering applications (e.g. Kim et al., 2004), as well as for exploration purposes (Miong et al., 2007). Uphole surveys appear less commonly used; and difficulty to get appropriate

S-wave sources has been reported, as much as concerns on damaging the borehole (Parry, 1996).

2.2 The experiment: field Data

The experimental data analyzed in this chapter were collected in a land multicomponent survey, known as the Tenerife Project, acquired by Ecopetrol in the Middle Magdalena Valley of Colombia. Details about it are in Agudelo et al. (2013), Guevara et al. (2013) and Mason (2013). This survey included surface 3-D 3-C seismic data, shallow boreholes, well logs, and a 9 Km 2-D 3-C seismic line. Figure 2.2 illustrates the location and relevant characteristics of the setting and the 2D 3C seismic line (identified by a dotted line). Two shallow experimental boreholes approximately 3 km apart were recorded. One of them was acquired in a flat area on a Quaternary Formation, about 400 m away from a small river, on its flood plain. It is the subject of this study, identified as *Uph-1*, represented by a star in the map of Figure 2.2.

Figure 2.3 shows the *Uph-1* borehole layout. Two source types provided the seismic energy: small dynamite charges (150 g) and *blasting caps*, which were interspersed inside the borehole and separated 2.5 m from each other, as shown in the Figure. The maximum depth was 60 m. The receivers were 3C accelerometers deployed on the surface with a maximum offset of 200 m, and separated 5 m from each other. The following analyses do not use all the spread, only the receivers up to a maximum offset of 100 m.

Figure 2.4 shows the lithological profile at this location, obtained from the drilling cuttings. Most of the profile corresponds to clays interbedded with sands; a layer of conglomerates and other hard materials between 23 and 42 m depth was also identified.

Figure 2.5 shows five examples of the data records for source depths of 55, 45, 30, 20 and 10 m. Figure 2.5a corresponds to the vertical component and Figure 2.5b to the horizontal component, which are analyzed in the next section.

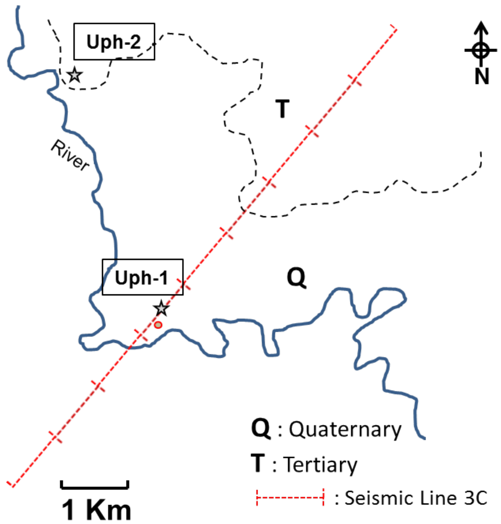

Figure 2.2: Multicomponent field experimental survey in Colombia: location map.

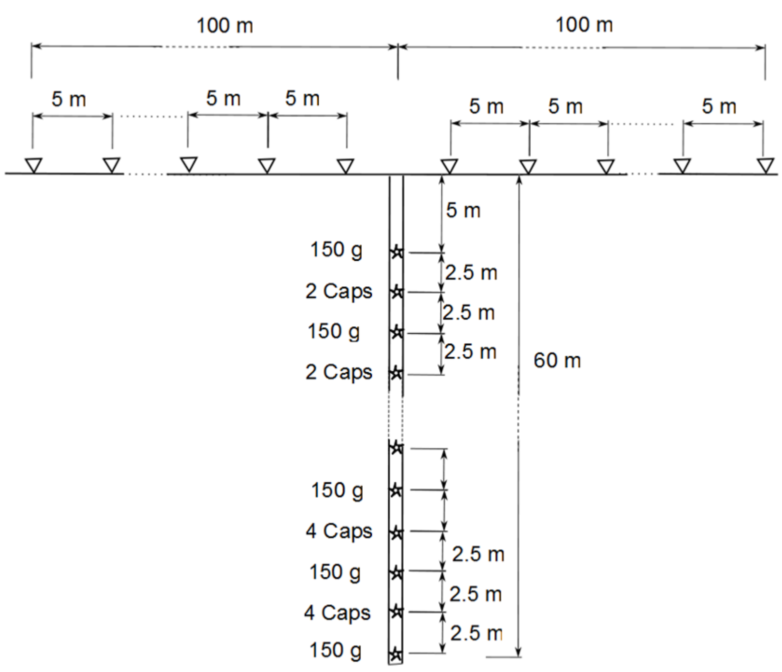

Figure 2.3: Profile of the borehole and sources deployment.

.

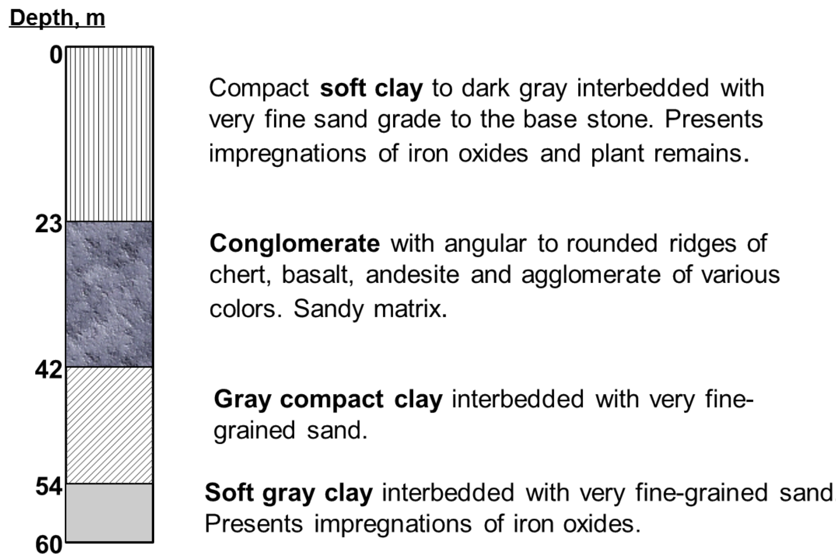

Figure 2.4: Stratigraphic profile of the borehole obtained from drilling cuttings.

2.3 The V_S model analysis

A velocity model based on the shot records is set up and analyzed in the following. Noticeable events are the strong first breaks (FB) on the vertical component and a later hyperbolic, high energy event on the horizontal component

2.3.1 Identification of P and S-waves generated by the source

Notice two strong hyperbolic events in Figures 2.5a and 2.5b: the first breaks, on the vertical component (Figure 2.5a) identified as FB in the following, and a delayed one, on the horizontal component (Figure 2.5b), identified as H1 meanwhile. Their strength indicates that they are unlikely to be reflections or refractions (e.g. Muskat and Meres, 1940), and are therefore more likely direct waves, and their hyperbolic shape correspond to events generated at the source, hence traveling upwards to the surface. The FB of Fig. 2.5a are the fastest and the polarization is vertical, namely in the direction of propagation. The event H1 in Fig. 2.5b is slower and its polarization is horizontal, normal to the direction of propagation. Therefore

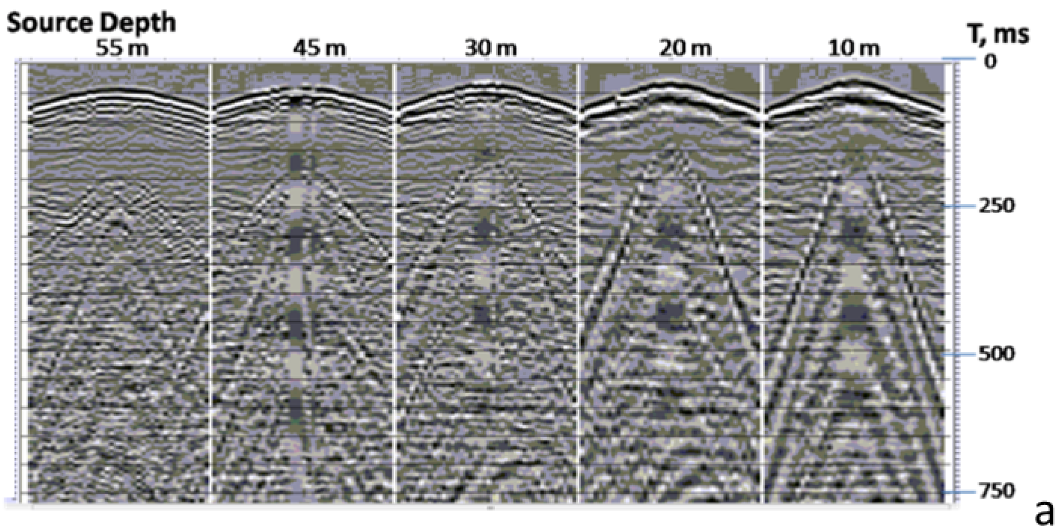

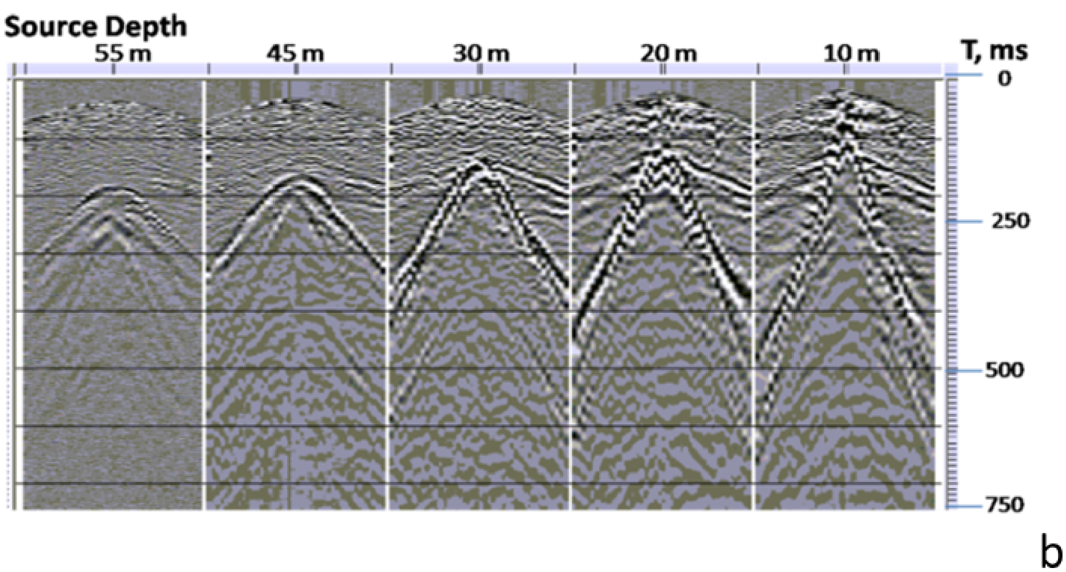

Figure 2.5: Records for various source depths: 55, 45, 30 , 20 and 10 m. (a) Vertical component (b) Horizontal component.

the First Breaks (FB) on the vertical component at short offsets are direct P-wave, and the strong events H1 in the horizontal component must be direct S-waves, both generated by the explosive sources.

S-waves generated by explosive sources are not generally identified in seismic exploration, and they are presumed to be negligible. However the literature provides theoretical models of S-waves generated by explosive sources, e.g. Heelan (1953) and Lee and Balch (1982) (see Appendix B). Real data examples have been reported too, see e.g. White and Sengbush (1963) and Lash (1985), and more recently Hardage and Wagner (2014). Ermolaeva and Stewart (2017) provide an analysis of SP waves (generated as S and converted to P in the reflector), with modeling and processing, using conventional sources of energy. Interestingly, a classical paper on explosive energy sources, Sharpe (1942) p. 320, mentions an unexplained seismic event that could be S-wave in the analysis of experimental data.

Furthermore, tests for this hypothesis using the Dix NMO equation and modeling are shown below (section 2.4). In addition, the velocity model obtained later, based on this assumption, appears robust and consistent with information of other sources.

2.3.2 Velocity model by picking zero offset events

Picking zero offset arrival times to obtain a NSL velocity model is a well-known method for its application to P-waves. Accordingly, this method was applied here to P and S-waves. Thus, the S-wave velocity model was constructed from the events identified as S-waves in the previous section. Both arrival time results for P and S-waves are illustrated in Figure 2.6a. Picking was straightforward for P-waves, but proved more difficult for S-waves. It was particularly hard for depths shallower than 20 m, which can be attributed to other events interfering (see e.g. the 10 m depth source in Figure 2.5b for illustration). Additionally S-wave events exhibit decreasing amplitude approaching zero offset, as shown in Figure 2.7b. By the way, this decreasing amplitude agrees with the theoretical model of Lee and Balch (1982), as shown in the Appendix B).

The resulting velocity model is illustrated in Figure2.6(b), with the values displayed in Table 2.1. It shows a sharp velocity increase for P-waves at about 5 m depth, whereas the S-wave velocity increases more gently with depth. This result matches the expected near surface behavior, related to the difference in response between P and S-waves to the water table, as stated in section 2.1.2 (Stümpel et al., 1984). The V_P/V_S ratio spans between 8 (the shallower) and 3 (the deeper), agreeing with the expectations for the NSL.

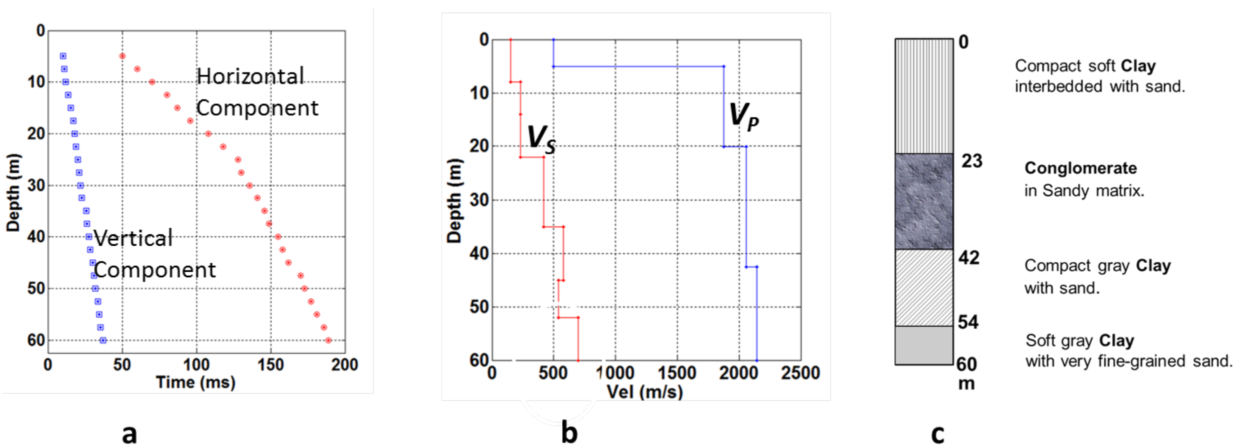

Figure 2.6: V_P and V_S from zero offset arrival times, and their relation with the lithology: (a) Zero offset arrival time picking (b) Resulting velocities (b) lithology from Fig. 2.4 at the same scale, for comparison.

The S-wave velocity shows more variations than the P-wave, and a probable *velocity inversion* can be identified in Figure 2.6b, between 44 and 52 m depth (even though it can be considered to be within the range of uncertainty). A simpler S-wave velocity model can be enough to correct the S-wave statics, namely the reflection arrival times from deeper interfaces. A velocity inversion could be correlated with the stratigraphic profile in Figure 2.4.

Depth (m)	V_P (m/s)	V_S (m/s)
0	0	0
0	500	170
8	1800	230
14	1800	230
22	2000	420
35	2000	580
45	2200	540
52	2200	700
60	2200	1200

Table 2.1: Velocities V_P and V_S obtained from the uphole analysis for the NSL.

2.3.3 Velocity model by tomography of the uphole

Tomography is a method to obtain a velocity model from arrival time measurements. It starts with a simple 1-D model, and iteratively finds an improved model (2-D or 3-D) searching for the minimal difference between the time calculated (by using ray tracing) and the observed arrival times (see e.g. Shearer, 1999). The input experimental data, namely the observed arrival times, requires reliable identification and picking of the seismic events of interest.

A velocity model was generated with tomography by picking the arrivals at the receivers to 50 m offset. Figure 2.7a illustrates the picking of the events for two depths, 45 m and 42.5 m, and Figure 2.7b shows the amplitude variation with offset for the 45 m depth event. The model resulting from tomography of the uphole data is illustrated in Figure 2.8. Vertical and horizontal scales are equal. The borehole is located at 50 m in the horizontal direction (x) and the maximum offset is 50 m. Depth is referred to the land surface at the borehole location. The initial 1-D model used the result of zero offset picking, namely the S velocity in Figure 2.6b. Only two iterations were required to obtain a result with negligible error, which supports the reliability of the previous 1-D model.

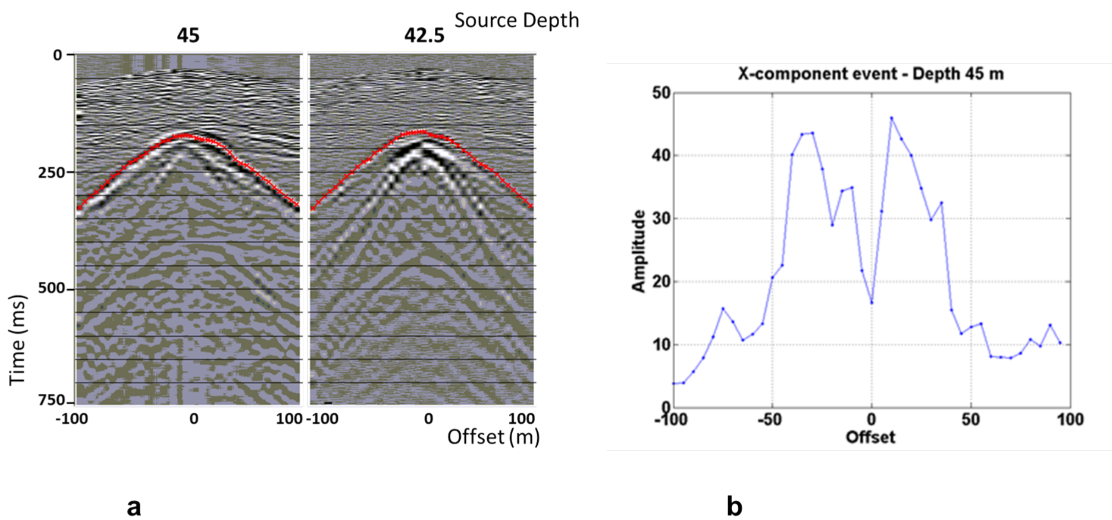

Figure 2.7: Direct S-wave picking and amplitude variation with offset: an example. (a) Records for sources at 45 m and 42.5 m depth, picking the event identified as direct S-wave. (b)Amplitude variation with offset of the 45 m depth event. Notice the decreasing amplitude at shorter offset.

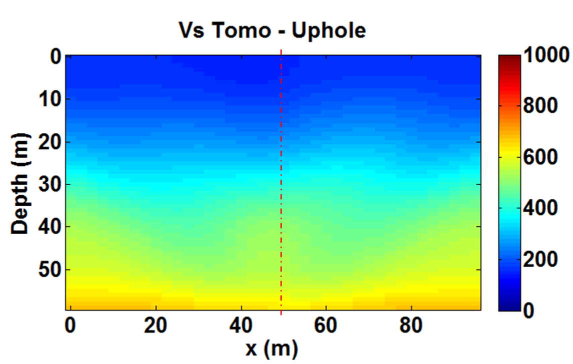

Figure 2.8: V_S obtained from direct S-waves using Tomography.

2.4 Test of hypotheses and the resulting velocity models

Two tests for the methodology and the uphole velocity model obtained follows. Forward modeling based on the velocity forms the background for both. In the first case a simple model is assumed, and the resulting arrival times compared to the real data, and in the second case elastic modeling allows us to compare the effect of the source, assuming a borehole explosion compared to a purely radial explosion.

2.4.1 Experimental arrival times compared to NMO

A test for the velocity field is to calculate the arrival-time/offset curves for a number of source locations, by using the velocity model obtained, and the NMO equation for a borehole. This relation, derived from the Dix Equation (Sheriff and Geldart, 1995), reads:

$$t_x = \sqrt{\left(\frac{z_s}{V_{avg}}\right)^2 + \left(\frac{x_r - x_s}{V_{rms}}\right)^2} \tag{2.1}$$

where z_s is the source depth, x_s and x_r are source and receiver surface locations, V_{avg}, is the *average velocity* and V_{rms} is the *RMS velocity.* These velocities are

$$V_{rms}^2 = \frac{\sum_{i=1}^{n} V_{Si}^2 t_i}{\sum_{i=1}^{n} t_i} \tag{2.2}$$

and

$$V_{avg} = \frac{\sum_{i=1}^{n} V_{Si} t_i}{\sum_{i=1}^{n} t_i} \tag{2.3}$$

where t_i is the time spent through layer i, namely

$$t_i = z_i / V_i$$

with z_i its thickness and V_i its velocity.

Results of this analysis are shown in Figure 2.9, where the resulting offset-arrival times are plotted over the seismic data gathers for source depths of 45 m (Figure 2.9a) and 10 m (Figure 2.9b). Agreement can be observed between calculated and recorded arrival times. However the 10 m depth result is less obvious, and many interfering events can be observed for large offsets.

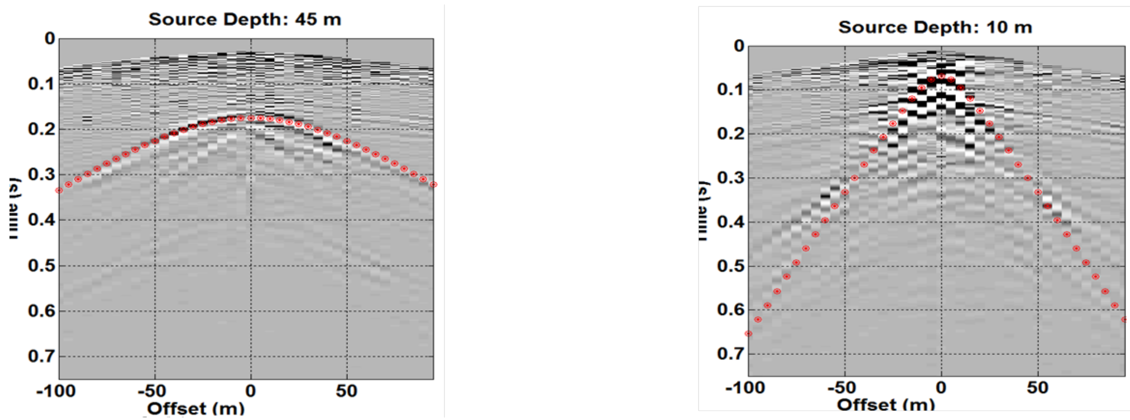

Figure 2.9: Comparison of time calculation using the NMO equation with field data. Arrivals calculated according to the NMO equation are displayed over the field seismic data for comparison. Horizontal component using two source depths as examples. Source depths are (a) 45 m, (b) 10 m.

2.4.2 Borehole source signature from real data and from FD modeling

Synthetic data using the Finite Difference elastic 2D method were generated based on the velocity field obtained previously, comparing the absence and the presence of an water filled uphole. A borehole, assuming a saturated, poorly consolidated medium, was located in the midpoint, with a diameter of 0.5 m (grid size required for the calculation), and assuming an acoustic low velocity medium inside . As in the real data, sources are located in the borehole and receivers are located each 5m on the flat surface, up to 100 m offset. The energy source was a zero offset 25 Hz Ricker wavelet. The resulting record for the 10 m depth source is shown in Figure 2.10a, together with the resulting record in the case of no borehole, in Figure2.10b. Notice the resemblance of the main features of Figure 2.10a when compared with the real data, in Figure 2.11. This result also supports the hypotheses about the effect of the borehole in the generation of the seismic data.

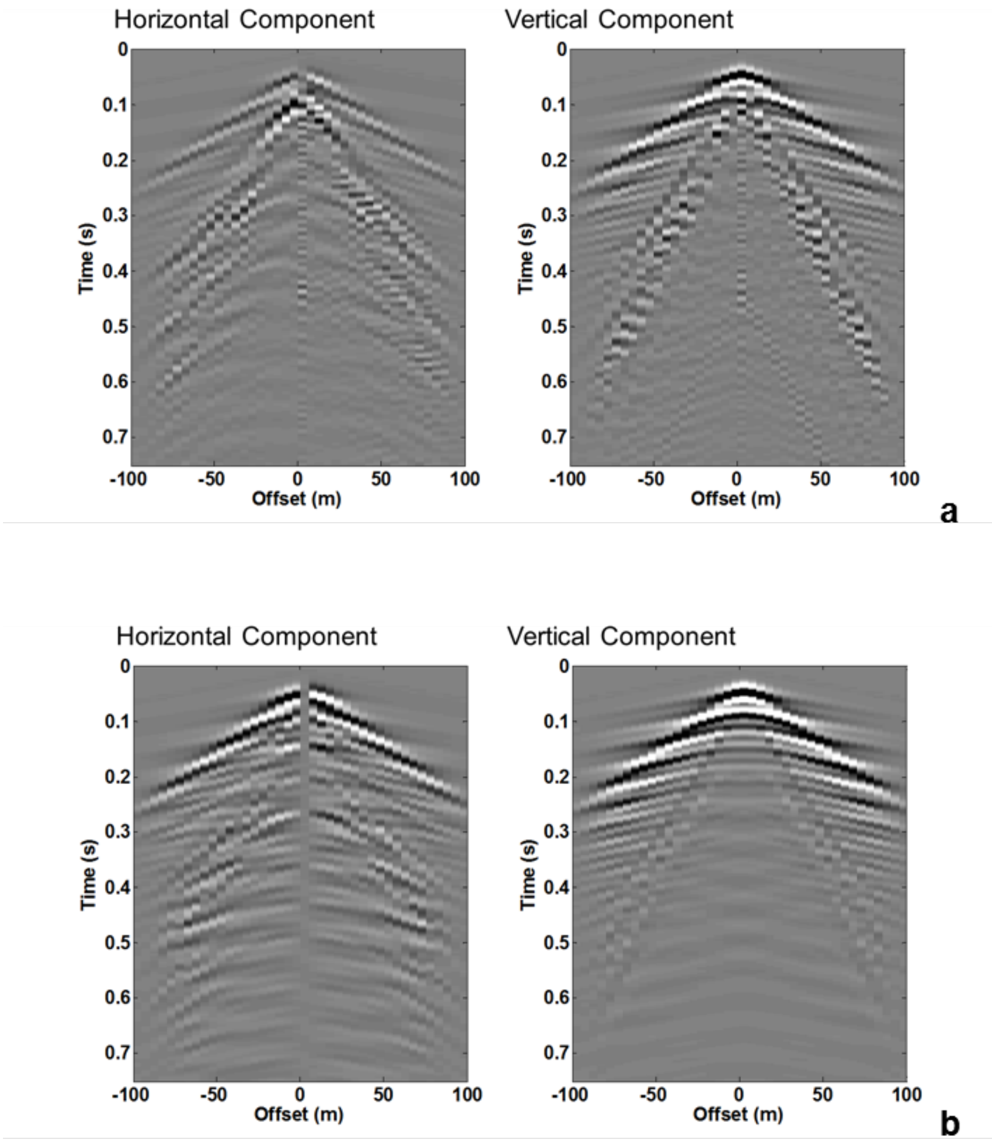

Figure 2.10: Comparing FD modeling of the 10 m depth shot with and without a borehole. Left: horizontal component. Right: vertical component. (a) Including a 0.5 m diameter borehole. (b) Without a borehole. Compare with Figure 2.11.

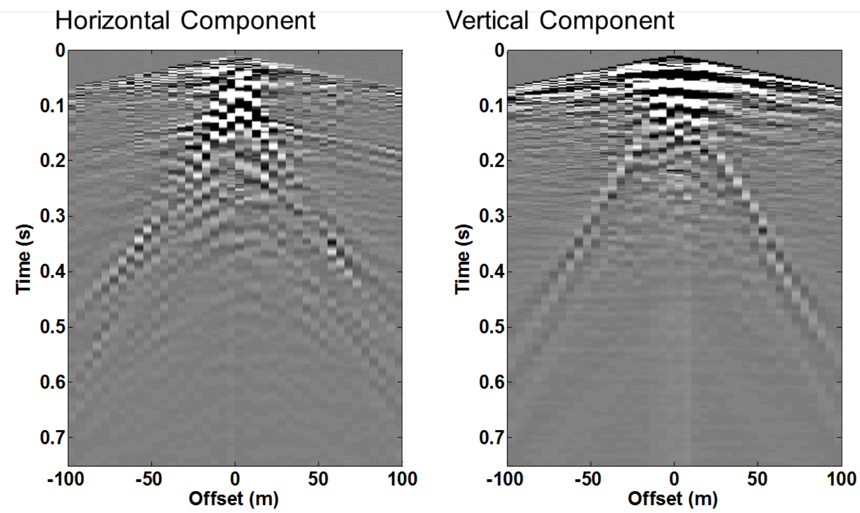

Figure 2.11: Uphole data from the 10 m depth source Left: horizontal component. Right: vertical component.

2.4.3 The radiation pattern

Lee and Balch (1982) define the theoretical model of irradiation caused by an explosive source inside of a borehole filled with a fluid. Radiation patterns can be defined for P and S-waves, which depends on the properties of the medium. More information about this theoretical model is in Appendix B. In the following an analysis of the radiation pattern is carried out on the real data of the uphole. The 25 m depth shot was selected for this purpose.

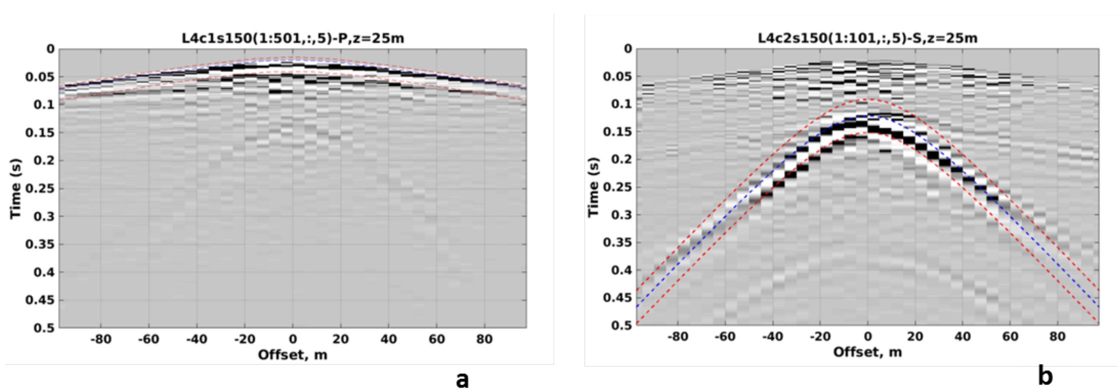

Figure 2.12: Real data 25 depth shot: (a) Vertical component and (b) Horizontal component

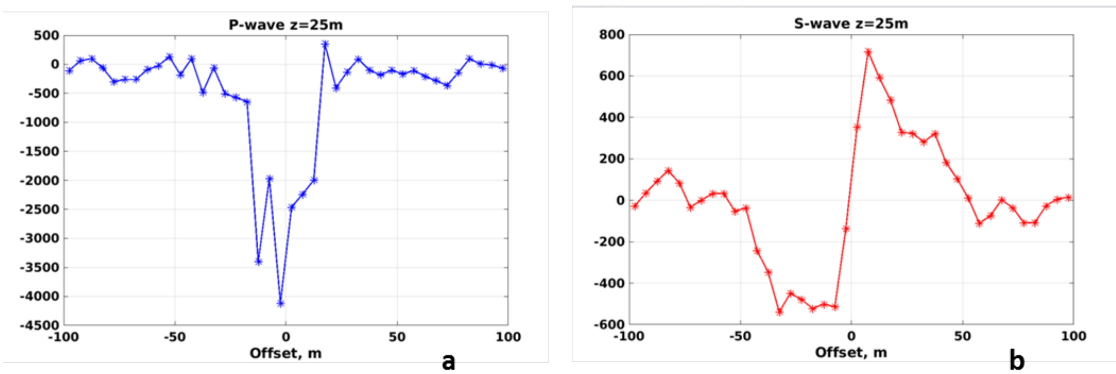

Figure 2.13: Real data amplitude pattern: amplitude summation at a gate corresponding to the arrival of direct events, for the 25 m depth shot: (a) Vertical component (P-wave); (b) Horizontal component (S-wave)

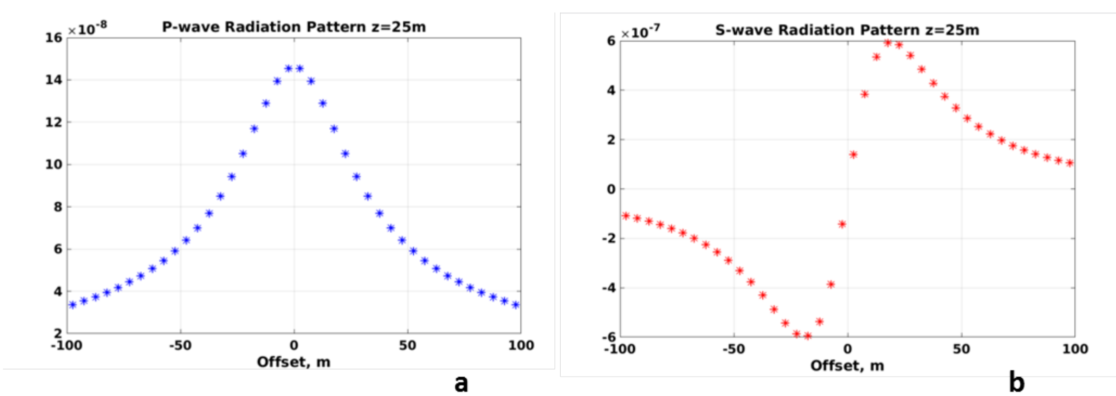

Figure 2.14: Theoretical radiation pattern for the 25 depth shot: (a) P-wave; (b) S-wave.

Figure 2.12 shows the two components of the 25 m depth shot. Notice the high-energy direct wave events, P-waves in the vertical component (Figure 2.12a) and S-waves in the horizontal one (Figure 2.12b), in agreement with the previous analyses. The gates used for the analyses are identified by red dashed lines. Figure 2.13 shows the amplitude summation for each gate, the vertical component in Fig. 2.13a and the horizontal component in Fig. 2.13b. Finally, Figure 2.14 shows the theoretical radiation patterns, according to the theory of Lee and Balch (1982), which corresponds to equations B.1 and B.2 in Appendix B. The real data results follow closely the shape of the theoretical calculations. It was assumed that the borehole is filled by a fluid with very low velocity (400 m/s). The opposite sign for the P-wave can be attributed to field polarity conventions.

Analyses of some other shots appear farther from the theoretical result. It can be related to interfering events, and to the analysis method. More work on these patterns can provide a better understanding of the model and about the methodology to obtain information from the uphole.

2.5 Relation between the uphole and the 2-D surface line seismic

As mentioned in section 2.2, a 2D 3C surface seismic line was acquired over the location of the uphole experiment. An analysis of the relationship between these two datasets follows, intended to investigate the application of this experiment to surface seismic exploration.

Figure 2.2 shows the location of the uphole (*uph-1*) and the seismic line. The surface seismic data were acquired using explosive sources of energy, with a charge size of 2700 g at a 10 m depth[2]. The nominal distance between sources was 40 m, and the receivers were separated by 10 m; the offset source-receiver distance ranges from 10 m up to 6000 m.

[2]Notice however that this depth corresponds to the bottom of the hole, since the source is really a cylinder with about 2 m length.

2.5.1 Shot records comparison

Analysis of the relation between the two experiments was carried out by comparing two analogous shot records. The records selected were: on the surface line, the closest shot (about 20 m) to the uphole location, and on the uphole, the 10 m depth shot. There were selected 100 m offset and 0.8 s time in the surface data. The surface line horizontal and vertical records are illustrated in Figure 2.15, and the uphole records are in Figure 2.16.

The surface data show lower frequencies and higher amplitudes, which can be expected taking into account the energy of the source (about 20 times stronger than the uphole). Arrival times and their relation to offset allows us to identify and find relations between events. Relevant events are labeled with numbers in both Figures to facilitate the following analysis. Some events are identified in one of the records but not in the other, such as 1 and 4 in the surface data and 5 in the uphole data. Events 2 and 3 can be identified in both. Other events appear common in both, as number 2 in the horizontal component and number 3 in the vertical one.

Event 2 is apparently linear and runs 100 m between about 0.22 and 0.48 s, therefore its velocity is about 380 m/s. This is close to the velocity that has been identified as corresponding to the conglomerate in Figure 2.4, see Table 2.1, whose top depth is about 23 m. Taking into account that the source is at 10 m depth, and that the polarization is horizontal, it can be hypothesized that this is an S-wave refraction generated as a pure S-wave at the source. The origin of this event would be a reflection, whose minimal time would correspond to zero offset, which according to the velocities of Table 2.1 must be 0.17 s. This time is not far from the data of the experiment, about 0.2 s (larger than any possible P-wave). This supports our hypothesis.

Event 3 is also linear, with velocity about 250 m/s (100 m in about 0.4 s), which according to Table 2.1 and Figure 2.4 corresponds to the S-wave at the clay layer above the conglomerate. Therefore it may be a surface (Rayleigh) wave, taking into account its presence in the vertical component. It must be observed in the horizontal component too, however probably there are many events interfering there.

In addition, there are events that appear in the uphole data and are absent or hardly identified in the surface data. Noticeably, the direct S-wave marked by a red dashed-dotted curve (Figure 2.16a according to the calculated NMO in Figure 2.9) cannot be followed in the surface data (Figure 2.15a), which may be explained by a lack of sampling (see section 2.5.2). Additionally the uphole record shows hyperbolic higher frequency events, identified by number 5, which appear periodical, as expected for reverberations. Since they are polarized in the horizontal direction, they may be pure S-wave reverberations.

Two events that appear in the surface data and have not been identified in the uphole are number 1 in the horizontal component, perhaps a dispersive effect related to S waves, and number 4 in the vertical component, probably a mode of surface waves.

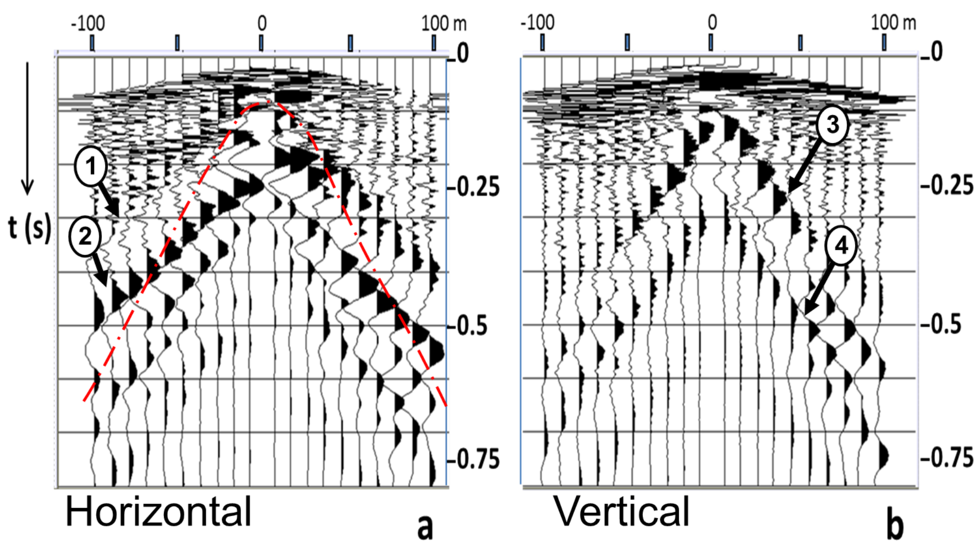

Figure 2.15: Detailed view of a land surface record, using a 2700 g dynamite energy source, for up to 100 m offset and up to 0.8 s. (a) Horizontal component (b) Vertical component.

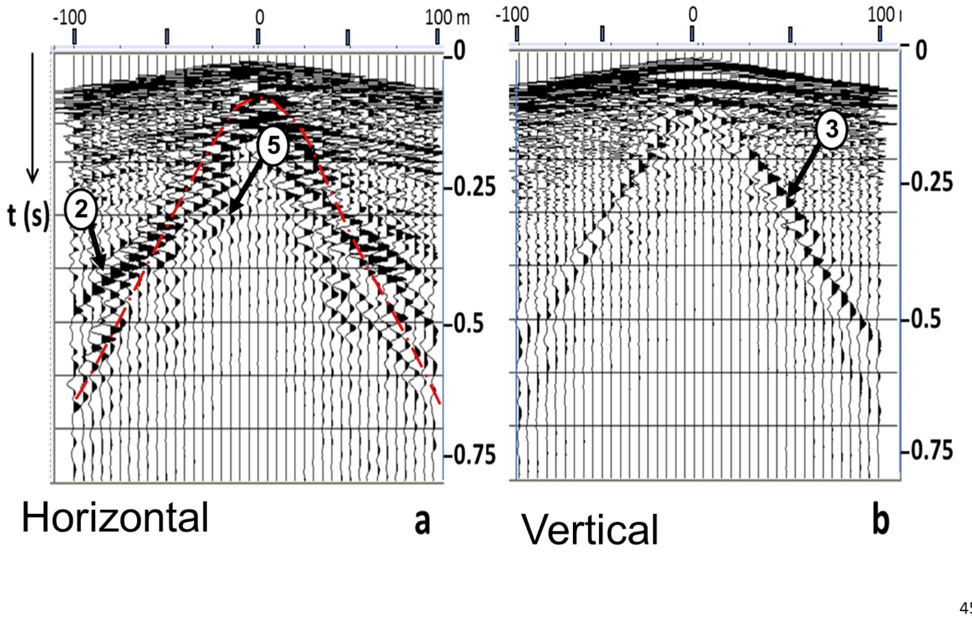

Figure 2.16: Detailed view of a borehole record, to compare with the land surface record, Figure 2.15, using a 150 g dynamite energy source (a) Horizontal component (b) Vertical component.

2.5.2 Velocity from tomography of the surface 2-D line

The 2D-3C seismic line data provide refraction events, thus it is possible to obtain a NSL velocity model for the S-wave using tomography. Figure 2.17 shows a shot record from the 2D seismic line, Figure 2.17a is the horizontal component and Figure 2.17b the vertical component. The events marked by their velocity in Figure 2.17are identified as S-wave refractions, which is also supported by the analysis of the previous section (Figure 2.15, event number 2).

The velocity model resulting after tomography of these 2D line refractions is shown in Figure 2.18. The color scale is the same as in the uphole tomography (Figure 2.8). There is a 20 times exaggeration in the vertical scale. The thick black line identifies the earth's surface topography. The arrow marks the uphole location (Uph-1). V_S from the uphole tomography (Figure 2.8) is shown above the uphole location, and its squeezed version (with 20 times vertical exaggeration) is set in the line tomography at its true location. Notice agreement between both velocity models, supporting the reliability of these results.

However there is a noticeable difference: the slower velocity (darker blue) in the shallower zone from the uphole tomography is about 150 m/s, whereas the velocity from the surface data tomography at the same zone is over 220 m/s (pale blue). There is an explanation for this difference based on the receiver separation of 10 m of the surface data, compared to 5 m separation of the uphole receivers. According to the sampling theorem, the Nyquist wavelength (λ_{x_N}) that can be properly sampled would be 20 m in the surface and 10 m in the uphole. It we assume a dominant frequency of 20 Hz, the velocity would be

$$V_{crit} = f_{dom} \times \lambda_{x_N} = 20Hz \times 20m = 400m/s$$

for the surface data and similarly $200m/s$ for the uphole data.

Therefore it is likely that the uphole data properly sample the low velocity events, and that the surface data do not. This reveals a shortcoming of the surface data for obtaining an accurate velocity model of the NSL.

.

2.6 Discussion

Low energy explosive sources inside a borehole generated seismic events which were identified as direct S-waves on the horizontal component record, which are not commonly identified in field data. As evidence supporting this claim, there is horizontal polarization, a polarity flip across zero offset, and large amplitudes (losses are mostly associated with reflections or mode conversions). In addition, theoretical models support this fact, which also explains the amplitude variation with offset of these data (Fig. 2.7b).

A 1-D S-wave velocity model was obtained from picking zero offset arrivals, a method used commonly for P-waves. However the picking was laborious, requiring numerous trials and errors, since the identification of the right arrival event for S-waves is not obvious. It is

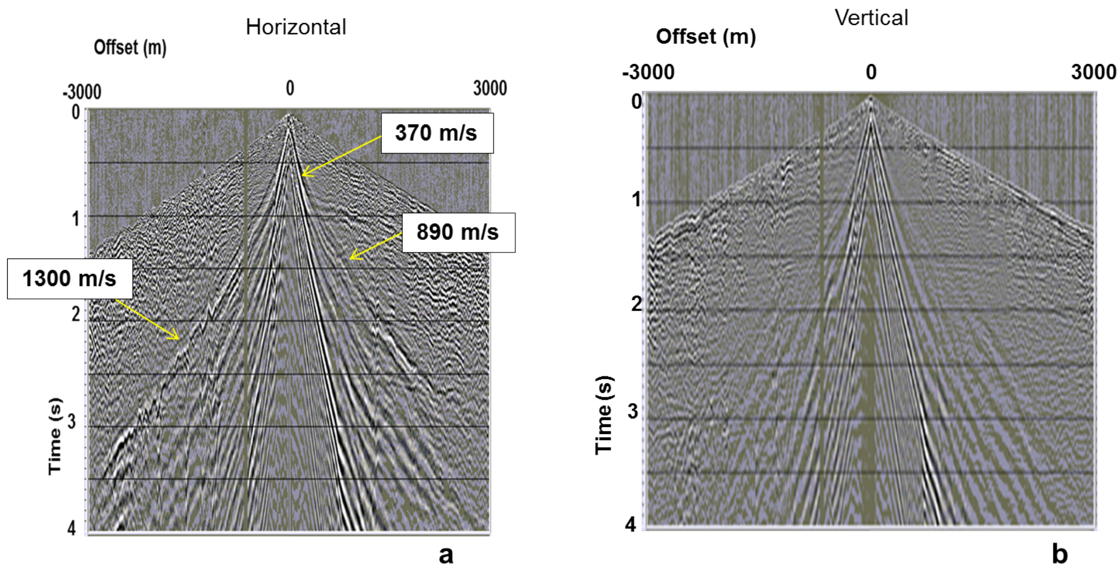

Figure 2.17: Typical records of the surface data: (a) horizontal component and (b)vertical component. The labels with velocities mark the event identified as S-wave refraction.

even harder for shallower data (less than 20 m depth), since there are many events interfering. Despite these challenges, the NSL V_S model obtained is reliable, since it agreed with both seismic and lithological data. Furthermore, the V_S model allowed the calculation of arrival times and the generation of synthetic records, that agreed with the real data.

The surface 2D line data shows higher amplitude and lower frequency than the uphole data, but otherwise, there is strong similarity between them. Thus, S-wave refractions were identified in both data sets, therefore S-waves generated by the explosive sources can be deduced. However the direct S wave is not apparent. Taking into account that the surface line source is about 20 times the magnitude of the uphole source, more destruction and plastic deformation is generated, hence probably the borehole theoretical model proposed by Lee and Balch (1982) is less appropriate. The model proposed by Sharpe (1942) sets a spherical *equivalent cavity* with center at the explosion point, that includes the destructive and plastic deformation caused by the explosion, and P-waves generation. On the other hand Miller and Pursey (1954) propose a theoretical source model on a free surface that includes

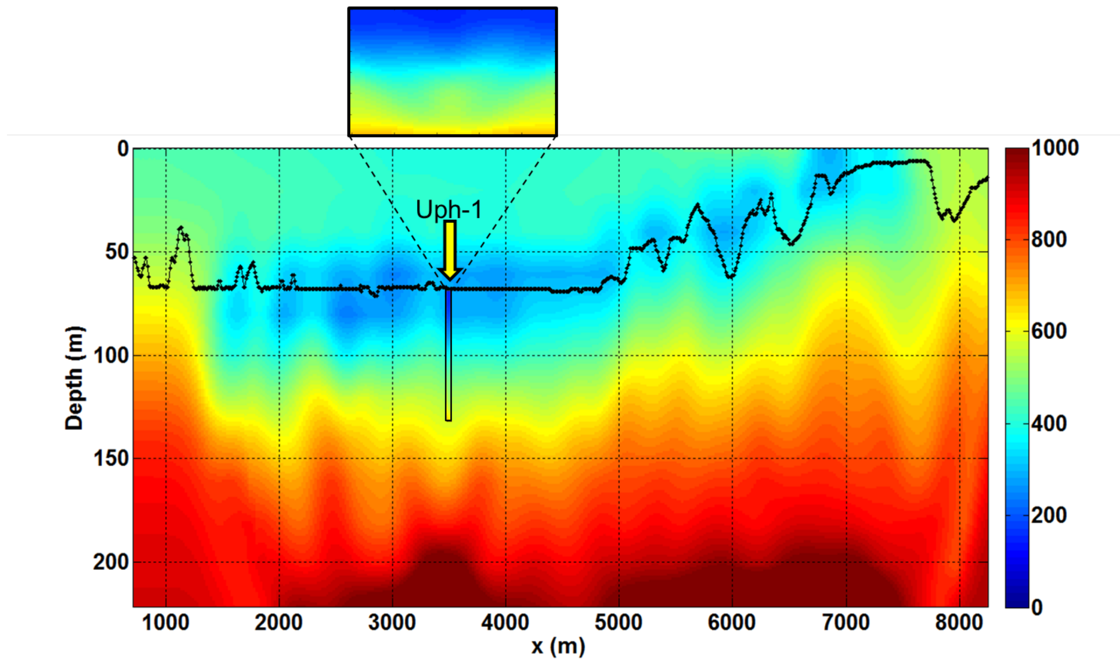

Figure 2.18: V_S of the 2-D seismic line obtained from tomography. There is a 20 fold exaggeration in the vertical scale. The arrow marks the uphole location (*Uph-1*). V_S from the uphole tomography (Figure 2.8) is shown above the uphole location, and its squeezed version (with 20 times vertical exaggeration) is inserted in the line tomography at its true location. Notice the slower velocity (darker blue) in the shallower zone from the uphole tomography (see the text for an analysis).

also a S-wave pattern of radiation. Although the observed S-wave refraction supports pure S-waves generated by explosive sources, they probably do not correspond exactly to the previous theoretical models. Field experiments (analogous to Suarez and Stewart, 2009) and theoretical studies may enlighten us about this phenomena.

The previous result supports using S-wave refractions tomography on 2D line data to obtain a V_S model. The resulting NSL V_S model from the 2D line tomography agrees closely with the uphole data, except in the shallower zone with velocities below 200 m/s, a disagreement maybe caused by the sparse sampling in the surface line (Section 2.5.2). This shortcoming is significant, since the shallower low velocity zone generates much of the statics delay. Thus, the surface line cannot provide a complete model of the NSL for statics correction , and the uphole and surface line data are complementary to this purpose.

2.7 Conclusions

- Events on the horizontal component of an uphole record were identified as S-waves generated by explosive sources inside the borehole.

- A 1-D near-surface V_S model was obtained using these events, by picking zero offset arrivals. The zero offset S-wave arrivals identification is harder than for P-waves. The shallower part of the record is less reliable, due to the interference of other seismic events.

- However a reliable V_S model was obtained, tested by the NMO equation and by FD modeling. It also correlates properly with the lithological profile.

- Based on the previous model, and using tomography, a 2-D V_S model was obtained, extended to 50 m offset. Tomography of the surface line using events identified as S-wave refractions generated another V_S model, which closely resembles the uphole result.

- However the surface line tomography shows higher shallower (less than 20 m depth) velocity than the uphole. The uphole appears more reliable, since the surface line sampling appears inadequate for that low velocity.

- Information on the near surface S-wave velocity field from upholes can be related to surface reflection seismic data to generate a more reliable near surface model, extended to a larger zone. Tomography appears as an appropriate technique to obtain velocity information from these surveys.

- Comparing to the uphole results, a nearby shot record of the surface 2D 3C line data with a similar charge depth shows lower frequency and higher amplitude. However events related to S-waves such as refractions and surface waves can be identified in both.

- These results support the generation of S-waves by explosive sources in 2D 3C land surface multicomponent data, therefore the possibility of taking advantage of them in exploration. It agrees with recent reports that identify pure S-wave reflections generated by conventional vertical P-wave sources (e.g. Hardage and Wagner, 2014; Ermolaeva and Stewart, 2017).

Chapter 3

A method for PS-wave receiver statics correction

3.1 Introduction

Recasting Section 2.1, the NSL in land causes delay times in seismic waves, which are a challenge for data processing (see Section 2.1.3); statics correction is the method developed to deal with the time delay on seismic events affected by the NSL. Additionally, since S-waves are slower than P-waves, and are not affected by fluids, the effect of the NSL on S-waves is more severe (Section 2.1.2). This is a serious issue for PS-wave processing (e.g. Garotta, 1999), and hence the subject of interest by academic and industry researchers (e.g. de Meersman and Roizman, 2009; Al-Dulaijan and Stewart, 2010; Cova, 2017).

This chapter addresses statics correction for PS-waves. I begin with an overview of statics correction methods, illustrated first by their application to PP-waves, and then to PS-waves. Then, I introduce a new method for the statics correction of the receiver for PS-waves, aiming to overcome current shortcomings. The method is presented and discussed with a test on synthetic data, and finally it is applied to real data to illustrate its potential benefits.

3.2 Statics correction methods

Statics correction was developed first for the PP-wave seismic method, providing effective and robust results. As a result, all seismic data are referred to a flat plane, which is a common elevation without the NSL problems. [1] This flat plane is known as the *reference datum.*

[1]The objective, quoting Sheriff (1991), is "to determine the reflection arrival times which would have been observed if all measurements had been made on a (usually) flat plane with no weathering or low-velocity material present".

Therefore, statics correction must remove or add time to honor the datum, conforming as much as possible to the local media properties.

Statics correction are based on the fact that, because of the low velocity NSL, waves arrive close to normal to the surface, which is a good approximation if the NSL has a low velocity compared to the underlying consolidated rock, if it is not very thick, and if the topography is relatively flat. Thus, the next two assumptions arise:

- The arrival ray is normal to the surface.
- As a consequence, the time shifting is assumed to be *surface consistent*, that is to say, it depends only on the surface location, regardless of any other factor like the source-receiver distance (*offset*).

The name *statics correction* implies that only a time shift (a *static* shift) applies to all trace samples, immaterial of their arrival time.

Two statics correction methods commonly applied to PP-waves are introduced in the following. They are identified as *datum statics* and *residual statics* (Cox, 1998). Both play a complementary role in the solution of the problem, and are guidelines for PS-wave methods. More extended explanations and practical examples can be found in Yilmaz (2001) and Cox (1998), among others.

3.2.1 Datum statics correction

The *datum statics* method applies a correction based on a model of the NSL seismic wave, i. e. velocity and thickness. Refraction is a common way to obtain this velocity model, hence it is also known as *Refraction Statics.* The reference datum rarely coincides with the bottom of the NSL, hence the depth difference must be replaced with a time shift using an approximate velocity known as the *replacement velocity.*

The procedure is as follows:

1. Find a model of the NSL thickness and velocity. It can be obtained from delays to refraction arrivals or by using uphole information (Cox, 1998).

2. Calculate the time delay to the base of the NS-LVL. It is the layer thickness at that location divided by its velocity.

3. Calculate the time shift to the reference datum. It is the distance between the NSL bottom and the datum divided by the replacement velocity.

Datum statics normally corrects most of the NSL anomaly. However it is usually not enough, and an additional correction is normally required, which is done through the *residual statics correction*.

3.2.2 Residual statics

Residual statics is based on the coherence of seismic reflections, instead of the NS velocity model. The rationale is that since the NSL anomalies deteriorate the stacking of the reflected events, improvement of stacking as a function of the NSL delay time anomalies improves the statics correction.

Therefore, a relationship between the reflection arrival time and the NSL anomaly is required. This relationship is provided by the surface consistent model which, following Schneider (1971), allows defining the traveltime for a seismic event generated at source s and detected at receiver g as

$$\begin{aligned}\text{Traveltime } s\text{-}g \quad &= \quad \text{Normal incidence time} + \text{Moveout} + \text{Shot statics} + \text{Receiver statics} \\ &+ \quad \text{Estimation error} \quad . \end{aligned} \tag{3.1}$$

Equation 3.1 suggest the analysis of arrival time components by data *domains*, which correspond to different ways of gathering the traces in data subsets or *gathers*. In fact, each trace is related to a source, a receiver, an offset and (for PP-waves, according to the CMP model) a reflection point or CMP, which define a domain. Then, the trace can be grouped with the others of the same domain. The following domains are identified and illustrated in Figure 3.1: Common Mid Point gather or CMP, Common Shot Gather or CSG, Common Receiver Gather or CRG, and Common Offset Section of COS (Yilmaz, 2001).

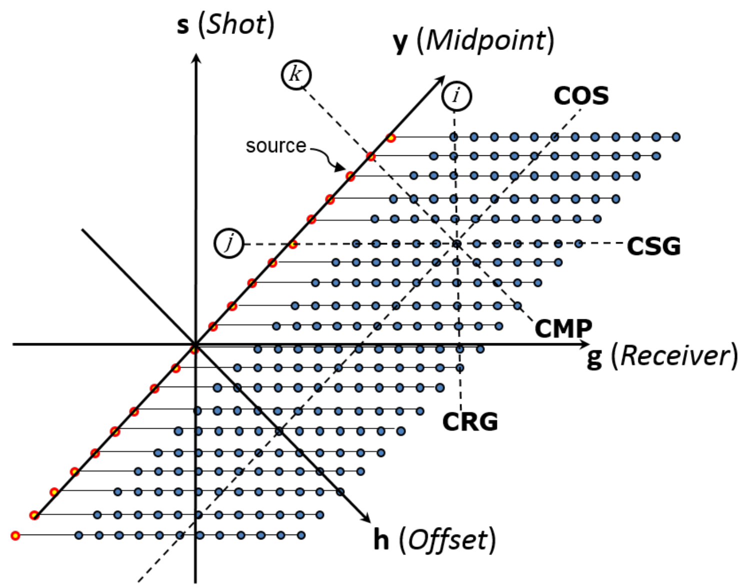

Figure 3.1: Stacking chart, illustrating the data domains of a 2-D seismic survey, as for the conventional seismic method. The horizontal coordinate corresponds to receiver locations, the vertical coordinate to source locations. Index i corresponds to a CRG, j to CSG, k to CMP. h_{ij} is the offset. (After Yilmaz (2001) and Taner et al. (1974)

The surface consistent principle of Equation 3.1 has been translated into expressions that allow numerical handling, such as the one presented by Taner et al. (1974):

$$T_{ijk} = R_i + S_j + G_k + M_k h_{ij}^2 \tag{3.2}$$

where R_i denotes receiver statics at the $i_t h$ receiver position. S_j denotes Source statics at $j_t h$ source position. G_k denotes an arbitrary time shift for kth CMP gather, also known as *structural geology* component (or normal incidence time). M_k denotes residual NMO component at kth CMP gather, and h_{ij} denotes source to receiver distance[2]. The CMP corresponds to the index k, the CSG to the index j and the CRG to the index i.

[2]Taner et al. (1974) use $(j - i)$ instead, which is good enough for the CMP model.

The NMO time delay is large compared to the residual statics delay, then NMO-corrected data are required, hence M_k in equation 3.2 corresponds to a residual NMO correction error. Since the NMO correction requires a velocity model, and velocity analysis is affected by the statics correction, determining residual statics becomes an iterative process (see Fig. 1.5).

The time delay between two seismic traces can be obtained by the operation of *cross-correlation* (Taner et al., 1974), which quantifies the similarity between two time series (see details in Section 3.4.6). Under this approach a number of techniques have been proposed, such as Taner et al. (1974) and Wiggins et al. (1976). Ronen and Claerbout (1985) propose a robust method for noisy data that uses cross-correlations of seismic trace stacks as a statics improvement criterion.

3.3 Statics correction methods for converted waves

The basic ideas applied to statics correction in the conventional seismic method are also valid for converted waves. Since a converted (PS) wave propagates as a P-wave at the source side and as a S-wave at the receiver side, the source statics are already corrected during the PP wave processing. Thence the statics correction of PS wave can be abridged to the receiver S-wave statics correction. Nevertheless, this narrower problem has proved challenging. *Datum statics* and *common receiver stack*, two commonly used techniques to solve PS-wave statics, are presented in the following.

3.3.1 The datum statics method applied to PS-waves

This method is analogous to the method for PP-waves (section 3.2.1); it requires a thickness and velocity model of the near surface layer. Determining the velocity model is a critical step of this approach. Refraction analysis of S-waves have been investigated for this purpose (Schafer, 1993; Dufour et al., 1996; Zuleta-Tobon, 2012). Even though reasonable results have been obtained, S-wave refracted events are more difficult to pick than for first breaks picking for PP-waves. Additionally, as discussed in Chapter 2, this method can not obtain a good model of the usually quite significant very shallow NSL.

Surface waves have also been investigated to obtain the NSL S-wave velocity (e.g. Socco et al., 2010; Askari, 2013), with promising results reported. However, the horizontal resolution for this technique is not always good enough, and there are research efforts addressed at improving it.

3.3.2 The common receiver stack statics ($CRSS$) method

According to Equation 3.2, if the source statics S_j, the NMO correction, and the geological component G_k delay are known, the remainder must be the receiver statics correction. Hence, after subtracting all the other terms, R_i would be the only remaining anomaly, which can be measured in a receivers stacked section, a *Common Receiver Stack* or *CRS*.[3] This is the principle of a PS-wave receiver statics correction method, identified in the following as the Common Receiver Stack Statics or CRSS method. This method has proved reliable in practical applications. This procedure can be represented by the equation:

$$R_i \approx T_{ijk} - G_k - M_k h_{ij}^2 \tag{3.3}$$

where R_i denotes the receiver statics at the ith receiver position. T_{ijk} denotes the total traveltime of the event k, G_k denotes the geological structure delay time, M_k denotes the residual NMO component at the kth CDP gather, and h_{ij} denotes the source to receiver distance.

The source statics S_j is set from the PP-wave processing (see Figure 1.5a); the NMO delay can be corrected using an approximation, such as CCP (Equations 1.12) or ACP (Equation 1.14) and a stacking velocity field V_C; the structural geology component can be removed if a guide reflection can be identified and there is a reasonable guess of its arrival

[3] Quoting Harrison (1992): "any time delay encountered by the S-wave energy on its way back through the near surface will be common to all traces collected by the receiver. .... A receiver delay can be obtained by applying that time shift which best aligns the summed receiver trace with its neighboring traces".

time. Notice that in this case k does not represent a midpoint but a PS reflection point, which changes with depth (i.e. with time), as illustrated in Fig. 1.6.

Such a guide reflection can be obtained from the PP seismic section, provided that it is also clearly identifiable in the PS data, and works as a guide to pick the delay time R_i in the CRS section. Thus, an iterative procedure alternating between velocity analysis and statics correction is set up. The final receiver statics R_i (and an improved V_C) corresponds to the flat reflector in the CRS section.

Cary and Eaton (1993) proposed a technique for PS-wave receiver statics correction, based on the same principles, and with an automated optimization algorithm analogous to Ronen and Claerbout (1985). This method appears less laborious and interpretative than the CRSS method. However, it also assumes a simple geology, and requires a velocity model for stacking.

3.4 Proposal: A method for PS-wave receiver statics using receiver gathers without stacking

3.4.1 Background: an approach to converted wave receiver statics without stacking

An appropriate V_S model of the NSL for datum statics is difficult to obtain, as mentioned above. Additionally, the very low shallow NSL V_S appears critical, and is even more difficult to obtain with conventional methods (Section 2.6).

Schafer (1993) carried out a test on datum statics compared with the CRSS method (section 3.3.2) for PS data, and found better result with the latter. Higher resolution appears as a key strength of this method, since it can obtain an independent value for each trace, therefore even adjacent receivers can have unrelated statics corrections, which can be explained by the horizontal heterogeneity of the NSL for S-waves (section 2.1.1).

However the CRSS method also has shortcomings. It depends on identifying a reflection, which may not always be available, specially at earlier stages of processing. Additionally, the reflection gathers result from simplified approximations, such as the ACP (equation 1.14), and requires a preliminary velocity model V_C. Hence arises a laborious process, with interpretative steps that involve subjective criteria, susceptible to errors. These properties prevent in particular a reliable application to complex settings.

A potentially rewarding approach is suggested by comparing two records of the horizontal component without PS-wave receiver statics correction but after the source (P-wave) statics correction. An example is shown in Figure 3.2. Presence of events can be noticed, which maybe correspond mostly to PS reflections. These events appear coherent and hyperbolic in the receiver gather (Figure 3.2b), but less so in the shot gather (Figure 3.2a). This difference can be attributed to the receiver statics. The same property can be noticed in adjacent CRGs. Hence there are many traces, and events in each trace, whose difference between adjacent CRGs is caused by S-wave receiver statics. Hence, should be possible to extract this differential statics by comparing CRG gathers trace-wise. This is the observation behind the method proposed in the following.

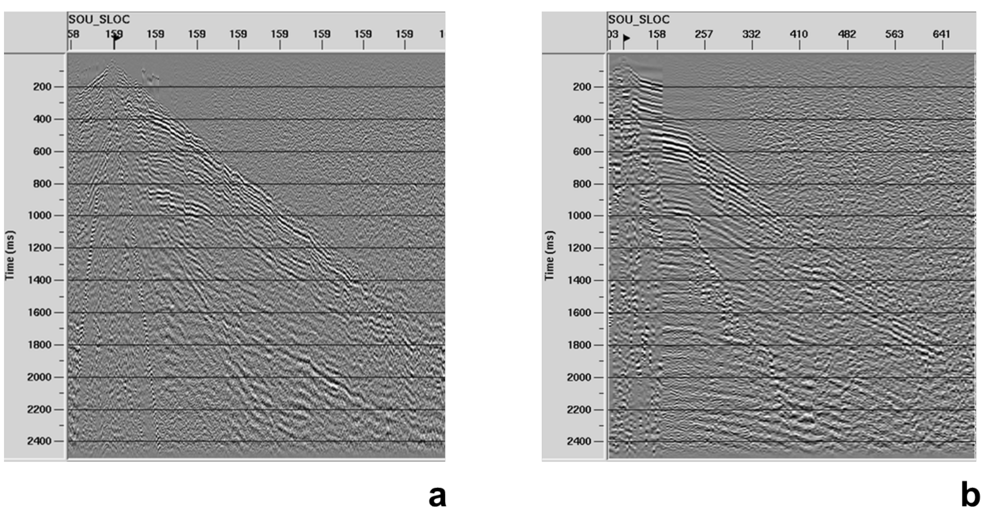

Figure 3.2: Comparison of horizontal component gathers after source statics correction: (a) Common Shot Gather (CSG) and (b) Common Receiver Gather (CRG).

3.4.2 Principles of the method

The proposed approach is close to the CRSS method, since it is based in the surface consistent approximation (equation 3.1), uses CRG gathers, and the receiver statics correction is obtained after separating out all other meaningful effects. However, while the CRSS method obtains the statics corrections from stacking the traces, the proposal is to obtain them without stacking. Thus, in the following the new method will be identified by the acronym CRGS for Common Receiver Gather Statics. There are publications with analogous techniques for conventional seismic data statics using prestack data in surface domains (CRG and CSG), e.g. Disher and Naquin (1984) (see Cox, 1998, Section 7.3).

According to the previous analysis, the receiver statics, R_i, can be obtained relating the appropriate pair of traces of two adjacent CRGs. This pair of traces are called *analogous* in the following. The delay time between these two traces can be represented by the surface consistent equation (equation 3.1) but using the relative delay time between the two analogous traces of adjacent receiver gathers, which we can call *differential delay time*, and symbolize by δ. Hence

$$\delta T_{ijk} = \delta R_i + \delta S_j + \delta G_k + \delta N_{ijk} \tag{3.4}$$

where δR_i denotes the differential receiver statics at the receiver position i_{th}. δS_j denotes the differential source statics at the source position j_{th}, and δG_k denotes the differential geological structure time shift for the kth reflection gather. δN_{ijk} denotes the differential NMO effect at the kth reflection gather with source j and receiver i.

Notice that I use N_{ijk} instead of $M_k h_{ij}^2$ for the NMO effect, taking into account that in the proposed method there is no NMO correction, therefore there is no residual NMO delay, but rather the total NMO delay time.

Figure 3.3 illustrates the NSL time delay (equation 3.4) for analogous traces in adjacent CRGs. The distance between receivers is Δg, and the distance between sources is Δs. The two adjacent receivers are identified by g_1 and g_2, and there is a NSL thickness jump between

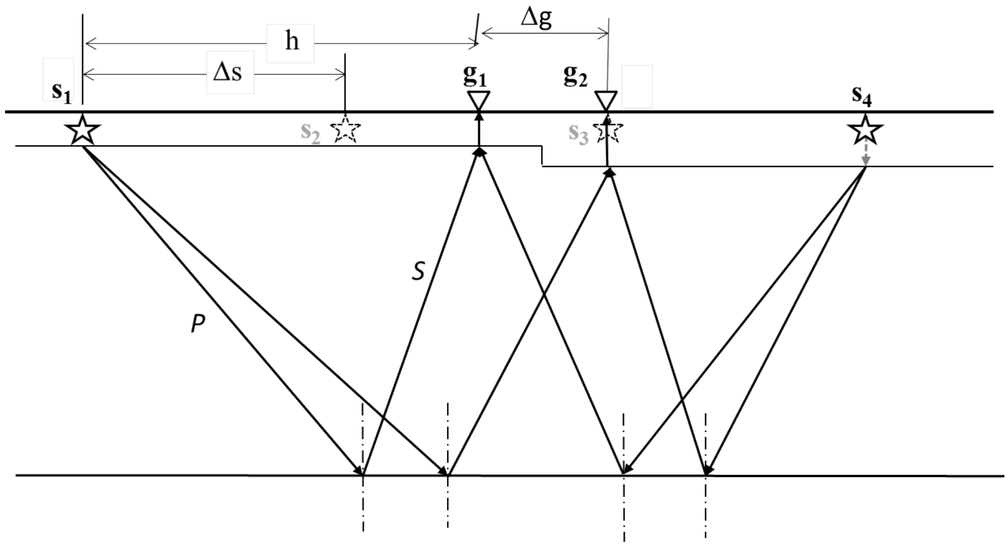

Figure 3.3: The PS events used for cross-correlation in the receiver statics algorithm. Each trace of a CRG is cross-correlated with the trace of the adjacent CRG corresponding to the same source. The differential time delay consists of the differential receiver and source statics, plus the offset and geological time delays.

them, which causes a NSL delay, which requires the statics correction. The Figure 3.3 also shows rays from two sources, identified by s_1 and s_4. A flat interface generates the PS-wave reflection.

3.4.3 Analysis of the delay time components in δT_{ijk}

As a first guess, the closer corresponding traces of two adjacent CRGs are the traces generated by the same source, as illustrated in Figure 3.3. The receiver statics time delay component can be obtained if the other components of the delay time were removed.

From PP-wave processing, the source statics S_j is already known, so it can be taken out, provided it has been applied. The geological component, δG_k, and the NMO component, δN_{ijk}, can be assumed to be negligible in principle, since they correspond to the differential change in a distance of the order Δg, which can be assumed to be small. The experimental analysis of section 3.5 supports this assumption for δG_k, but not for δN_{ijk}. The latter requires an additional correction that amounts to obtaining the same offset in both traces. Analysis of this issue and the method to correct it follows.

An simplified approximation of N_{ijk}, according to Equation 1.15, is

$$N_{ijk} = \sqrt{G_k^2 + \left(\frac{h_{ij}}{V_C}\right)^2} - G_k \tag{3.5}$$

where G_k is the zero offset arrival time of the PS wave event k, V_C is an RMS approximation to the PS wave velocity at the reflection k, and h_{ij} is the offset. Thus,

$$\begin{aligned}
\delta N_{ijk} &= N_{ijk} - N'_{ijk} && (3.6)\\
&= \left(\sqrt{G_k^2 + \left(\frac{h_{ij}}{V_C}\right)^2} - G_k\right) - \left(\sqrt{G_{k'}^2 + \left(\frac{h_{ij} + \Delta g}{V_C}\right)^2} - G_{k'}\right) && (3.7)\\
&\approx \sqrt{G_k^2 + \left(\frac{h_{ij}}{V_C}\right)^2} - \sqrt{G_{k'}^2 + \left(\frac{h_{ij} + \Delta g}{V_C}\right)^2} \quad , && (3.8)
\end{aligned}$$

where $G_{k'}$ corresponds to the geological delay caused by the second reflection point, which we can assume not too different from G_k. Hence the difference is caused by offset and reflection point distance between the two adjacent receivers.

Figure 3.4a illustrates two traces for the reflection events generated by the two sources indicated in figure 3.3, and recorded at g_1 and g_2. The differential delay time would corresponds to the receiver statics if both traces were analogous, i.e. if the other delay time components were negligible. However, a delay time caused by NMO is illustrated in Figure 3.4b. Notice that it depends on the direction, as can be noticed in Figure 3.3. Remember that the offset is

$$h_{ij} = g_i - s_j.$$

Assuming that the differentials are measured from left to right, the second trace offset is Δg longer if the offset is positive, and Δg shorter if the offset is negative, therefore the delay time caused at s_1 is a bit larger and the delay time caused at s_4 is a bit smaller than expected. Since these additional delays are present in every trace and event, a meaningful error is introduced in the measurements, as is tested later in the example of section 3.5.2.

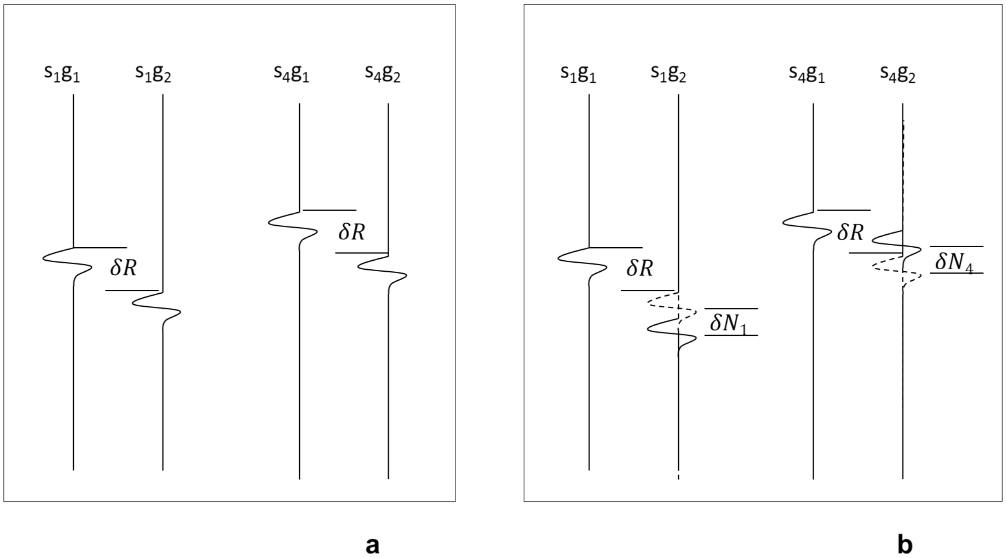

Figure 3.4: (a) Travel time of traces from adjacent receivers, g_1 and g_2, affected only for the receiver statics δR_i, for sources s_1 and s_4 (see Fig. 3.3). (b) An event travel time of traces from adjacent receivers affected by the differential NMO, symbolized by δN_j, additionally to the receiver statics δR_i.

3.4.4 About the structural component

The differential structural component, δG_k, can be assumed to be negligible. An explanation is that cross-correlation and stacking are applied to events of two traces which have the same surface consistent receiver statics R_i, but not surface consistent geology. Additionally, the reflection point between to analogous traces of adjacent receivers are about Δg apart, which can probably entail a negligible time delay caused by geology.

3.4.5 The differential offset compensation

A method to compensate for the differential delay generated by the offset and NMO consists of eliminating the offset difference. If both traces had the same offset there would be no delay generated by the NMO δN_{ijk}. We introduce interpolation here for this purpose, which is illustrated in Figures 3.5 and 3.6. Interpolation amounts to having virtual sources s_1^* and s_4^* in Figure 3.5, such that the offsets between s_1-g_1 and s_1^*-g_2 are equal, as for s_4-g_1 and

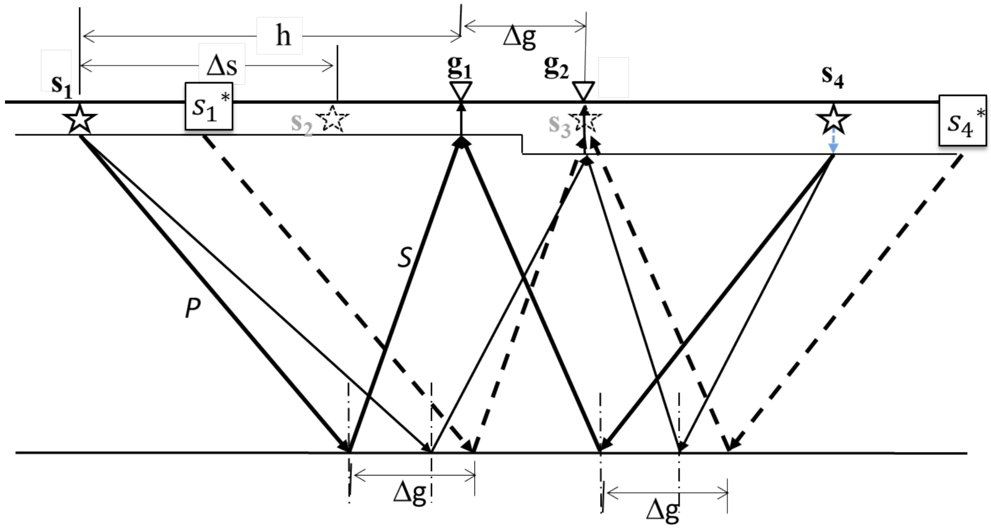

Figure 3.5: PS events in the surface consistent model used to correct the NMO delay: wave-paths for adjacent receivers and for events interpolated. s_1^* and s_4^* are the interpolated source locations that replace s_1 and s_4, such that the offsets to g_2 are equal to the offset to g_1.

s_4^*-g_2. Figure 3.6 illustrates the interpolation of the traces of a CRG, as a top view of a seismic spread. Interpolated traces correspond to the white stars (Figure 3.6b).

In this case the time delay δN_{ijk} is

$$\delta N_{ijk} = N_{ijk} - N^*_{ijk} \tag{3.9}$$

$$\approx \sqrt{G_k^2 + \left(\frac{h_{ij}}{V_C}\right)^2} - \sqrt{G_{k^*}^2 + \left(\frac{h_{ij}}{V_C}\right)^2} \quad , \tag{3.10}$$

whose difference is caused by the reflection point distance between two adjacent analogous traces of the same shot.

The τ-p transform was used for this interpolation. The τ-p transform, also known as *slant-stack*, transfers the seismic data from the *time-space* coordinates $(t-x)$ to the intercept time (τ)-ray parameter (p) domain, according to the equation:

$$u(\tau, p) = \int_{-\infty}^{\infty} u(\tau + px, x)\mathrm{d}x. \tag{3.11}$$

For more details see Appendix E. Since the τ-p transform is approximately invertible, it

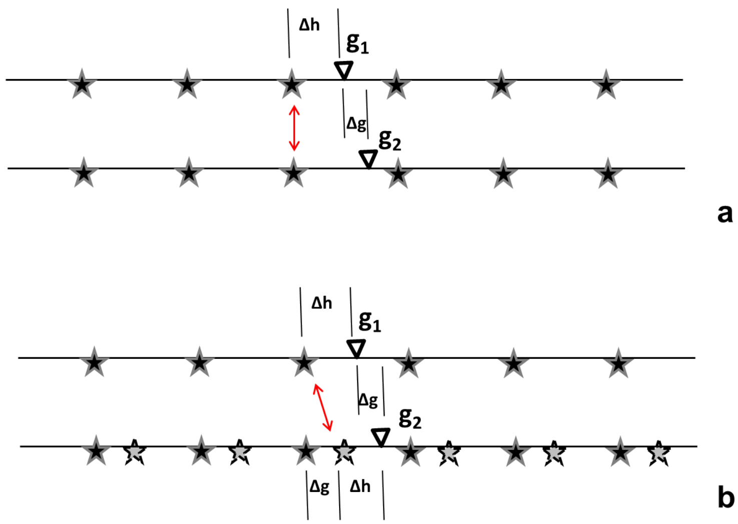

Figure 3.6: Trace interpolation illustrated by a top view of the seismic line.(a) the input data of a CRG with the receivers location (triangle) and the sources (black stars), (b) the interpolated trace locations, which amount for sources at the white stars. An example of traces that interpolate is shown by the arrow.

is possible to move the data back to the $t-x$ domain, after a convenient operation in the τ-p domain. In this case a simple re-sampling in the x domain is enough, such that the new offset of any trace in a CRG is the same as the offset of the analogous trace in an adjacent CRG.

3.4.6 Finding the delay time by cross-correlation

As shown in section 3.2.2, the relative time delay between two traces can be obtained from the cross-correlation between them (Taner et al., 1974). In the CRGS method, each trace of a CRG is cross-correlated with the analogous trace of the adjacent CRG. This is expressed by the equation

$$C_{g_1 g_2}(\Delta\tau) = \frac{\sum_{i=1}^{n_t} D_{g_1}(t_i) D_{g_2}(t_i + \Delta\tau)}{\sqrt{\sum_i D_{g_1}(t_i)^2 \sum_i D_{g_2}(t_i)^2}} \quad , \tag{3.12}$$

where $C_{g_1 g_2}(\Delta\tau)$ is the cross-correlation for the time delay $\Delta\tau$, ($\Delta\tau$ is the time shift between the two traces), and D_{g_1} and D_{g_2} indicate data of analogous traces for adjacent CRGs, with n_t time samples t_i.

The divisor in equation 3.12 makes for a normalized result, such that the maximum possible value is 1 for the case when both traces are identical (Li, 1997). Cross-correlation can have a misleading maximum at a nearby cycle, called *cycle skipping*, caused for example by the periodicity of seismic events. Cycle skipping can be attenuated by limiting the length of the input trace, as well as the range of the time shift variable. However it is not much a critical problem with this method, since a gateis not required, but the complete trace.

Depending on the selection of the traces identified by index g_1 and g_2 in Equation 3.12, there are two possible directions for the cross-correlation, namely toward the higher coordinate (lets say in the right-hand side direction) or toward the lower coordinate (left-hand side direction). Since D_{g_1} is fixed and D_{g_2} is shifted, then the corresponding cross-correlation $C_{g_1 g_2}$ must have the opposite sign for each direction. For the theoretical analysis and the examples in the following, the direction toward the higher coordinate (left to right) is assumed, unless otherwise indicated (see Figures 3.3 and 3.4).

Since $C_{g_1 g_2}$ measures the resemblance between traces, if they are analogous of adjacent receivers, then the delay between all of them must be the maximum cross-correlation, and equal to δR_i. Hence in principle, a *stack* of these cross-correlations must yield a more reliable delay δR_i, considering potential inaccuracies and possibly noise. Thus, δR_i is

$$\delta R_i = max \sum_{h=1}^{n_h} C_{i,h}. \tag{3.13}$$

where h is offset and n_h is the number of offsets.

Since the final receiver statics are relative to an assumed datum, it is obtained by summation of the differential corrections from the datum location. Assuming that the datum is at the location with index d, then the final receiver statics would be:

$$R_i = \sum_{j=d}^{i} \delta R_j \tag{3.14}$$

3.4.7 Statics correction data flow and comments on its application

A flow diagram that summarizes the method is shown in Figure 3.7. It is assumed that the calculations proceed "left-to-right" (see section 3.4.3).

Some comments about its application follow:

- We assume that the horizontal component has enough PS wave energy, even when not visible to the naked eye, which contributes to the cross-correlation.
- A long data gate to include as many PS wave reflected arrivals as possible leads to a more robust cross-correlation.
- The analysis could be improved by shaping a data gate to avoid strong coherent noise events such as surface waves and first arrivals (shallow refractions).

3.5 Test of the method using synthetic data

A test of this method on a synthetic model is now described. The synthetic data were generated using FD modeling. Figure 3.8 illustrates the S-wave velocity model, and Figure 3.9 the P-wave velocity. The x coordinate increases from left to right, and the z coordinate increase from top to bottom. The horizontal size is 1000 m and the vertical is 600 m. The surface is assumed to be flat, at z=75 m. The geology consists of two discrete sections, the NSL at the top and the consolidated rock below it.

The NSL P-wave velocity (Figure 3.9) is constant, whilst the NSL S-wave velocity (Figure 3.8) gradually increases with depth, from about 100 m/s at the surface to a velocity close to that of the consolidated rock. Five lateral zones were established, each one with a different NSL S-wave velocity and with thicknesses between 25 and 35 m, as shown in Figure 3.8b. In this way, we have four points where the NSL properties change, hence they require of an S-wave statics correction. The geology at depth is quite simple, composed of horizontal

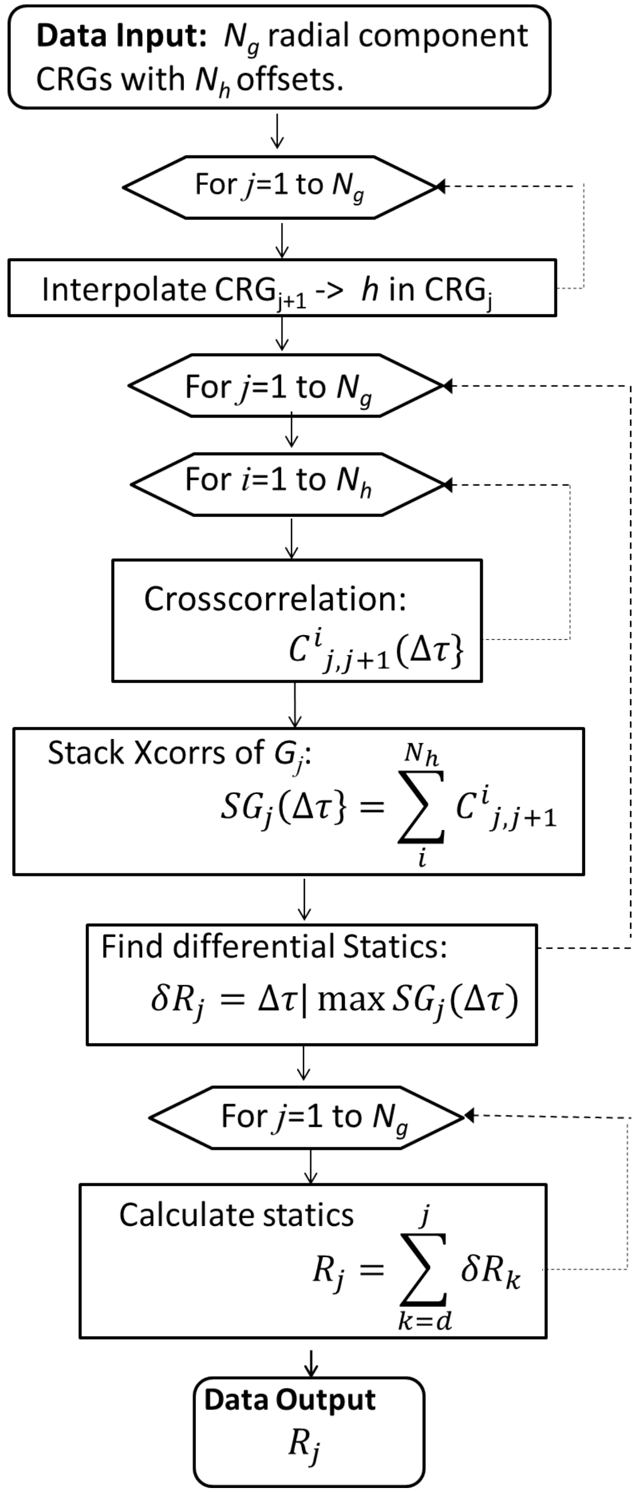

Figure 3.7: Flow diagram of the method developed for a PS receiver statics correction.

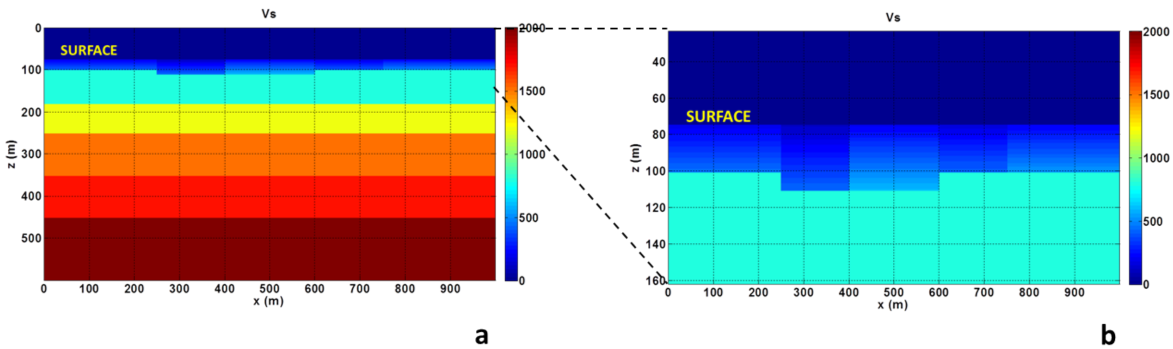

Figure 3.8: S-wave velocity model to test the PS receiver statics algorithm. x-coordinate increases to the right and z-coordinates to the bottom, starting 75 m over the free surface. Sources and receivers are located at the free surface. (a) Layer distribution: beneath the free surface it is the NSL, and below it, five more consolidated rock layers with flat interfaces. (b) Closeup of the NS Layer. Notice the gradual increase in velocity with depth and the four lateral velocity discontinuities.

layers, each one characterized by a constant velocity, which increases with depth. Receivers are separated by 5 m, and sources spaced by 20 m intervals.

Figure 3.10 shows records of the two components of a shot, as an example of the data obtained. Th shot is located at the surface coordinate x=600m. The vertical component is in Figure 3.10a, and the horizontal radial in Figure 3.10b. The vertical component shows P-waves, and the horizontal component mostly S-waves, as expected. Notice the delay times generated by the NSL in the S-waves (horizontal component, Figure 3.10b), correlated with the lateral variations of the surface locations of the NSL.

Figure 3.11 illustrates seismic traces of the horizontal component gathered by CRG. Figure 3.11a corresponds to the receiver at x-coordinate 599 m, CRG 119, and Figure 3.11b corresponds to the receiver at x-coordinate 604 m, CRG 120, hence adjacent CRGs. The distance between traces is the distance between sources, i. e. 20 m, and the number of traces is the number of sources, i. e. 41. A dashed line, corresponding to a velocity of 300 m/s, marks the limit of the high energy low velocity events, considered mostly surface (Rayleigh) waves.

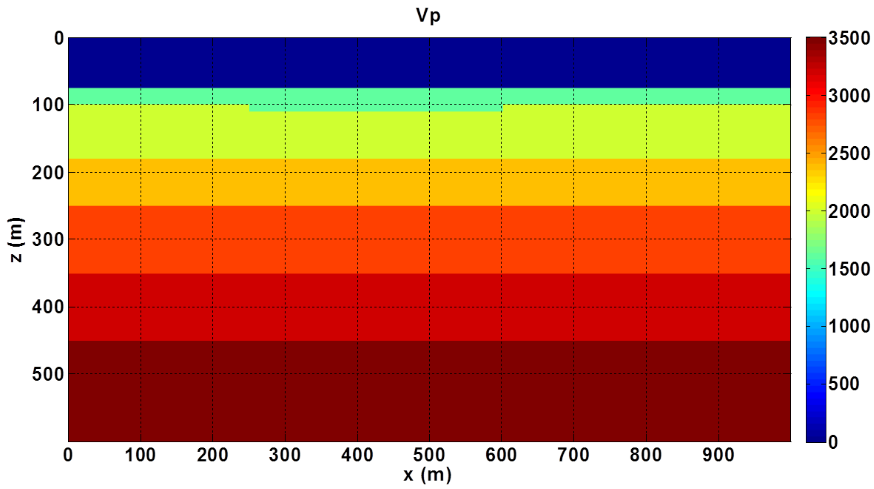

Figure 3.9: P-wave velocity model for testing the PS receiver statics algorithm. The free surface is at a depth of 75 m, below which there is a LVL and five more consolidated rock layers with flat interfaces. The NSL velocity is constant and close to the underlying layer velocity.

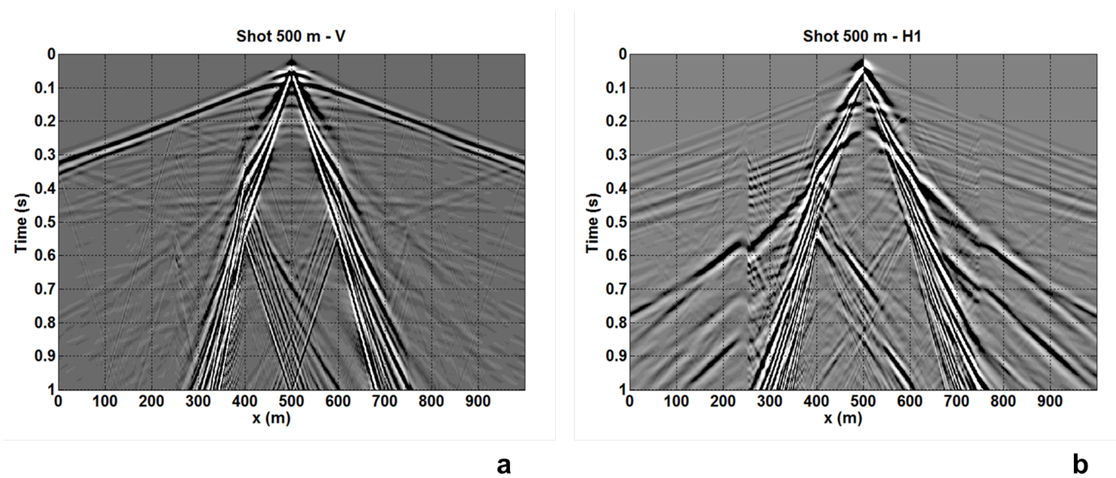

Figure 3.10: Shot gathers for vertical and horizontal components of the synthetic data test for the PS receiver statics method. (a) Vertical component, (b) Horizontal component. Notice the weak first arrivals in (b), and the strong events that resemble the horizontal NSL S-wave velocity variation. It includes PS reflections and probably S wave refractions.

Receiver location, (m)	V_S, (m/s)	Time, (s)	Time differential, (s)
245	325	0.089	
255	277.5	0.126	0.037
395	277.5	0.126	
405	407.5	0.086	-0.040
595	307.5	0.086	
605	300	0.096	0.010
745	300	0.096	
755	325	0.090	-0.006

Table 3.1: Time delay differentials (Column 4) calculated from the synthetic model of the near surface at locations where the NSL changes properties, using the average velocity (Column 2), down to 35 m depth.

Theoretical differential delay times were calculated from an average velocity for each horizontal variation of the NS-LVL, and assuming a thickness of 35 m. These values are in Table 3.1.

3.5.1 Compensation of the Move-Out effect using interpolation

In this dataset the sources are at the same locations than receiver, with distances four times the distance between receivers. Thus, the method requires interpolating the CRG traces to obtain all the intermediate values, as if there were a source at each receiver location. Figure 3.12 illustrates CRG interpolation, obtained from the CRG of Figure 3.11b. Figure 3.12a shows all the traces after interpolation, and Figure 3.12b shows the selected traces, that correspond to the offsets of the adjacent CRG toward lower x-value (in Figure 3.11a).

Figure 3.13 shows the cross-correlation of traces for the CRG in Figure 3.11a and 3.12b. As a side effect, the short offsets appear altered by the interpolation process (compare with Figure 3.20, cross-correlation without interpolation). The time delay is calculated in both directions, left to right and right to left for all the CRGs. The summations (stacks) of the cross-correlation left-to-right (from lower to higher x) for all CRGs are shown in Figure 3.14, and Figure 3.15 shows the analogous result when the analysis is carried out right to left (from

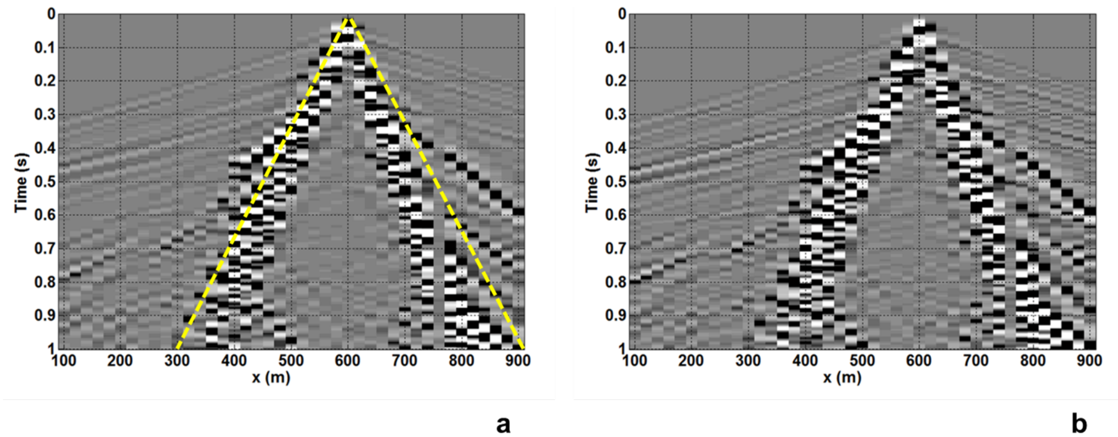

Figure 3.11: Common receiver gathers for adjacent receivers about x=600 m of the synthetic data test for the PS receiver statics method. (a) CRG at x=599 m, (b) CRG at x=604 m. Similar events can be seen on both gathers. The dashed line in (a) indicates a velocity limit assumed for surface waves.

higher to lower x). Notice that the cross-correlation variations correspond to the locations of the lateral changes in velocity (Figure 3.8), verifying the hypothesis behind the method. Also notice that the signs of these anomalies are opposite between forward and backward calculations, which is expected, since the residual delay sign depends on the direction.

The maximum values of both cross-correlation analyses are presented in Figure 3.16. The blue continuous line with dots refers to the forward calculation, and the red dashed line with stars refers to the backward calculation. It shows the opposite polarity for each method at the NSL V_S variation locations. A delay of 2 ms for all the CRGs in both methods can be seen. This delay may be explained as a phase effect of the interpolation using the $\tau - p$ transform. It suggests a method to overcome this delay, by subtracting the backward calculation from the forward and halving the result. Thus the value of zero is obtained, removing this trend.

In addition, there are some outliers without physical meaning, which can also be subject of attenuation. A mask to choose the picks, and a threshold to edit very low values, (assuming that a delay smaller than 4 ms is not reliable), can be used to edit these anomalies. The result

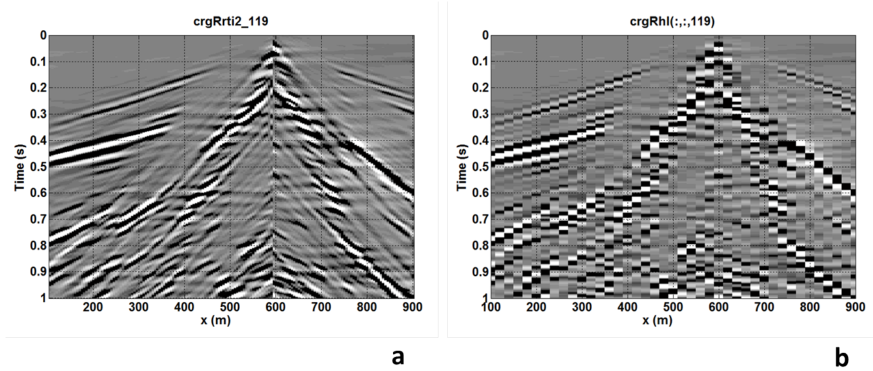

Figure 3.12: Interpolation of the CRG of Figure 3.11b, x=604, from the acquisition offsets to the offsets of the adjacent CRG, x=599. (a) First step is the interpolation from the distance between sources (20 m) to the distance between receivers (5 m), (b) Second step is selecting only the offsets of the adjacent CRG (Figure 3.11a).

of these operations is displayed in Figure 3.17. These values correspond to the differential receiver statics δR. The statics correction is obtained from them, summing through the CRG locations in the forward direction (equation 3.14). The resulting statics are shown in Figure 3.18, corresponding to the blue line. The theoretical statics calculated from data of table 3.1 are represented by the red dashed line as for comparison.

Finally, Figure 3.19 shows the shot gather corresponding to the location x=900 m, before statics application in Figure 3.19a, and after statics application in Figure 3.19b. Notice improvement in the continuity of the events, e.g. at offsets between -500 and -650 m.

3.5.2 Cross-correlation analysis without interpolation

This test shows the issue generated by the offset delay δN_{ijk}. The horizontal component CRGs of Figure 3.11, without interpolation, illustrate the input data used. In this analysis the traces of the same shot are assumed analogous, therefore cross-correlated. Figure 3.20 shows the results of cross-correlation for the analogous traces of CRGs 119 and 120 (CRGs at x 599 and 604 m in Figure 3.11). The scale corresponds to the normalized cross-correlation. Shot statics are already corrected. Note the horizontal variation, with a difference between

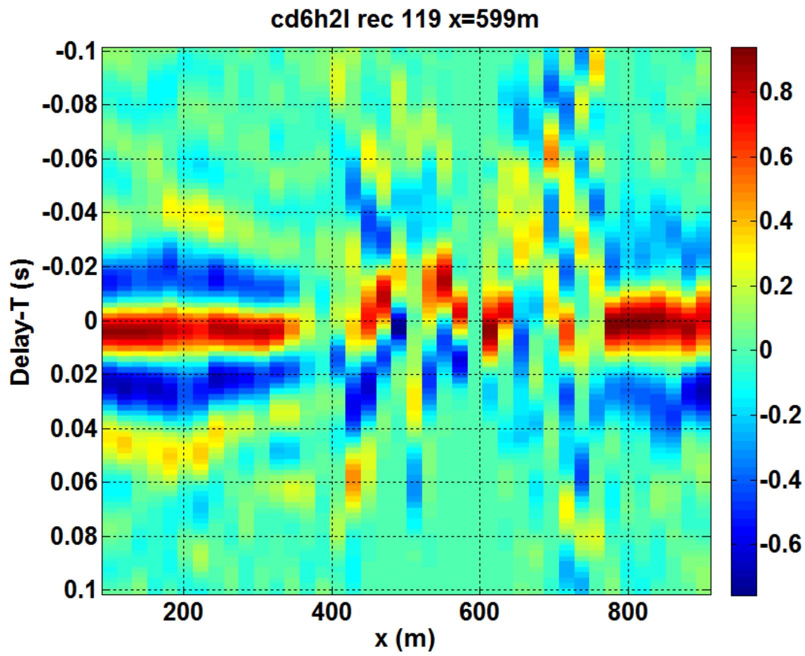

Figure 3.13: Crosscorrelation of CRGs at x=599. The cross-correlation at short offsets, between x 400 and 750, is poor (compare with Figure 3.20). However is good for higher offsets.

positive and negative offsets, which can be attributed to the NMO time delay component of equation 3.4, as analyzed in section 3.4.5. Figure 3.21 shows the stacked cross-correlation for each receiver gather of the synthetic line, left to right. Note that the same trend is exhibited, since the left hand side shows negative values and the right hand side positive, when zero (or at least no difference) would be expected.

3.6 Application to Real data: Spring Coulee, Alberta

The method was tested on the experimental 2D 3C 2008 Spring Coulee seismic survey, acquired in Alberta, Canada, by the CREWES project with the support of sponsor companies. Details have been published in CREWES project reports and technical meetings (e.g Lu and Hall, 2008; Isaac and Margrave, 2011). The seismic data selected for testing the method are from a 6500 m long seismic line, composed of 652 3C sensors separated 10 m from each

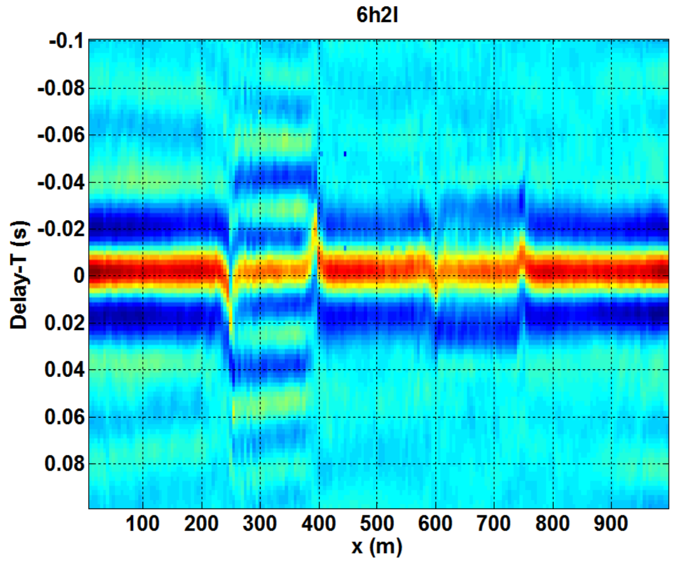

Figure 3.14: Summation of pairwise cross-correlations of adjacent CRGs from left to right. Each trace of a CRG is crosscorrelated to the corresponding offset trace after interpolation of the adjacent CRG tto the right (larger x coordinate).

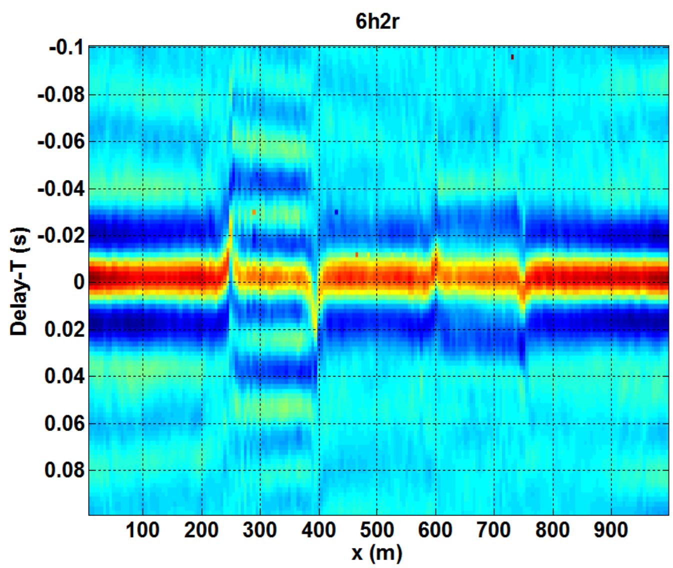

Figure 3.15: Summation of pairwise cross-correlations of adjacent CRGs from right to left. Each trace of a CRG is crosscorrelated to the corresponding offset trace after interpolation of the adjacent CRG to the left (smaller x coordinate).

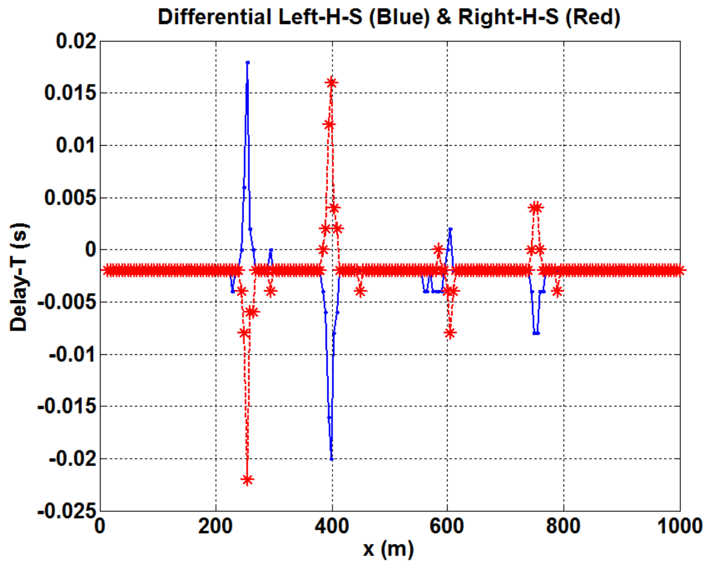

Figure 3.16: Picking of the maximum CRG cross-correlations in both directions. The dashed red line with asteriks corresponds to the right-hand-side cross-correlation, and the blue continous line with dots to the left-hand-side cross-correlation. Both have opposite polarity at the lateral NS V_S variations and a common constant delay of 2 ms.

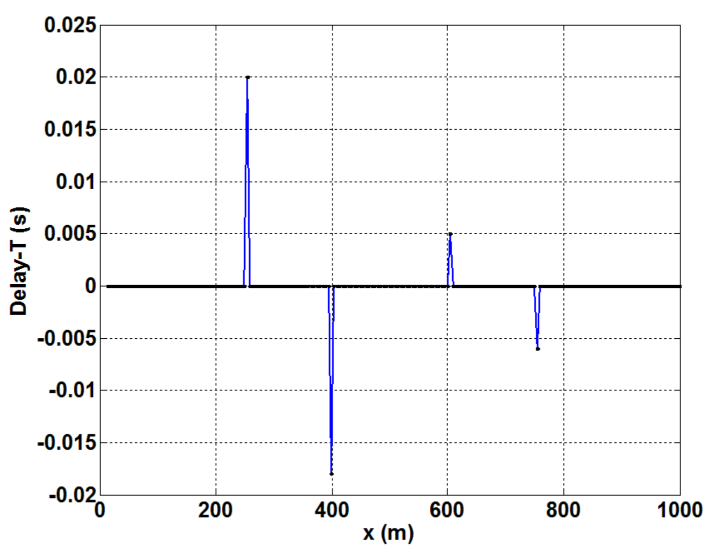

Figure 3.17: Summation of the maximum CRG cross-correlations in both directions. The right-hand-side cross-correlation maximum was substracted from the maximum left-hand–side and the result divided by two. It can be noticed that the 2 ms constant delay was eliminated.

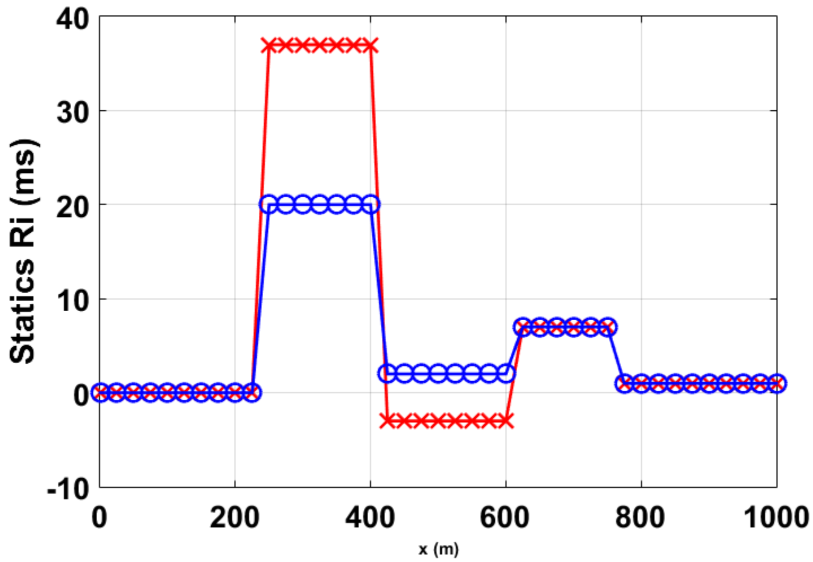

Figure 3.18: Statics calculation after interpolation (blue line, circles), obtained by summation on the x direction, compared with theoretical (red line, crosses).

other, and with 192 energy sources separated nominally at 30 m.

3.6.1 Receiver statics calculation

Firstly the seismic traces are organized into CRG and interpolated. As an example, Figure 3.22 shows two CRGs for left to right cross-correlation. Figure 3.22a corresponds to the CRG 201 and Figure 3.22b to the CRG 202 interpolated).

Figure 3.23 shows the resulting cross-correlations of the traces between CRGs 201 and 202, left to right in (a) and right to left in (b). Notice that they have consistent delays, but with opposite signs, as expected. Additionally, a bias of about -2 ms can be identified. Notice that there are picks with value of about 0.8, which indicates good quality, since the maximum possible is 1.0.

The variation of the differential receiver statics along the line is illustrated by Figure 3.24. Figure 3.24a compares the stacks of the cross-correlations in CRGs 200, 201 and 202. Notice a variation range of about 5 ms between them. Figure 3.24b shows the cross-correlation

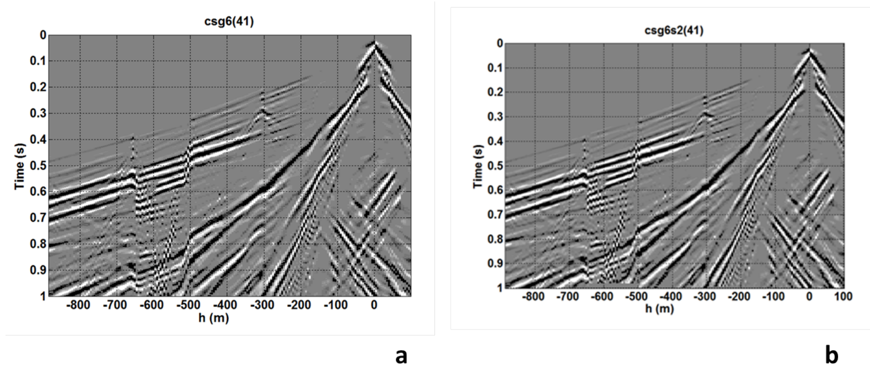

Figure 3.19: (a) Raw CSG without statics, and (b) after statics applied.

stacks for all the CRGs, with the approximated location of the traces represented in Figure 3.24a, indicated by an arrow. Figure 3.25 shows the values of the maximum peaks in Figure 3.24b. Notice that some peaks could be neglected since they have a very low value, therefore low reliability.

Figure 3.26 shows the picks of the largest amplitude of the cross-correlation stacks for analysis in the left to right direction (Figure 3.26a) and in the right to left direction (Figure 3.26b). Notice that they are alike with opposite sign, as expected, and both have a bias of about -2 ms. There are also a number of outliers, with values larger than 20 ms.

The processing includes first editing the outliers from Figure 3.26. After that, a subtraction between the maximum picks of the cross-correlations in both directions, allows us to edit the 2 ms bias. Figure 3.27 shows the resulting differential receiver statics δR for all the CRGs. Finally, the receiver statics are obtained from the summation with respect to a location selected as the datum.

The resulting receiver statics correction is shown in Figure 3.28, labeled *New-CRGS*, which is compared with the result of the CRSS method. Notice that differ in details, however both follow the same trend.

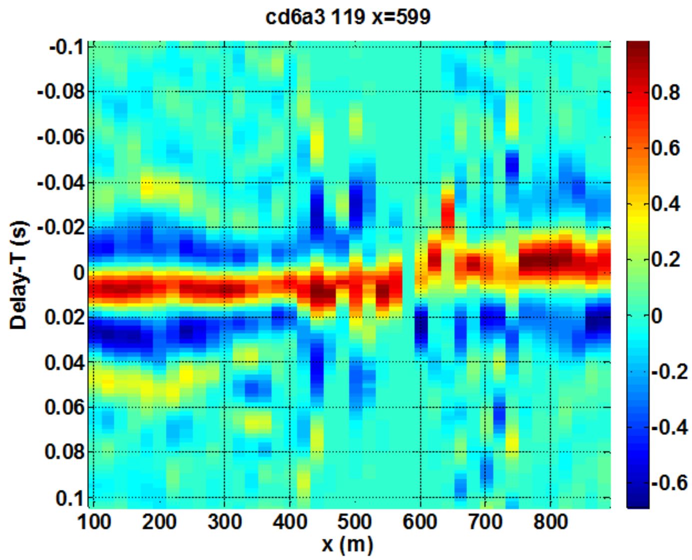

Figure 3.20: Results of cross-correlation of common receiver gathers for adjacent receivers about x=600 m, without interpolation. Notice a difference in time delay between positive offsets (lesser than 600 m) and negative offsets (greater than 600 m). See the explanation of section 3.4.3 and 3.4.5, and compare with Fig. 3.13.

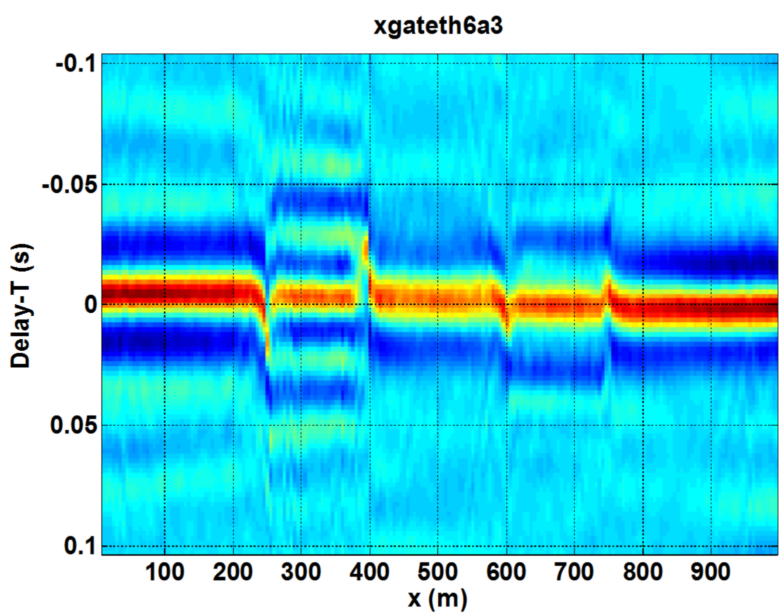

Figure 3.21: Result of the summations of cross-correlations for each CRG, without interpolation. Notice the trend along the locations, negative to the left and positive to the right (compare with Fig. 3.14).

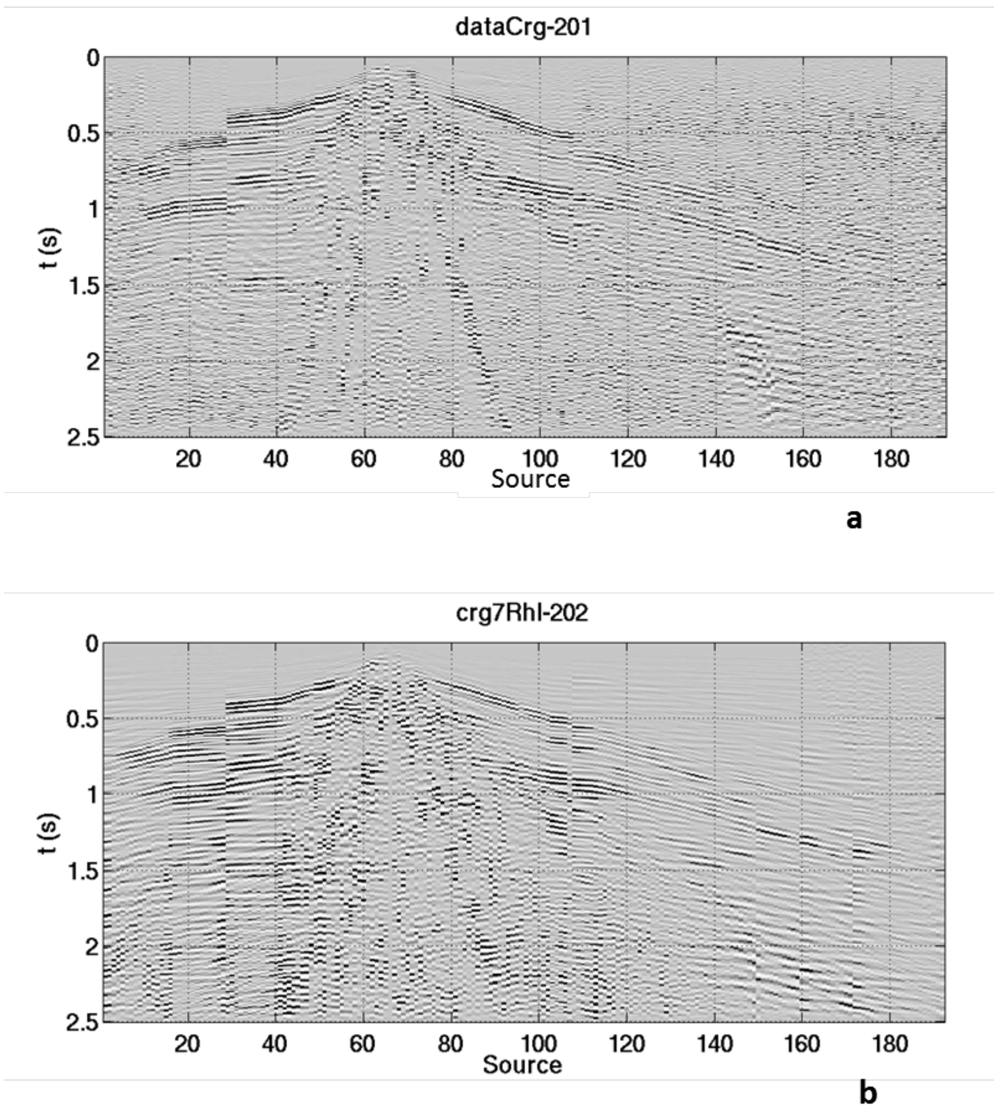

Figure 3.22: Spring Coulee 2D-3C line: data prepared for the cross-correlation of CRG 201 to the left hand side. (a) CRG 201 (b) CRG 202 interpolated, (same offsets as in CRG 201).

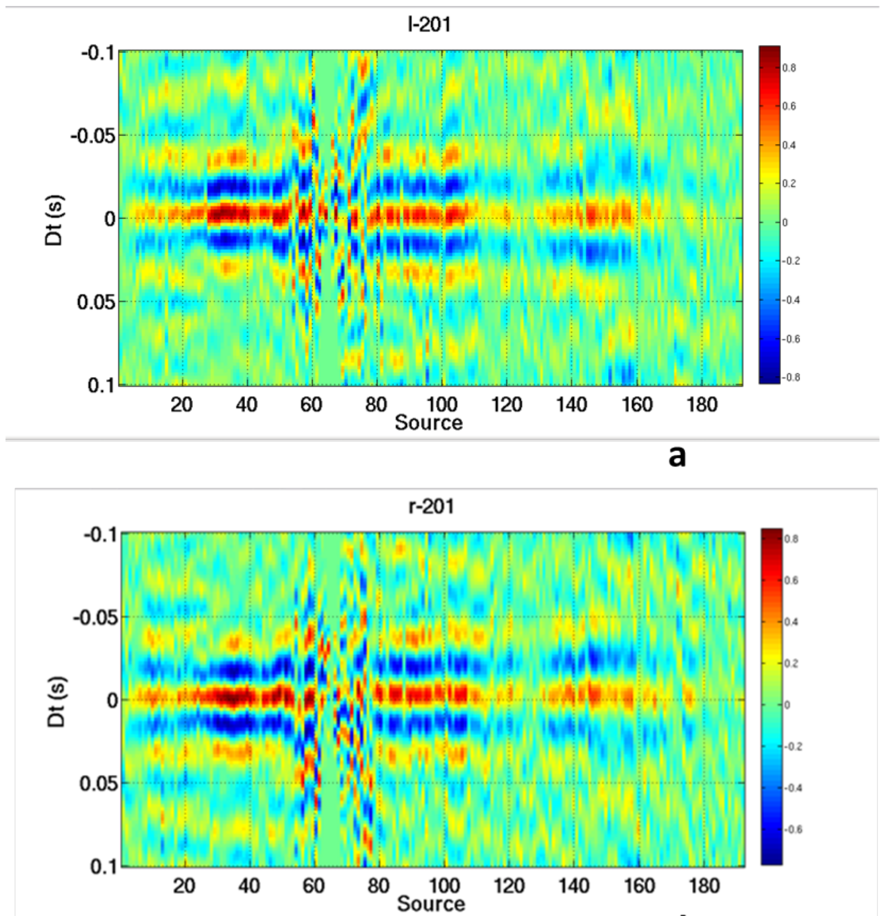

Figure 3.23: Spring Coulee 2D-3C line: cross-correlation of the traces in CRG 201 (a) Left to right direction. (b) Right to left direction. Notice the opposite polarity of the deviations of the correlation maxima between these two directions.

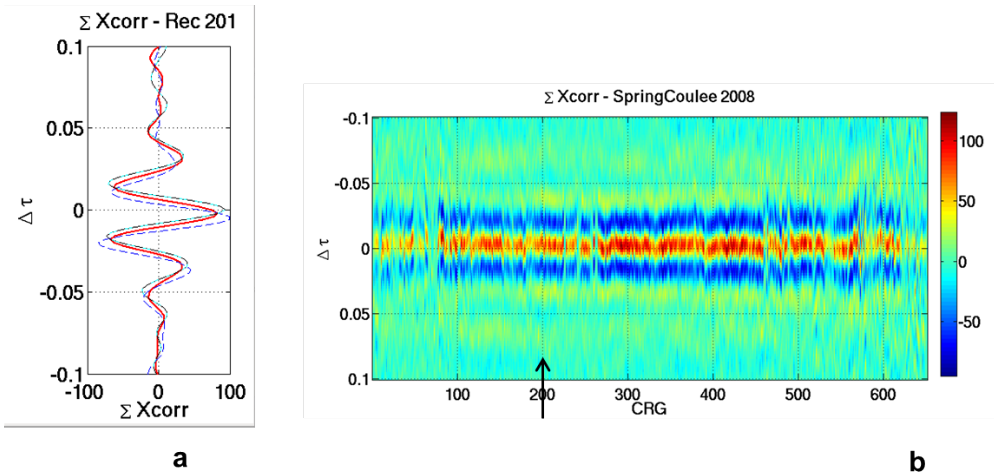

Figure 3.24: Crosscorrelation stacks in the direction left to right for all receivers. (a) Individual stacks for CRGs 200 (blue dashed line), 201 (solid red) and 202 (black dash dotted). (b) Stacks for each one of the CRGs; the location of the traces selected in Figure (a) is shown by an arrow.

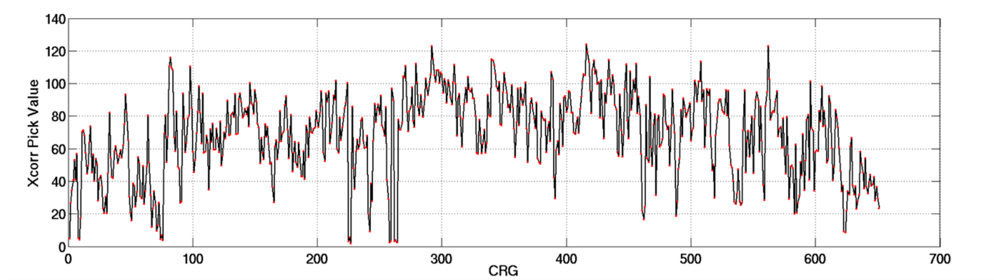

Figure 3.25: Maximum picks on the cross-correlation stacks (Figure 3.24). The maximum (perfect) possible value corresponds to the fold, i.e. 192, just in case that all the analogous traces were exactly equal. This figure gives a measurement of the cross-correlation reliability.

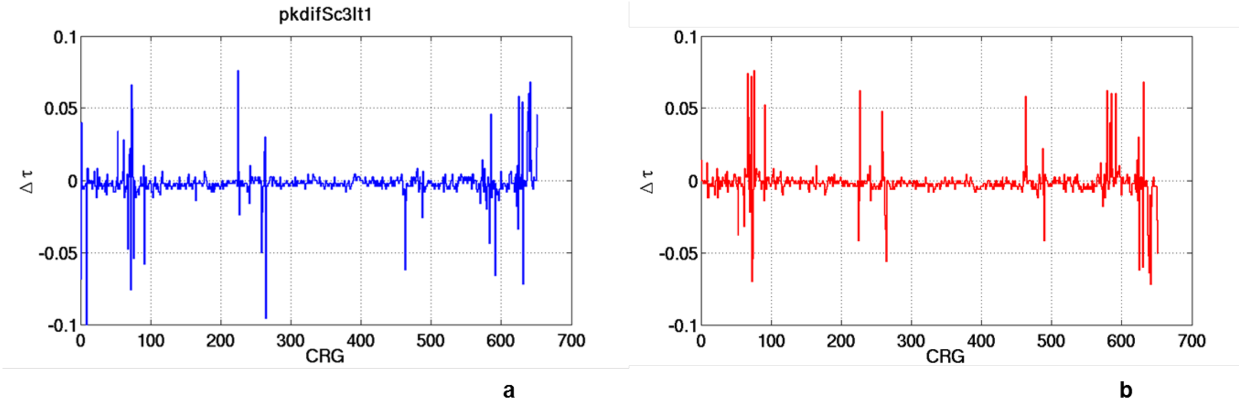

Figure 3.26: Time delay of the maximum picks on the cross-correlation stacks for both directions. (a) Left to right. (b) Right to left. Notice that Figure (a) is approximately opposite in $\Delta\tau$ to Figure (b) but with a bias of about 2 ms. A number of outliers, (large values, exceeding 0.02 s) can also be identified.

3.6.2 Real data processing

The result of our new CRGS method was compared to elevation statics, and to the result of the CRSS method applying processing until stack sections. Basic processing (according to Figure 1.5b) included noise filtering to attenuate ground-roll and other coherent events, and spikes (random high amplitude noise) editing. Source statics obtained from the PP-wave processing were applied.

The converted wave stack was obtained using asymptotic binning assuming a V_P/V_S ratio of γ=1.9. The converted wave stacking velocity, V_C, is preliminary, obtained from the PP-stacking velocity V_P (resulting of the P-wave processing) according to the approximate equation

$$V_C = \sqrt{\frac{V_P^2}{\gamma}} \tag{3.15}$$

3.6.3 Statics application

Figure 3.29 shows the effect of the statics correction calculated with the CRGS method in the stacked section (Figure 3.29b), compared with a stack section with elevation statics

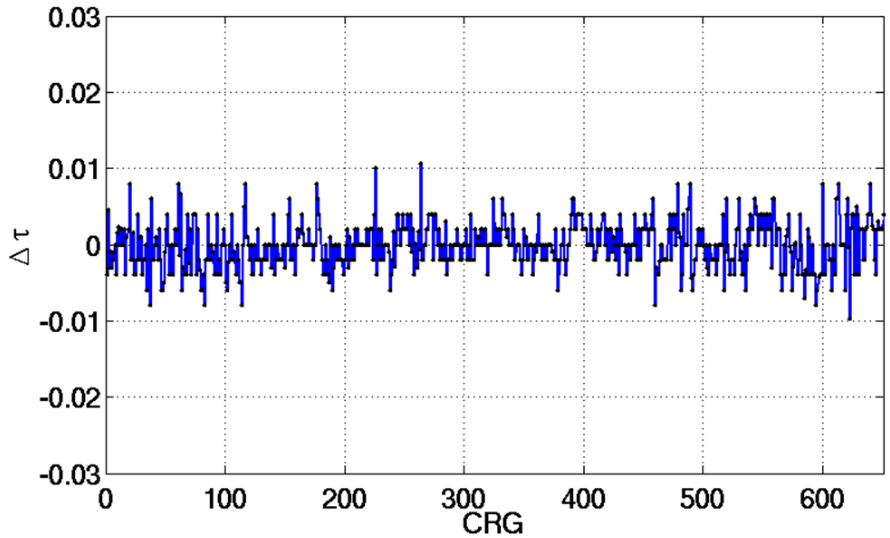

Figure 3.27: Differential receiver statics after bias correction and edition of outliers. For the bias correction the results of Figure 3.26 are subtracted and the result divided by two.

applied to the receiver (Figure 3.29a), where constant velocity and thickness were assumed for the near-surface layer. Notice that there is more continuity of the events in Figure 3.29b, indicating that a meaningful receiver statics outcome has been obtained.

Figure 3.30 shows a stack section following the same processing but applying the final CRSS receiver statics (Figure 3.28). The resulting image shows remarkable consistency, which supports the quality of the CRSS solution, that can be considered among the best possible in the industry (Isaac and Margrave, 2011). The CRGS solution, even not as excellent, provides a comparable image, confirming the promise of this method.

3.6.4 Effect on the velocity analysis

Figure 3.31 shows typical displays of the velocity analysis without (Figure 3.31a) and with the CRGS method (Figure (3.31b). The semblances (left hand side panels) show better continuity and stronger picks in (b), allowing easier picking of the stacking velocities, which illustrates a potential benefit of the new statics correction method (for a better understanding of this Figure, see Yilmaz (2001)).

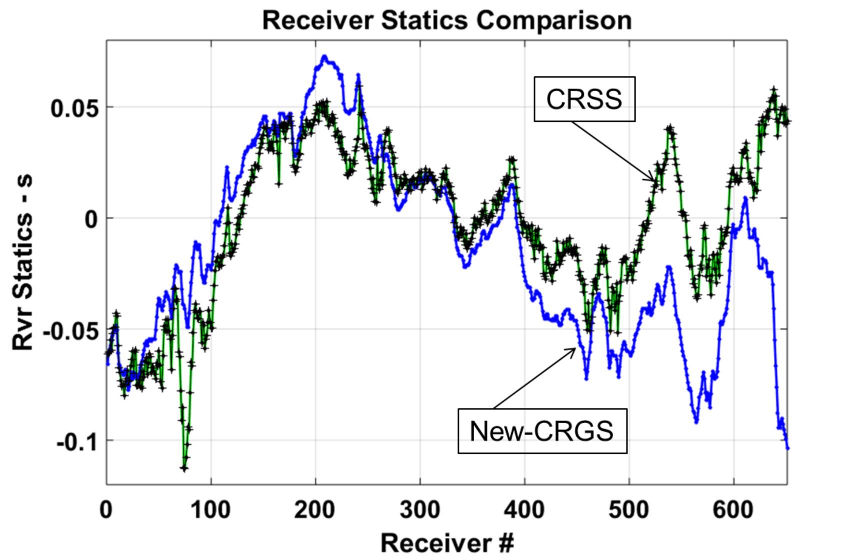

Figure 3.28: Comparing receiver statics delay using the CRSS method and the new CRGS method.

3.7 Discussion

The methods to obtain the NSL S-wave velocity are still not good enough, therefore can not solve the high resolution receiver statics required for PS-data. On the other hand, it can be obtained with the CRS method.

The CRSS method and the CRGS proposed share the same basic principles. The main difference is that CRSS obtains the result from stacked data and CRGS does not. CRSS requires V_C, and a PS-wave horizon guide to stack. However the stacking can probably destroy other PS events because the velocity model error.

In contrast the CRGS method does not require identification of any event, but uses all the events on each trace, even if they are not visible, and all the traces of adjacent CRG, just assuming that all of them have the same receiver statics. However it carries the lacks of the statics correction assumption, i. e. vertical incidence surface cosnsitent, caused by a low velocity NSL, which not always is valid.

Cox (1998) refers four possible sources of error in the statics correction: moveout effect,

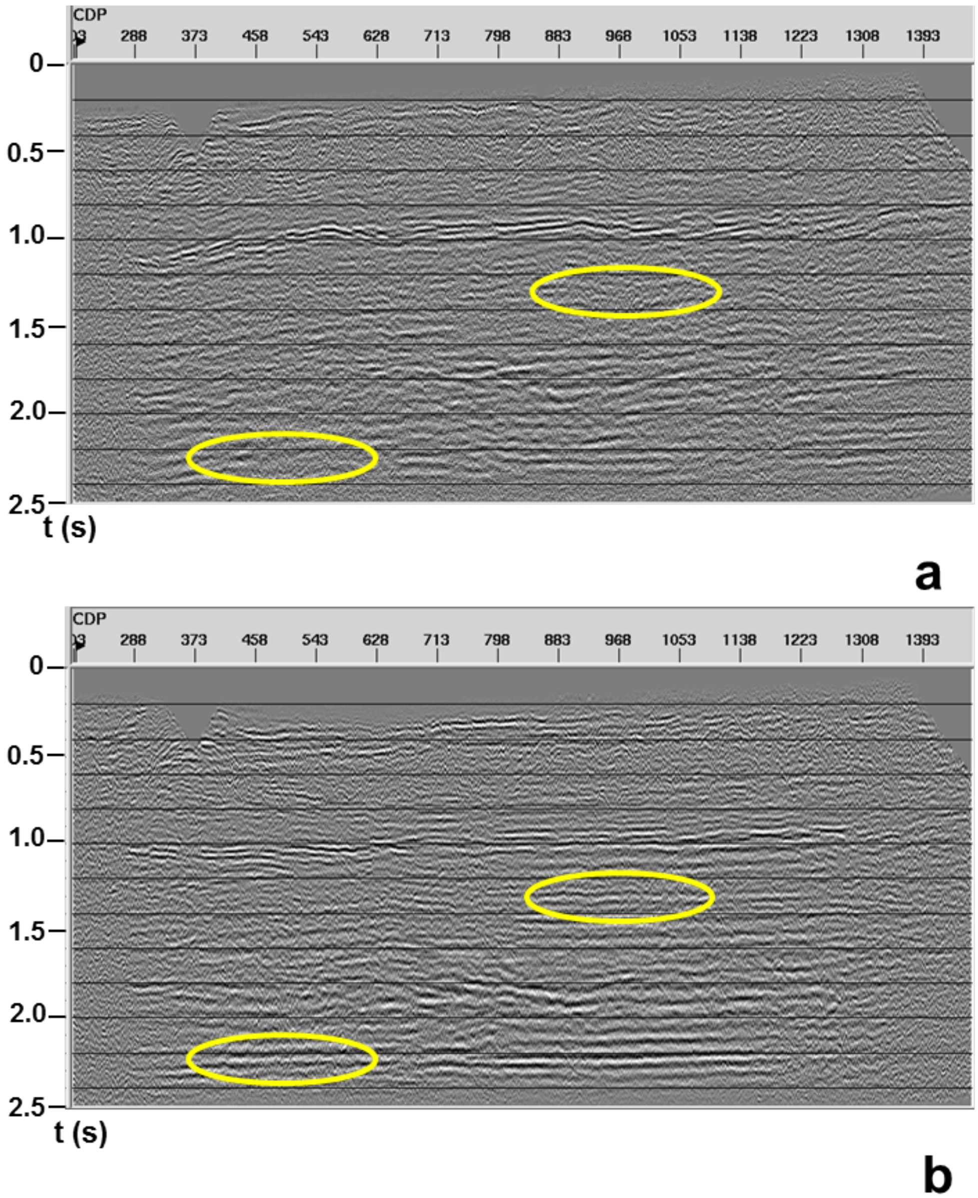

Figure 3.29: Effect of the statics correction in stack sections. (a) Stack section using elevation statics. (b) Stack section using the CRGS receiver statics. Notice the improved continuity in (b), illustrated by the ovals.

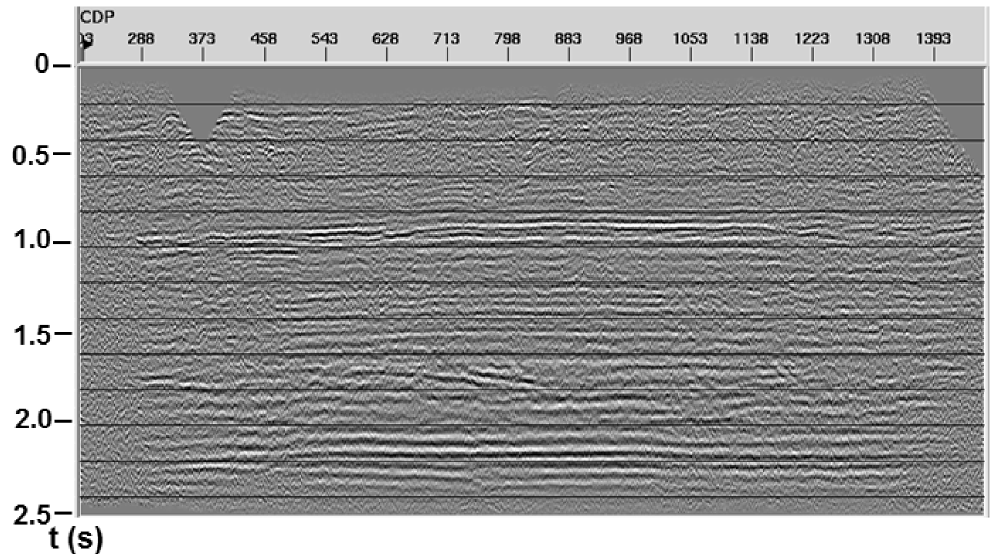

Figure 3.30: Stack section using receiver statics obtained with the CRSS method.

geologic structure or dip, possible cycle skipping in picking, and remaining noise contamination. Their presence in the method proposed is addressed as follows:

1. Moveout effect is compensated by trace interpolation.

2. Geologic structure or dip is possibly minor, and attenuated by the cross-correlation stack effect.

3. Possible cycle skipping in picking perhaps is a minor problem since the highest cross-correlation includes many events as possible of the two traces.

4. Remaining noise contamination, perhaps attenuated by cross-correlations stack, however noise maybe explicitly considered in future analyses.

Tables 3.2 and 3.3 show comparisons with other methods for statics correction, thus summarizing the strengths of the proposed method.

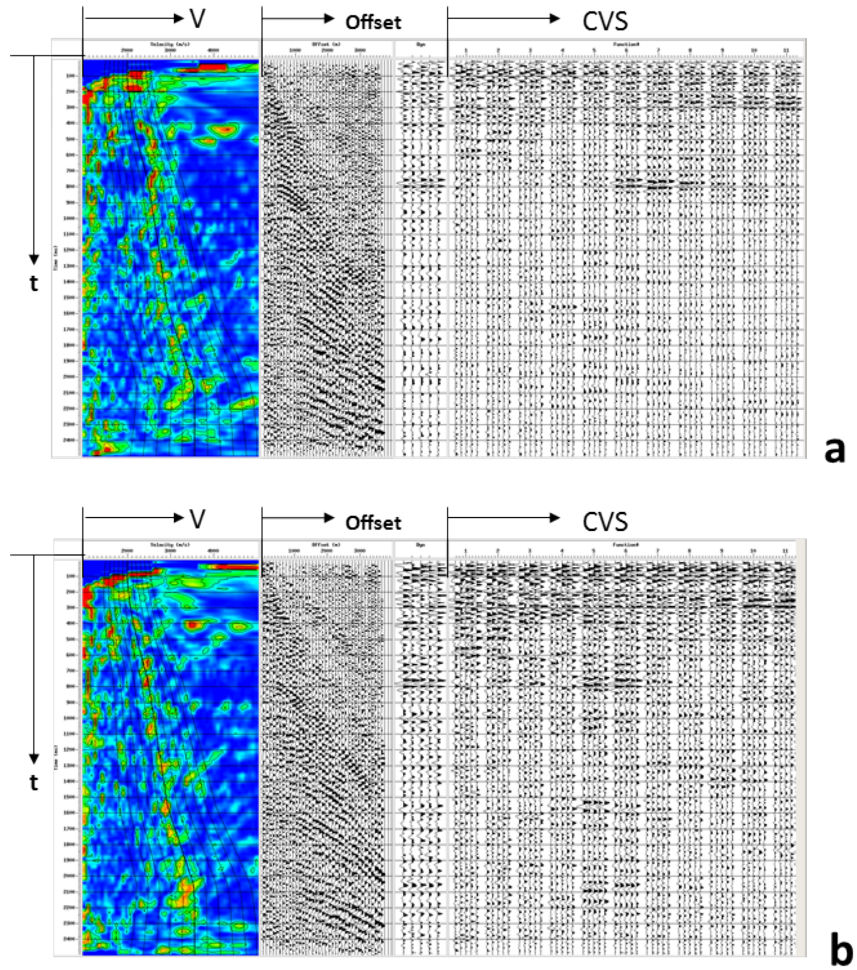

Figure 3.31: Comparison of the receiver statics effect on Velocity analysis of a CDP. (a) Without the receiver statics correction. (b) With the CRGS receiver statics correction: the events are easier to follow. (V is the stacking velocity, CVS means constant velocity stack, and t time.)

Datum statics using a NS S-wave velocity model	**New method**
Low frequency statics solution.	High frequency statics solution
Reliable NSL S-wave velocity can be hard to obtain.	Does not require NSL S-wave velocity.

Table 3.2: Comparison of the PS-wave receiver correction method proposed, CRGS, with the datum statics method.

Receiver statics using Common Receiver Stacks	**New method**
Requires a PS-wave stacking velocity, V_C.	Does not require V_C
Requires a guide horizon.	Does not require a guide horizon.
Works better in flat geology.	Does not assume flat geology.
It is laborious.	It is automatic.

Table 3.3: Comparison of the PS-wave receiver statics method proposed with the method CRS (section 3.3.2).

3.8 Conclusions

1. A method for the receiver statics correction of PS seismic data is being proposed here. It works in the CRG domain, without requiring stacking of PS events. The receiver statics are obtained from the cross-correlation of corresponding traces of adjacent CRGs

2. The method proposed can provide the short wavelength solution, since is based in differential delay times which are independent to each other.

3. An effective correction of the delay caused by the NMO step is proposed, using interpolation to obtain the same offset in the traces to cross-correlate.

4. A test of the converted wave CRGS method on real data has been presented. The new method improves the continuity of events on a stack section compared with an application of simple elevation statics. A stack with final receiver statics correction using the CRSS method appears more continuous than the stack section using the CRGS method.

5. Picking of maxima of the cross-correlation stacks may include outliers. Editing them would be convenient. On the other hand, application of methods specifically created for interpolation could benefit the result.

6. The new method does not require stacking velocity V_C, a guide horizon, or a

flat reflector, which are required by the CRSS method, neither a near surface layer S-wave velocity, as datum statics, and is automatic, so it is less laborious than other methods.

7. Semblance plots for velocity analysis show better continuity after application of the CRGS method. This allows easier picking of velocities, a potential benefit of the method.

Chapter 4

Mode separation for elastic waves recorded on a sloped surface

4.1 Introduction

Robust scalar methods, which have proven successful in P-wave processing, are commonly applied to multicomponent data, i.e. PP and PS-waves. This technology requires that the input data be composed only of one wave-mode, P or S. Thus, it is usually assumed that the vertical component corresponds to P-waves, and the horizontal one to S-waves, which is a reasonable assumption since seismic waves arrive almost normal to the surface due to the low velocity NSL. Otherwise, both wave-modes can be expected in horizontal and vertical components. In fact, the previous assumption can be considered inaccurate, even more so in the case of a high velocity NSL, or for long offsets.

Wave mode separation is more suitable in principle, especially if an analysis of true amplitudes is intended. Wave mode separation has been proposed as a first step in analyzing multicomponent data (e.g. Wapenaar et al., 1990). A number of potential advantages have been identified for wave-mode separation of multicomponent data, such as noise attenuation, easier processing and interpretation (see e.g. Van der Baan, 2006). In addition, elastic migration methods require mode separation (e.g. Wang and McMechan, 2015).

On the other hand, the seismic event recorded at the free surface results of the interaction between the incident wave, propagated through the body of the medium, and the energy reflected at the free surface, due to the contrast between the solid medium and the free air. This property is known as the *free surface effect*. A method for wave-mode separation taking into account the free surface effect, was proposed by Dankbaar (1985) and extended by Donati and Stewart (1995) to marine data.

In addition, the NSL in complex areas can show more variable features, such as near surface high velocity in rocky outcrops, rough topography, and heterogeneity over short distances, both in thickness and velocity, which may have an effect on reflections from depth interfaces, generating uncertainty in the angle of incidence to the surface. Moreover, in an inclined surface with a low velocity NSL, normal incidence to the surface means an angle with the vertical and horizontal directions of the sensor components, therefore both sensors would record both wave modes, as illustrated in Figure 4.1 (see e.g. Guevara et al., 2007).

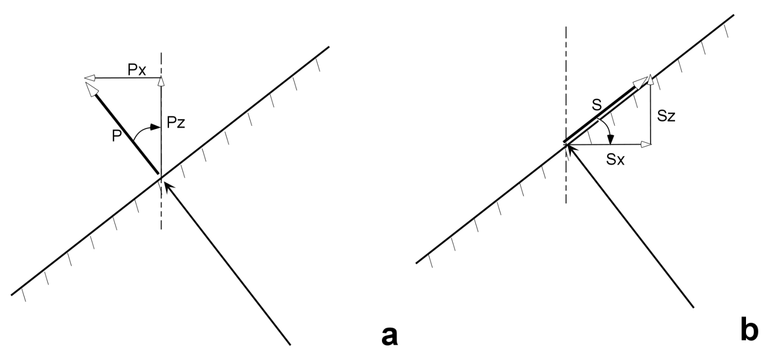

Figure 4.1: Normal incidence to an inclined surface for (a) P-wave and (b) S-wave.

In this chapter I investigate wave mode separation applied to complex land areas taking into account the free surface effect. Two properties of the near surface are taken into account: topography and lateral heterogeneity. It is assumed that the surface has a slope, and that its elastic properties can change from location to location. The method is tested and analyzed using synthetic data.

4.2 The free-surface effect

Data recorded on the land surface is the result of the interaction between the arriving reflection and the free-surface. i.e. is the summation of the incident and reflected waves. This property is known as the *free-surface effect.* Reflections and wave mode conversions are generated at the free surface, hence the free-surface effect depends on the angle of incidence and the elastic properties of the near-surface (e.g. Meissner, 1965; Evans, 1984).

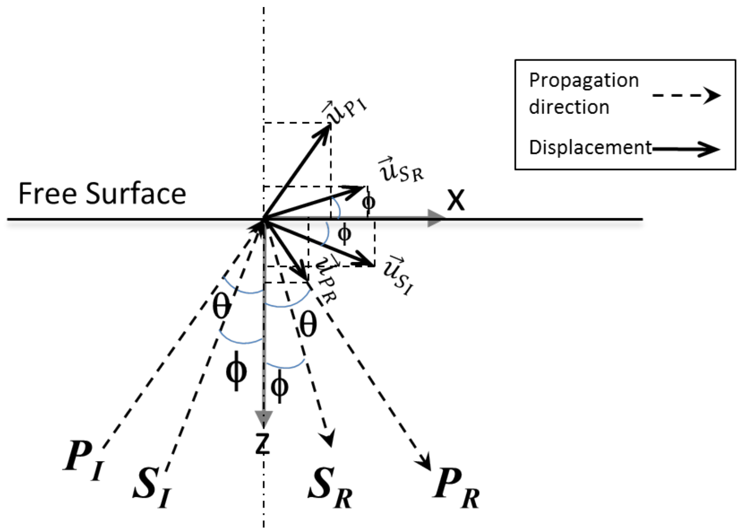

Figure 4.2: Free-surface effect: decomposition of P and S waves arriving to the surface, for incident P-wave (P_I), and S wave (S_I). Coordinate axes are x increasing to the right and z increasing downward. P_R identifies the reflected P-wave, and S_R the reflected S-wave. The displacements are identified by the vector $\vec{u}$, with an index of each type of wave.

Figure 4.2 illustrates the relationship between incident P-wave and S-wave and the corresponding reflections at the free surface. From these relations, the displacements in the vertical (z) and horizontal (x) directions can be found as a function of the angles of incidence and the velocities of the media. An outline of this derivation follows, and the details are in Appendix C):

1. At the free surface there are no normal or shear stresses, to pose the stress equilibrium equations.

2. Assuming an incident monochromatic plane wave, it is possible to obtain an expression for the displacements as a function of the elastic properties and angle of incidence. The stresses for an isotropic medium are a function of the displacements (equations A.9 and A.10), thus can be expressed as a function

of the angle of incidence and the elastic properties.

3. Provided a unit incident P-wave or S-wave, the relations between amplitudes of incident and reflected events is obtained from the stress equations of the previous point.

4. The displacements in the vertical (z) and horizontal (x) directions are the projections of the amplitudes previously obtained on each coordinate axis.

The relations between an incident plane wave (P or S) and the vertical (z) and horizontal (x) components are obtained as a function of the elastic properties and the angles of incidence. These relations are the *coefficients* represented in the following as R_{φ}^{χ}, where the subscript φ corresponds to the incident wave mode, and the superscript χ corresponds to the direction of the component:

$$R_P^z = \frac{(V_P^2 - 2V_S^2(1-\cos^2\theta))\,(-2\cos\theta(2\cos^2\phi - 1) - 4\,(V_S/V_P)\sin\theta\cos\theta\sin\phi)}{4V_S^2\sin\theta\cos\theta\sin\phi\cos\phi + (2\cos^2\phi - 1)\,(V_P^2 - 2V_S^2(1-\cos^2\theta))} \tag{4.1a}$$

$$R_P^x = \frac{4\sin\theta\cos\theta\sin\phi\,(2V_S^2\sin\theta\sin\phi + (V_S/V_P)\,(V_P^2 + 2V_S^2(1+\cos^2\theta)))}{4V_S^2\sin\theta\cos\theta\sin\phi\cos\phi + (2\cos^2\phi - 1)\,(V_P^2 - 2V_S^2(1-\cos^2\theta))} \tag{4.1b}$$

$$R_S^z = \frac{4V_S^2\cos\phi\sin\phi\cos\theta\,(2\sin\theta\sin\phi + (V_P/V_S)\,(2\cos^2\phi - 1))}{4V_S^2\sin\theta\cos\theta\sin\phi\cos\phi + (2\cos^2\phi - 1)\,(V_P^2 - 2V_S^2(1-\cos^2\theta))} \tag{4.1c}$$

$$R_S^x = \frac{2\cos\phi(2\cos^2\phi - 1)((2V_SV_P\sin\phi\sin\theta) + (V_P^2 - 2V_S^2(1-\cos^2\theta)))}{4V_S^2\sin\theta\cos\theta\sin\phi\cos\phi + (2\cos^2\phi - 1)\,(V_P^2 - 2V_S^2(1-\cos^2\theta))} \tag{4.1d}$$

Figure 4.3 shows an example of the free surface coefficients for P-wave incidence, and Figure 4.4 for S-wave incidence, assuming V_P 2000 m/s and V_S 1000 m/s (the vertical function in (a) and the horizontal in (b)).

4.3 The method for wave mode separation using the free surface effect

The incident wavefield can be decomposed into plane waves (see e.g. Aki and Richards, 1980, Chapter 5), each one with a specific angle of incidence. Thus, each recorded component, vertical and horizontal, can be expressed as the plane incident wave times the corresponding

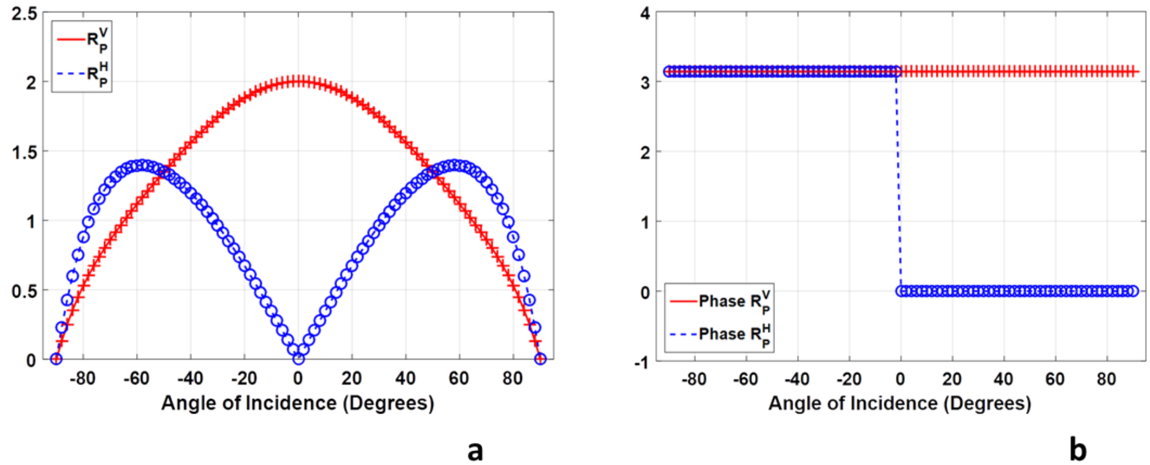

Figure 4.3: Example of the free-surface effect as a function of the angle of incidence for P-wave arrival. V_P 2000 m/s and V_S is 1000 m/s. (a) Amplitude response, (b) Phase response. Red (crosses) and blue (circle)s correspond to the vertical and horizontal components respectively.

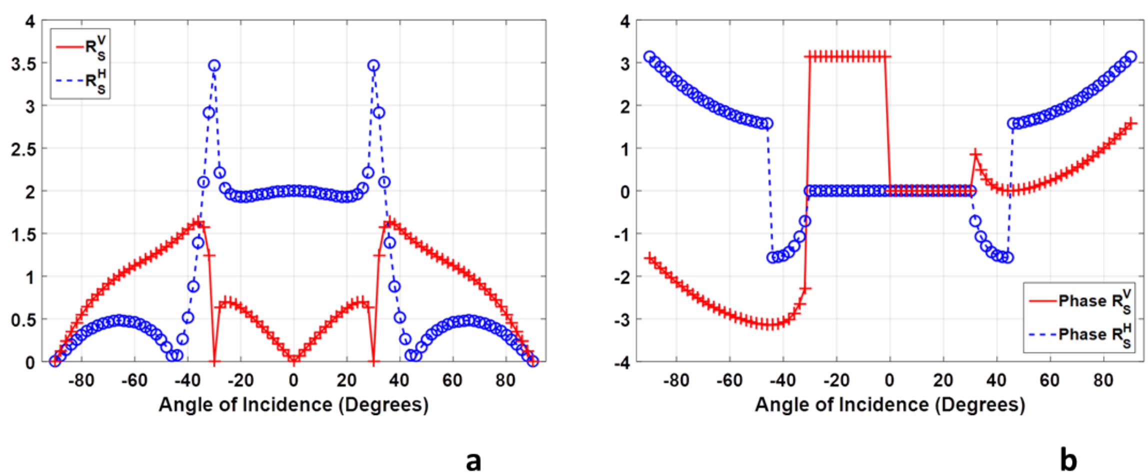

Figure 4.4: Example of the free-surface effect as a function of the angle of incidence for S-wave arrival. V_P 2000 m/s and V_S is 1000 m/s. (a) Amplitude response, (b) Phase response. Red (crosses) and blue (circle)s correspond to the vertical and horizontal components respectively.

free surface effect coefficient, according to equations 4.1. The equations representing the displacement components are

$$u^z = \sum_{\theta=\theta_0}^{\theta_f} (P_I(\theta) R_P^z(\theta, V_P, V_S)) + \sum_{\phi=\phi_0}^{\phi_f} \big(S_I(\phi) R_S^Z(\phi, V_P, V_S)\big) \tag{4.2a}$$

$$u^x = \sum_{\theta=\theta_0}^{\theta_f} (P_I(\theta) R_P^x(\theta, V_P, V_S)) + \sum_{\phi=\phi_0}^{\phi_f} (S_I(\phi) R_S^x(\phi, V_P, V_S)) \quad , \tag{4.2b}$$

where R_φ^χ are the free surface effect coefficients already introduced in equations 4.1.

Therefore, the incident waves can be obtained if the recorded components and the free surface coefficients are known. The method for wave mode separation based on this principle is presented in the following section.

4.3.1 Plane wave decomposition at the free surface

Equations 4.2a and 4.2b require that the wavefield be expressed as a function of the angle of incidence at the surface, which amounts to decomposing the wavefield into plane waves Two methods to carry out the plane wave decomposition are the *Tau-p* transform and the Fourier transform. Figure 4.5 illustrates the physical meaning of the plane wave variables arriving to the surface, for both methods.

Figure 4.5(a) corresponds to p, the variable used in the *Tau-p* transform, which is known as the *horizontal slowness*, defined as

$$p = \frac{\sin\theta}{V} = \frac{\Delta t}{\Delta x}. \tag{4.3}$$

Figure 4.5(b) shows the frequency characteristics of the Fourier transform, corresponding to a monochromatic (single frequency) plane wave component. T is the period, λ is the wavelength, λ_z is the vertical wavelength, and λ_x is the horizontal wavelength. In addition, since

$$k_x = 1/\lambda_x,$$

it can be shown a relation between both representations (see e.g. Claerbout, 1985)

$$\frac{\sin\theta}{V} = \frac{k_x}{\omega} = p \tag{4.4}$$

since

$$VT = \lambda\,, \qquad \sin\theta = \frac{\lambda}{\lambda_x}\,, \text{ and } \quad \frac{k_x}{\omega} = \frac{T}{\lambda_x}\,.$$

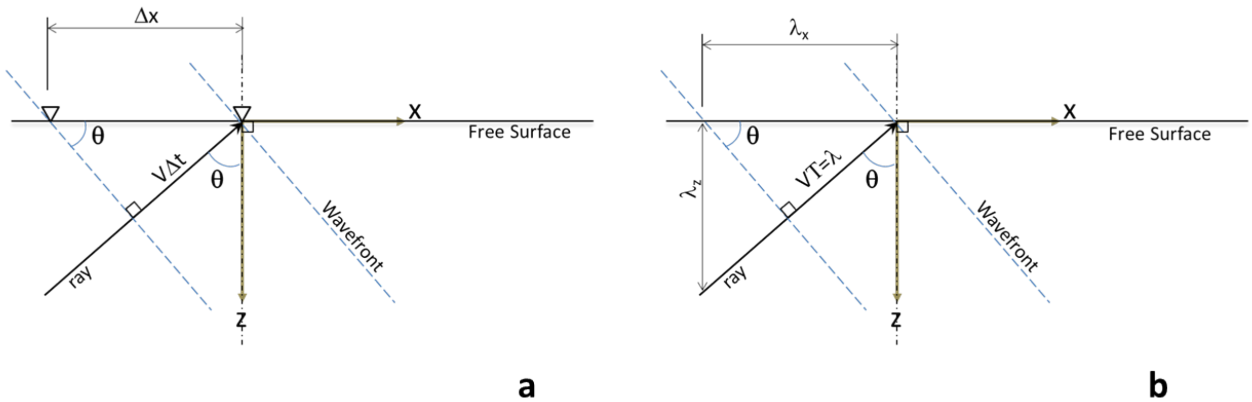

Figure 4.5: Plane wave incidence at the free surface: (a) slowness p relations and (b) frequency domain relations.

4.3.2 Free-surface response equations in the p domain

Equations 4.2a and 4.2b can be represented using p instead of the angle of incidence θ, taking into account the relation between angle of incidence and slowness in Equation 4.3, as follows,

$$u^z(p) = \sum_{p_0}^{p_f} P_I(p) R_P^z(p, V_P, V_S) + S_I(p) R_S^z(p, V_P, V_S) \tag{4.5a}$$

$$u^x(p) = \sum_{p_0}^{p_f} P_I(p) R_P^x(p, V_P, V_S) + S_I(p) R_S^x(p, V_P, V_S)\,. \tag{4.5b}$$

Thereby Dankbaar (1985) expresses the free surface response as a function of the slowness

p as

$$R_P^z(p) = 2\,V_P/V_S \cdot \left((V_S/V_P)^2 - V_S^2\,p^2\right)^{1/2} \cdot (2V_S^2 \cdot p^2 - 1)/R_0(p) \tag{4.6a}$$

$$R_S^z(p) = 4\,V_S\ \cdot p \cdot \left((V_S/V_P)^2 - V_S^2\,p^2\right)^{1/2} \cdot (1 - V_S^2 \cdot p^2)^{1/2}/R_0(p) \tag{4.6b}$$

$$R_P^x(p) = 4\,V_P \cdot p \cdot \left((V_S/V_P)^2 - V_S^2\,p^2\right)^{1/2} \cdot (1 - V_S^2 \cdot p^2)^{1/2}/R_0(p) \tag{4.6c}$$

$$R_S^x(p) = 2\,(1 - V_S^2 \cdot p^2)^{1/2} \cdot (1 - 2V_S^2 \cdot p^2)/R_0(p) \tag{4.6d}$$

The R subscripts indicate the wave mode, and the superscripts the component direction, V_P and V_S refer to P- and S-wave velocities, and p is the horizontal slowness. The denominator is:

$$R_0(p) = (1 - 2V_S^2 \cdot p^2)^2 + 4\,p^2 V_S^2 \cdot \left((V_S/V_P)^2 - V_S^2\,p^2\right)^{1/2} \cdot (1 - V_S^2 \cdot p^2)^{1/2}$$

This allows the work to be carried out in the *Tau-p* domain, by using wave decomposition, as explained in the following [1].

4.3.3 Obtaining separated mode waves by the *Tau-p* transform

The *Tau-p* transform, also known as *slant-stack* (Claerbout, 1985), is an operation carried out on trace gathers, namely in the $t - h$ (*time-offset*) domain. It is achieved by applying a move-out of constant dip and summing amplitudes along offsets (Yilmaz, 2001). The data become separated by slowness p, therefore it is a plane wave decomposition. Mathematically it is defined as

$$\hat{u}(\tau, p) = \int_{-\infty}^{\infty} u(\tau + px, x)\mathrm{d}x\,, \tag{4.7}$$

where $u(t, x)$ is a seismic data record in time and space, and the transformed $\hat{u}(\tau, p)$ stands for the data in the intercept time (τ)-ray parameter (p) domain. The *Tau-p* transform is reversible, therefore it is possible to get back the data in the $t - x$ domain. See Appendix E for details.

[1] Dankbaar (1985) uses the abbreviations $\psi = V_S/V_P$, $\xi = \left(\psi^2 - V_S^2\,p^2\right)^{1/2}$ and $\eta = (1 - V_S^2 \cdot p^2)^{1/2}$. Therefore simpler forms appear: $R_P^v(p) = 2\,\psi^{-1} \cdot \xi \cdot (2V_S^2 \cdot p^2 - 1)/R_0(p)$, $R_S^v(p) = 4\,V_S\ \cdot p \cdot \xi \cdot \eta/R_0(p)$, $R_P^h(p) = 4\,V_P \cdot p \cdot \xi \cdot \eta/R_0(p)$, and $R_S^h(p) = 2\,\eta \cdot (1 - 2V_S^2 \cdot p^2)/R_0(p)$, with $R_0(p) = (1 - 2V_S^2 \cdot p^2)^2 + 4\,p^2 V_S \cdot \xi \cdot \eta$.

Following Dankbaar (1985) and Cary (1998), the *Tau-p* domain allows their inversion of equations 4.2a and 4.2b, to obtain the incident body waves. The tool to this method is a least-squares *Tau-p* algorithm on the frequency domain known as the *Discrete Radon Transform* (Appendix E), which has proven highly accurate (Marfurt et al., 1996).

Following Marfurt et al. (1996), the inverse discrete *Tau-p* transform in the frequency domain is

$$g(\omega, x) = \underset{\sim}{\mathcal{R}}(\omega, p, x)\hat{g}(\omega, p)\,, \tag{4.8}$$

where $\underset{\sim}{\mathcal{R}}$ is the inverse matrix operator with discrete elements defined by

$$R_{jk} = e^{i\omega p_j x_k}\,. \tag{4.9}$$

Equation 4.8 can also be represented in discrete shape as

$$g_k = \sum_{j=1}^{n_p} e^{i\omega p_j x_k}\hat{g}_j\,. \tag{4.10}$$

The *Tau-p* transform can be obtained by a least squares inversion according to:

$$\hat{g}(\omega, p) = \left[\underset{\sim}{\mathcal{R}}^H \underset{\sim}{\mathcal{R}}\right]^{-1} \underset{\sim}{\mathcal{R}}^H g(\omega, x) \tag{4.11}$$

where the exponent $[.]^H$ indicates the transpose conjugate matrix, and $[.]^{-1}$ indicates the inverse.

As for our problem, $\hat{g}(\omega, p)$ can be associated with the incident plane wave affected by the free-surface effect namely $u^z(p)$ and $u^x(p)$ in equations 4.5a and 4.5b, and $f(\omega, x)$ with the recorded vertical and horizontal components of the seismograms at a location x_k, both in the frequency domain. Thereby, from equations 4.5a and 4.5b:

$$\hat{g}(\omega, p_j) = \begin{pmatrix} \hat{g}_x(\omega, p_j) \\ \hat{g}_z(\omega, p_j) \end{pmatrix} = \begin{pmatrix} P_I(\omega, p_j)R_P^z(p_j, V_P, V_S) + S_I(\omega, p_j)R_S^z(p_j, V_P, V_S) \\ P_I(\omega, p_j)R_P^x(p_j, V_P, V_S) + S_I(\omega, p_j)R_S^x(p_j, V_P, V_S) \end{pmatrix}\,, \tag{4.12}$$

which, in matrix form, are:

$$\hat{g}(\omega, p_j) = \begin{pmatrix} R_P^z(p_j, V_P, V_S) & R_S^z(p_j, V_P, V_S) \\ R_P^x(p_j, V_P, V_S) & R_S^x(p_j, V_P, V_S) \end{pmatrix} \begin{pmatrix} P_I(\omega, p_j) \\ S_I(\omega, p_j) \end{pmatrix}\,. \tag{4.13}$$

This is a Tau-p form, therefore it is possible to obtain the inverse using equation 4.10:

$$g(\omega, x_k) = \begin{pmatrix} u^z(\omega, x_k) \\ u^x(\omega, x_k) \end{pmatrix} = \sum_{j=1}^{n_p} \left[e^{i\omega p_j x_k} \begin{pmatrix} R_P^z(p_j, V_P, V_S) & R_S^z(p_j, V_P, V_S) \\ R_P^x(p_j, V_P, V_S) & R_S^x(p_j, V_P, V_S) \end{pmatrix} \begin{pmatrix} P_I(\omega, p_j) \\ S_I(\omega, p_j) \end{pmatrix} \right] \tag{4.14}$$

These relations can be extended to all the values of x_k. Thus, the vertical component of the incident P-wave, after the free surface effect, is

$$\begin{pmatrix} u_P^z(\omega, x_1) \\ u_P^z(\omega, x_2) \\ \dots \\ u_P^z(\omega, x_{n_x}) \end{pmatrix} = \begin{pmatrix} e^{i\omega p_1 x_1} R_P^z(p_1) & e^{i\omega p_2 x_1} R_P^z(p_2) & \dots & e^{i\omega p_{n_p} x_1} R_P^z(p_{n_p}) \\ e^{i\omega p_1 x_2} R_P^z(p_1) & e^{i\omega p_2 x_2} R_P^z(p_2) & \dots & e^{i\omega p_{n_p} x_2} R_P^z(p_{n_p}) \\ \dots & & & \\ e^{i\omega p_1 x_{N_x}} R_P^z(p_1) & e^{i\omega p_2 x_{N_x}} R_P^z(p_2) & \dots & e^{i\omega p_{N_p} x_{n_x}} R_P^z(p_{n_p}) \end{pmatrix} \begin{pmatrix} P_I(\omega, p_1) \\ P_I(\omega, p_2) \\ \dots \\ P_I(\omega, p_{n_p}) \end{pmatrix} \tag{4.15}$$

where

$$R_P^z(p_j) = R_P^z(p_j, V_P, V_S).$$

Equation 4.15 can be abbreviated as:

$$u_P^z(\omega, \vec{x}) = \underset{\sim}{\mathcal{B}}_P^z(\omega, \vec{p}, \vec{x}) P_I(\omega, \vec{p}) \tag{4.16}$$

and analogously for the horizontal direction and also for the S-wave. Therefore we obatin a set of equations

$$\begin{pmatrix} u^z(\omega, \vec{x}) \\ u^x(\omega, \vec{x}) \end{pmatrix} = \begin{pmatrix} \underset{\sim}{\mathcal{B}}_P^z(\omega, \vec{p}, \vec{x}) & \underset{\sim}{\mathcal{B}}_S^z(\omega, \vec{p}, \vec{x}) \\ \underset{\sim}{\mathcal{B}}_P^x(\omega, \vec{p}, \vec{x}) & \underset{\sim}{\mathcal{B}}_S^x(\omega, \vec{p}, \vec{x}) \end{pmatrix} \begin{pmatrix} P_I(\omega, \vec{p}) \\ S_I(\omega, \vec{p}) \end{pmatrix} \tag{4.17}$$

which ca be represented as

$$\begin{pmatrix} u^z(\omega, \vec{x}) \\ u^x(\omega, \vec{x}) \end{pmatrix} = \underset{\sim}{\mathcal{B}}(\omega, \vec{p}, \vec{x}) \begin{pmatrix} P_I(\omega, \vec{p}) \\ S_I(\omega, \vec{p}) \end{pmatrix}. \tag{4.18}$$

It is possible to obtain the incident P and S waves from this expression, by using the least squares inversion algorithm (see e.g. Lines and Treitel, 1984), as follows:

$$\begin{pmatrix} P_I(\omega, \vec{p}) \\ S_I(\omega, \vec{p}) \end{pmatrix} = \left(\underset{\sim}{\mathcal{B}}(\omega, \vec{p}, \vec{x})^H \underset{\sim}{\mathcal{B}}(\omega, \vec{p}, \vec{x}) \right)^{-1} \underset{\sim}{\mathcal{B}}(\omega, \vec{p}, \vec{x})^H \begin{pmatrix} u^z(\omega, \vec{x}) \\ u^x(\omega, \vec{x}) \end{pmatrix}. \tag{4.19}$$

These equations allow finding the incident P and S-waves from the recorded vertical and horizontal components, if the near surface velocities are known.

4.4 Wave mode separation with topography

Complex geological settings can present strong variation over short distances, therefore it is better to assume the relevant properties, velocities and slope, local. These properties can change at each receiver location, and are common to the traces of the same CRG. A method for wave mode separation taking into account these characteristics follows.

4.4.1 Free-surface coefficients applied on a sloping free surface

The sloping surface seismic wave recording is illustrated in Fig. 4.6, using an incident P-wave, P_I. The recording components are vertical and horizontal, but the normal to the surface is not vertical due to the slope. The previous analysis about the free surface response and the wave mode separation by inversion assumes a flat horizontal surface with vertical and horizontal sensors. Therefore, to apply the previous approach, a coordinate rotation is required, such that the data correspond to the directions normal and parallel to the free surface.

Figure 4.6 shows the coordinate system x_0-z_0, that corresponds to the vertical and horizontal directions, namely the recording component directions. The receiver location is taken as the origin of the coordinate axes. The horizontal coordinate axis x_0 increases left to right, and the vertical one z_0 increases downward. The slope angle is ξ, and the rotated coordinate system is x_ξ-z_ξ. P_I corresponds to the incident P wave, P_R to the reflected P-wave, and S_R to the reflected S-wave.

The relations between the recorded components on the vertical and horizontal axes and the axes normal and parallel to the surface are

$$u_{z_\xi} = u_{z_0} \cos \xi - u_{x_0} \sin \xi \tag{4.20}$$

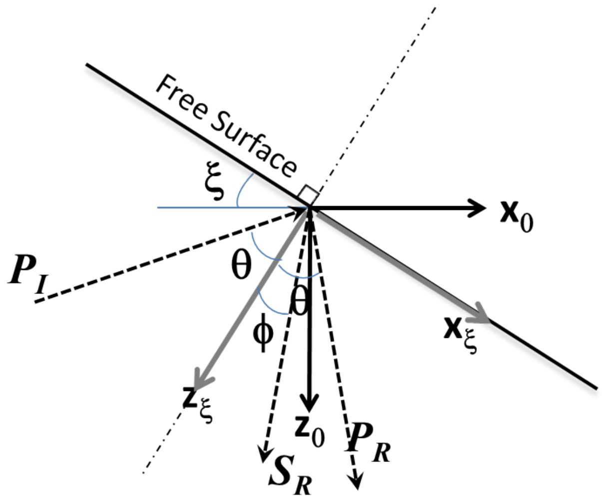

Figure 4.6: Analysis of a P-wave arrival at a sloping surface. Two coordinate axes are defined, x_0-z_0 corresponding to the horizontal and vertical directions, and x_ξ-z_ξ to the directions parallel and normal to the surface. P_I corresponds to the incident Pwave, P_R to the reflected P-wave, and S_R to the reflected S-wave.

and

$$u_{x_\xi} = u_{z_0} \sin \xi + u_{x_0} \cos \xi \, , \tag{4.21}$$

whose derivation is in Appendix C. These equations allow us to rotate the data recorded in the vertical and horizontal directions, and then apply the method of Section 4.3.3 to the data recorded on the sloping surface.

4.4.2 Angles of incidence at a receiver and the *Tau-p* transform

According to the method proposed in Section 4.3.3, a plane wave decomposition of the wavefield can be carried out by using the Tau-p transform, where the p values amounts to angles of incidence at the surface according to equation 4.3. The appropriate data gather must be selected such that the Tau-p transform can identify the right delay time Δt.

We compare the source gather (CSG) with the receiver gather (CRG) for this purpose. Figure 4.7 illustrates the analysis for waves arriving to a sloping free surface. We assume that G_1 is the receiver location to analyze. The required angle is θ_g. For a CRG, the Tau-p

transform takes the Δt between two traces, namely the traces corresponding to sources S_2 and S_1. However, this Δt corresponds to the angle θ_s (compare with Figure 4.5(a)). On the other hand, the Δt between receivers G_1 and G_2, from the CSG of source S_1 is the one corresponding to the angle θ_g, as required. Therefore, the appropriate domain in which to carry out the *Tau-p* transform is the CSG.

On the other hand, the properties can change at each receiver location, as has been discussed previously. Therefore, the analysis must be as local to the receiver as possible. A trade off for the requirement of local analysis and the integral character of the *Tau-p* transform (Equation 4.7), is a local *Tau-p* transform, which will be discussed in the next section.

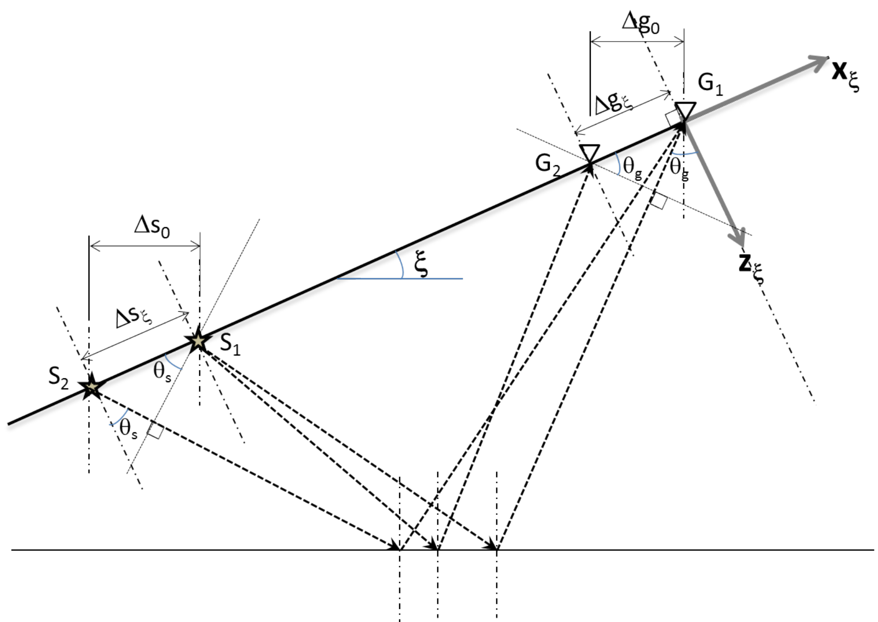

Figure 4.7: Analysis of the angles of incidence for a *PS*-wave arriving at a sloping, free surface: using a CRG the slowness corresponds to the sources, which, in general, is not the same as the angle of incidence at the receiver.

4.4.3 Application of the local *Tau-p* transform

Some authors have proposed a space variable or local *Tau-p* transform, such that a function $p - x$ can be defined, namely the variation of the slowness in space (McMechan, 1983; Milkereit, 1987). This transform is defined as (McMechan, 1983)

$$u_0(\tau, p) = \int_{x_0-\delta}^{x_0+\delta} u(\tau + px, x) W(x_0 - x) \mathrm{d}x \,, \tag{4.22}$$

where $u(t, x)$ stands for a seismic data record in time and space, x_0 is the reference location, and $W(x_0 - x)$ is a weight function that depends on the distance to the reference location.

The parameter δ, together with the weight function $W(x_0 - x)$, allows to select a gate with a number of traces sufficient to contribute to a more robust *Tau-p* transform, without losing the information of the angle of incidence at the receiver, or adding noise related to the horizontal variation of the surface properties. However, the minimum span is convenient for our local *Tau-p* transform[2] .

Regarding the weight function $W(x_0 - x)$, a *Gaussian* function is an appropriate option taking into account its properties , namely that it is a smooth function, that the weight decreases with distance, and that it allows to reconstruct a piecewise signal (Margrave et al., 2011). It is defined by the following equation:

$$W(x_0 - x) = a \exp\left(\frac{-(x_0 - x)^2}{2\sigma^2}\right) \tag{4.23}$$

where a is the peak value, which is assumed 1.0 for our purpose, x_0 is the position of the center of the peak, x are the positions of the other points, and σ defines the shape of the Gaussian with respect to the peak value. The parameter σ is the *standard deviation*[3], which characterizes the Gaussian shape in space coordinate units.

[2] A criteria to select δ based on the Fresnel zone has been proposed by Schultz (1976), who found that all the data that contributes to a slowness p span roughly a Fresnel zone of 10° arc at most.

[3] Mathematically, the standard deviation is: $\sigma = \sqrt{\frac{\sum_{i=1}^{N}(h_i - h_0)^2}{N}}$, or in words, the square root of the average of the squared differences from the mean. A distance of one Standard deviation includes 64 % of the area of the Gaussian, two times the standard deviation include 96% of the area and three times include 99%.

Therefore, using an appropriate Gaussian function, the distance δ in equation 4.22 can be properly defined, such that the amplitude values closer to the receiver of interest are enhanced (see Figure 4.15 for illustration).

Figure 4.8 shows a flow chart of the wave mode separation algorithm for a sloping free surface. Notice that the mode separation is carried about for each receiver into a CSG.

4.5 Model 1: a sloping free surface

Figure 4.9 illustrates a simple geological model with a sloping surface to test this method. The synthetic data was generated by ray tracing using the software Norsar-2D. Since ray-tracing allows to select specific seismic events, two tests on these data are presented in the following section, the first one with only PP and PS events, the second one with P and S-wave reflections generated by P and S-wave sources, yielding PP, SP, PS and SS data.

4.5.1 Modeling

The geologic model consists of a sloping free surface and a flat horizontal interface. The free surface slope is about 16.7 °. The model size is 1000 m by 1000 m, and the interface is at a depth of 600 m. There are 50 sources and 50 receivers, separated by 20 m. A zero-phase Ricker wavelet (see e.g. Sheriff and Geldart, 1995; Margrave, 2007) with a dominant frequency of 20 Hz was used as the energy source.

4.5.2 Receiver example 1

Examples corresponding to two receivers are presented in the following. The first one corresponds to the receiver located at x=1000 m (see Fig. 4.9). Figure 4.10 illustrates the resulting vertical and horizontal component gathers for 100 shots. Figure 4.11 illustrates the resulting P- and S- wave fields after wave mode separation using the method described. The second example corresponds to the receiver located at x=500. Figure 4.12 illustrates the

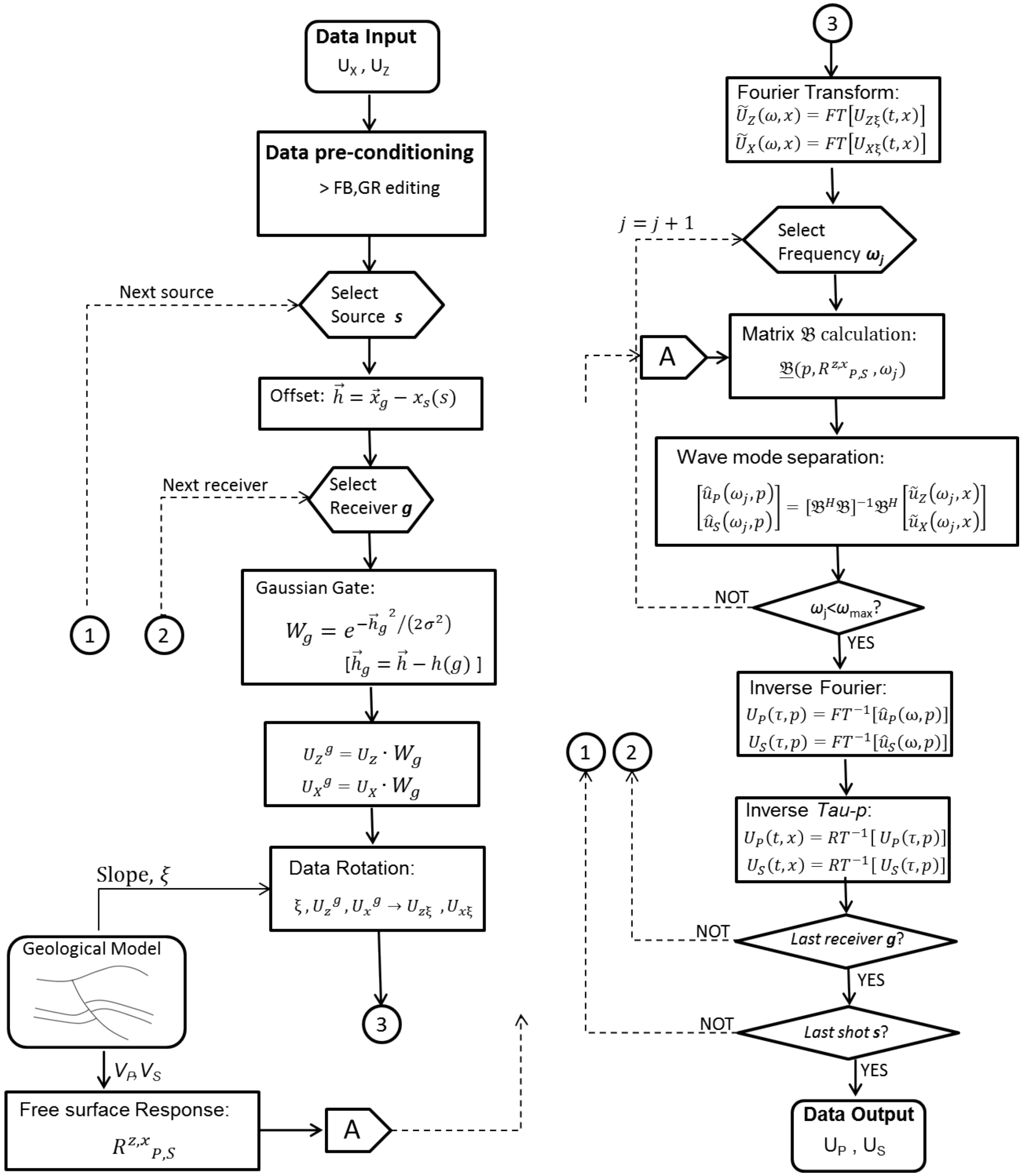

Figure 4.8: Flow diagram of the complex area wave-mode separation method.

resulting vertical and horizontal component gathers for 100 shots. Figure 4.13 illustrates the resulting P- and S- wave fields after wave mode separation. As expected, the S-wave arrives later in both cases, and shows features such as low energy at short offsets and reversal of polarity in both directions.

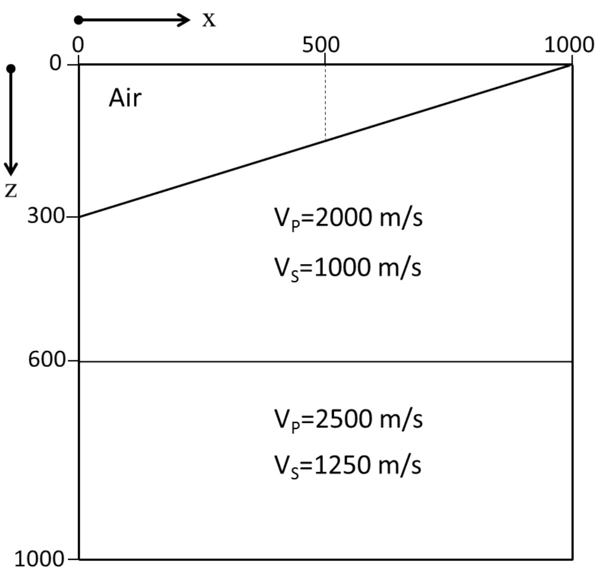

Figure 4.9: Geological model to test the method, illustrated by the P-wave velocity. Sources and receivers are located on the sloping surface.

4.6 Model 2: rough topography with a flat reflector

The second example to test the wave-mode separation method includes a rough topography that represents a hill. It is illustrated in Figure 4.14. The deep geology is also simple, a flat horizontal interface. The data was generated with the FD method, instead of RT as in the previous example (see Appendix D), which generates a more realistic wavefield that includes all the elastic events, unlike the previous example.

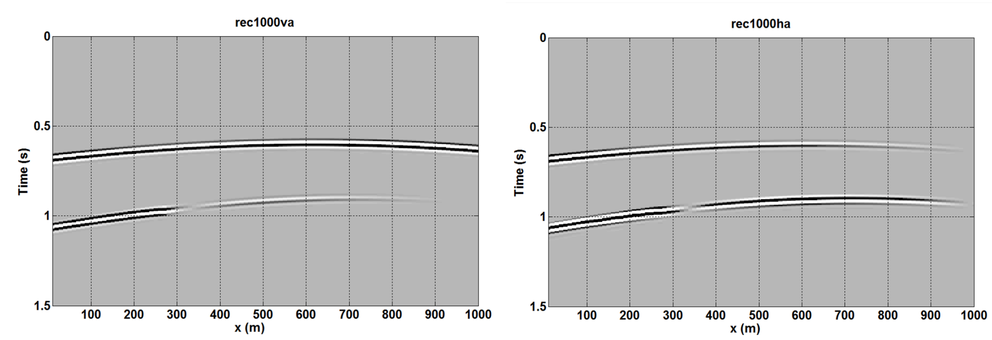

Figure 4.10: Common receiver gathers at the receiver located in x=1000 m. (a) Vertical component. (b) Horizontal component

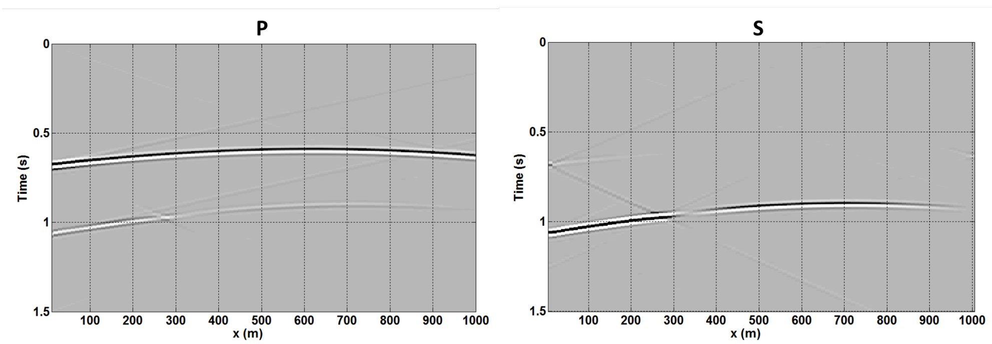

Figure 4.11: P- and S- wave fields after the wave mode separation for the receiver at x=1000 m. (a) P-wave (b) S-wave.

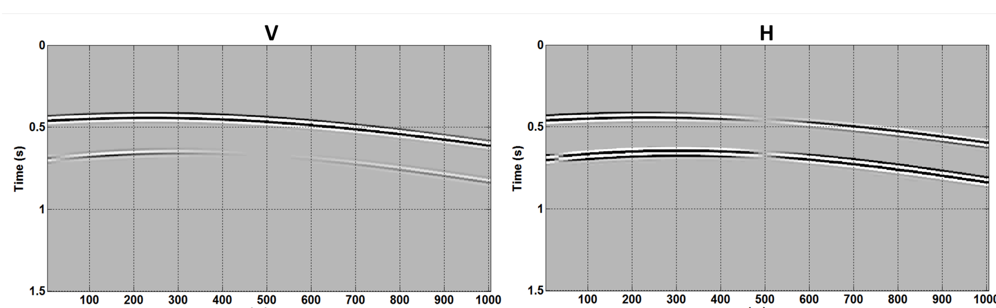

Figure 4.12: Common receiver gathers at the receiver located in x=500 m. (a) Vertical component. (b) Horizontal component

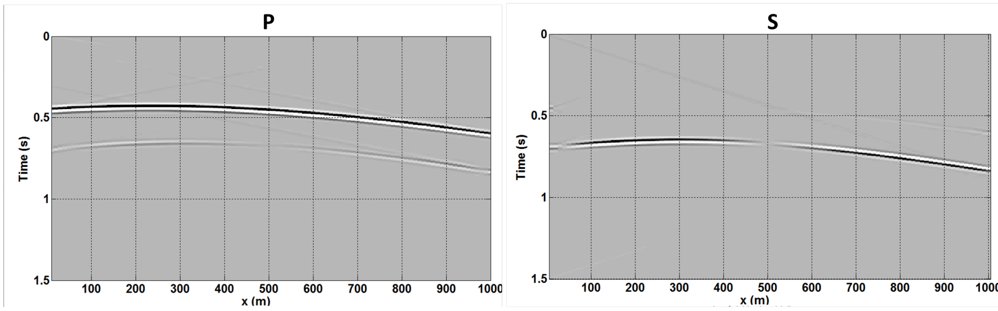

Figure 4.13: P- and S- wave fields after the wave mode separation for the receiver at x=500 m. (a) P-wave (b) S-wave.

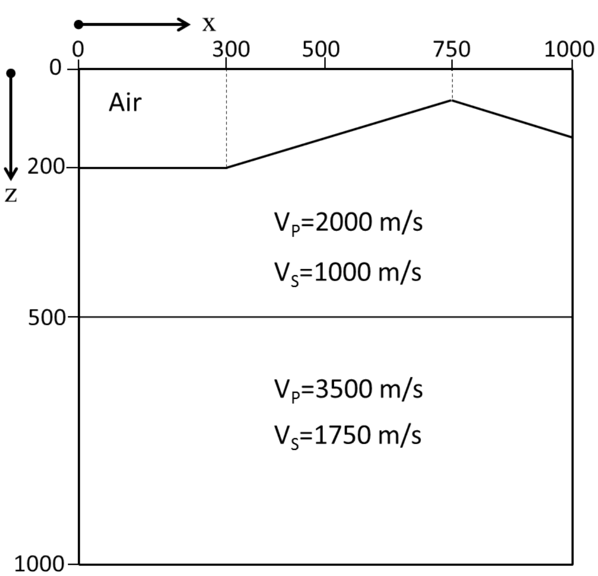

Figure 4.14: Model 2: a rough topography with a flat reflector.

4.6.1 Modeling

The seismic survey included 41 shots separated by 20 m from each other, between x=100 and x=900 m. There are 200 receivers on the surface, separated 5 m from each other. As in the previous example, the source of energy is a zero-phase Ricker wavelet with a dominant frequency of 20 Hz. Figure 4.16 illustrates the vertical and horizontal component records typical of this modeling, by the source of energy located at x=800 m. Notice differences between both records, however, also some events that appear in both, which can be identified as *leakage* between wave modes.

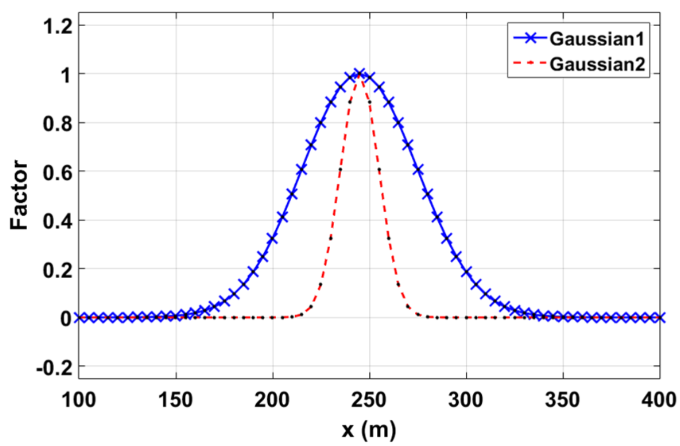

Figure 4.15: The Gaussian function gates for the wave mode separation, input and output, corresponding to the receiver located at x=245 m. The input data gate is wider, with σ=30 m (blue continuous line with crosses), and the output is narrower (dashed red line with dots), with σ=10 m.

4.6.2 Test on individual shots

The method just described in the flow chart of Figure 4.8 was applied to hte modeling data. Figure 4.15 illustrates the Gaussian function used as a gate for the *Tau-p* transform, the wider for the input and the narrower for the output. Figure 4.17 illustrates the resulting records, after wave mode separation. As for comparison, Figure 4.18 illustrates the arrival times for PP-wave (4.18(a)) and PS-wave (4.18(b)), obtained with ray-tracing. Notice that events corresponding to the other wave-mode have been attenuated in Figure 4.17, comparing with the input data (Figure 4.16) and the arrival times from ray-tracing (Figure 4.18).

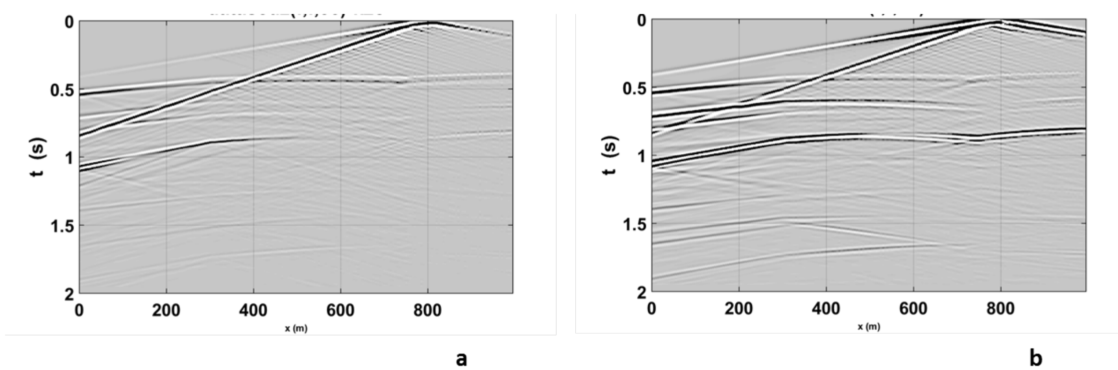

Figure 4.16: Seismic data of Model 2 before wave mode separation. It corresponds to source No. 36, located at x=800 (a) Vertical component (b) horizontal component.

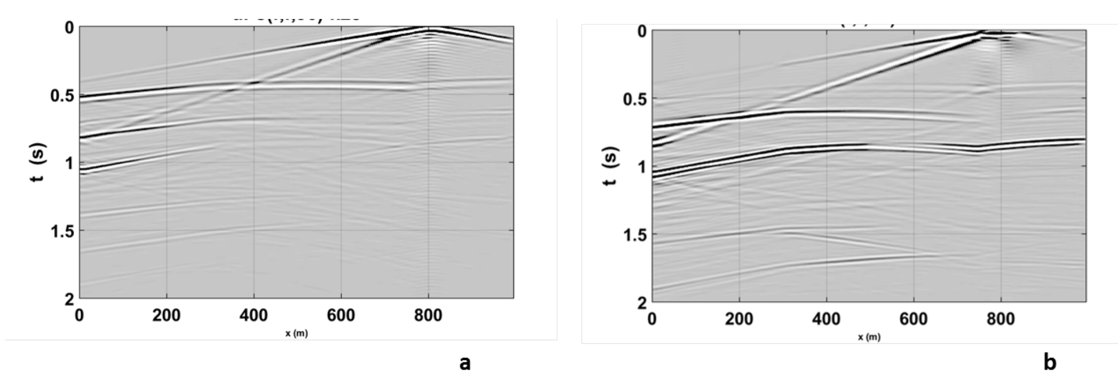

Figure 4.17: Seismic data of Model 2 after wave mode separation. It corresponds to source No. 36, located at x=800 (a) P-wave field, (b) S-wave field.

4.7 Conclusions

- A method for wave mode separation in a complex setting has been proposed, taking into account the topography and using the frees surface response according to the approach of Dankbaar (1985).

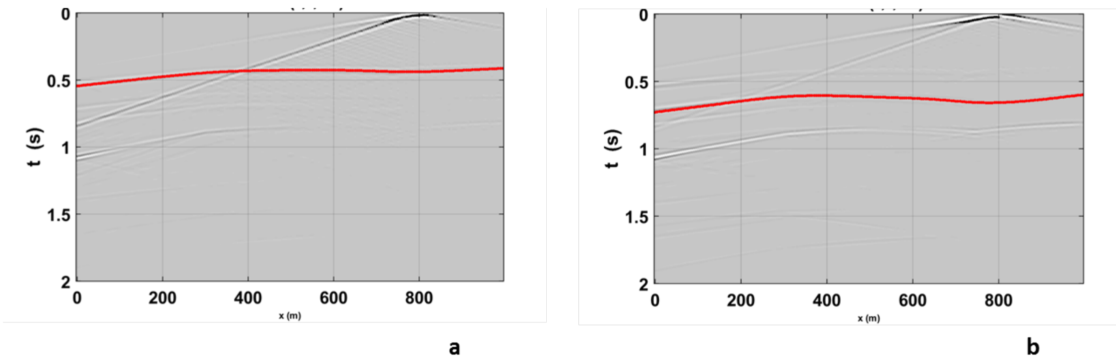

Figure 4.18: Arrival time of seismic data of Model 2 using ray-tracing. Example of source No. 36, located at x=800. (a) PP-wave (b) PS-wave.

- The near surface velocities for P and S-waves, and the surface slope at each receiver location are required. Vertical deployment of the multicomponent receivers is assumed.

- The method works on the CSG domain, on a receiver basis, selecting a subset of traces (receivers) for each calculation pertaining to one location, such that it is possible to obtain the angle of incidence to the free surface.

- Assuming that the relevant properties typically can change for each receiver, a local Tau-p transform has been applied at each receiver location to obtain the required plane wave decomposition.

- The first example, from a simple model (one slope and one reflector) and with data generated by using ray tracing, show the expected wave mode separation.

- The example from a complex topography model, using FD modeling, shows a reasonable resulting wave mode separation too, specially noticeable in far offsets.

Chapter 5

PS-wave processing in complex areas: PreSDM from topography

5.1 Introduction

Methods like the statics correction (Chapter 3) suffice if the NSL irregularities are relatively minor. In the case of complex areas, the rough topography, the weathering variations and the outcrops of geological structures can introduce strong effects in the geometry and amplitude of the reflections (Gray and Marfurt, 1995). Methods that better honor the wave equation propagation laws become more advisable. One of them is *wave-equation datuming*, (e.g. Berryhill, 1979; Shtivelman and Canning, 1988; Salinas, 1996), which allows to extrapolate the wavefield to an arbitrary reference surface. Another one is performing migration from the topography[1] instead of the usual flat reference datum (Reshef, 1991; Bevc, 1995). An investigation of migration from topography applied to multicomponent data is presented in this chapter.

In section 1.4.2 (Figure 1.5(b)), migration after stack is included in the conventional processing flow for PS-wave. In addition, time migration before stack has also became commonly applied (e.g. Li et al., 2007; Cary and Zhang, 2011). On the other hand, Prestack Depth Migration (PreSDM), although less popular, has attractive properties for complex areas. It also appears convenient for PS-waves, since their complex travel path depends more on the properties of the media (e.g. Thomsen, 1999), becoming less proper the simplified assumptions of time processing (Bancroft, 2007). Besides that, an issue of PS-waves time sections, the identification of corresponding PP and PS reflections (known as the *registration*

[1] See section 1.3.2 for basic ideas on migration.

issue), would also benefit from depth migration. Thus, depth migration methods exhibit attractive properties for PS-waves.

Prestack migration can be carried out into two schemes *shot-profile* and *source-receiver* (Claerbout, 1985; Biondi, 2006). In this work, migration methods were applied in the shot-profile domain, which appears more convenient, taking into account the commonly coarse and irregular sampling of sources in complex areas. Two approaches are implemented, Kirchhoff and PSPI, based on scalar algorithms developed for PP-waves. The methods are tested on synthetic data from a geological model with topography and complex structure, generated with an elastic 2-D FD code. The wave separation method introduced in Chapter 4 is tested with this data.

5.2 Theory

It follows a brief explanation about relevant characteristics of the two migration methods applied, Kirchhoff and PSPI.

5.2.1 Kirchhoff method

The theoretical model is derived from Green's Theorem, which relates a vector field in the interior of a volume with the field on the surface (Shearer, 1999). The Kirchhoff equation results, following Wiggins (1984), may be written as

$$U(\vec{x},t) = \frac{-1}{v} \int_{S_0} \frac{1}{r} \frac{\partial r}{\partial n} \left[\frac{\partial U_0}{\partial t} \left(\vec{x_0}, t + \frac{r}{v} \right) \right] \mathrm{d}S_0 \quad , \tag{5.1}$$

where $\frac{1}{r}$ corrects for spherical spreading, and $\frac{\partial r}{\partial n}$ for obliquity. This equation allows us to obtain the wavefield $U(\vec{x},t)$ at a point $\vec{x}$ in the interior of a volume enclosed by the surface S_0, as a function of the measurements $U_0(\vec{x_0},t)$ at the point $\vec{x_0}$ on the surface (see e.g. Shearer, 1999; Wiggins, 1984). The distance r is defined as $r = |\vec{x} - \vec{x_0}|$, n represents the normal to the surface at $\vec{x_0}$, and v is the propagation velocity.

Equation 5.1 performs an extrapolation, which can be used for other purposes besides migration, such as for wave equation datuming (e.g. Berryhill, 1979; Salinas, 1996). Wiggins (1984) presents a Kirchhoff extrapolation method for non-planar data, between two surfaces, which can have any shape. If sources and receivers are in plane S_0 and we want to extrapolate the data to plane S_1, we can use Equation 5.1 applied twice and call the reciprocity principle (see e.g. Claerbout, 1985), resulting the equation

$$U(\vec{x}_1, \vec{x}_1\prime, t) = \frac{1}{v^2} \int_{S_{0_s}} \int_{S_{0_g}} \frac{1}{r_s} \frac{1}{r_g} \frac{\partial r_s}{\partial n} \frac{\partial r_g}{\partial n} \left[\frac{\partial U_0}{\partial t} \left(\vec{x}_{0_s}, \vec{x}_{0_g}, t + \frac{r_s + r_g}{v} \right) \right] dS_{0_s} dS_{0_g} \, , \tag{5.2}$$

termed KRK by Wiggins (1984), for "Kirchhoff-Reflection-Kirchhoff". The distance r_s is defined as $r_s = |\vec{x}_s - \vec{x}_1|$, and r_g is defined as $r_g = |\vec{x}_g - \vec{x}_1'|$.

This extrapolation equation becomes a migration method if the *imaging condition* is called for. The imaging condition requires that the events be simultaneous, and at the same point (the reflection point). Thus, migration at a point $\vec{x}_\xi$ is

$$I(\vec{x}_\xi) = U(\vec{x}_\xi, \vec{x}_\xi, 0) = \frac{-1}{v^2} \int_{S_s} \int_{S_g} \frac{1}{r_s} \frac{1}{r_g} \frac{\partial r_s}{\partial n} \frac{\partial r_g}{\partial n} \left[\frac{\partial^2 U_0}{\partial t^2} \left(\vec{x}_{0_g}, \vec{x}_{0_s}, \frac{r_g + r_s}{v} \right) \right] dS_g dS_s \quad , \tag{5.3}$$

where $r_s = |\vec{x}_s - \vec{x}_\xi|$, and $r_g = |\vec{x}_g - \vec{x}_\xi|$. This migration is valid for 3-D data of PP waves, with constant velocity.

Following Biondi (2006), the Kirchhoff method of shot-profile prestack migration in 2-D, for a point inside the media located at x_ξ, z_ξ, can be represented in a generalized form as:

$$I_s(\vec{x}_\xi) = \int_\Sigma W(\vec{x}_\xi, \vec{x}_s, \vec{x}_g) U[\vec{x}_s, \vec{x}_g, t = t(\vec{x}_\xi, \vec{x}_s) + t(\vec{x}_\xi, \vec{x}_g)] \, \mathrm{d}x_g \tag{5.4}$$

where $\vec{x}_\xi = (x_\xi, z_\xi)$, $W(\vec{x}_\xi, \vec{x}_s, \vec{x}_g)$ represents the amplitude weight correction obtained according to the Kirchhoff theory, $U[t, \vec{x}_s, \vec{x}_g]$ the input wavefield with source at $\vec{x}_s$ and receiver at $\vec{x}_g$ (a shot gather in this case), $I_s(\vec{x}_\xi)$ is the migrated image, Σ is the *migration aperture*[2], $t(\vec{x}_s, \vec{x}_\xi)$ is the travel time from the source to the reflection point, and $t(\vec{x}_\xi, \vec{x}_g)$ is the travel time between the reflection point inside the medium and the receiver. PreSDM for PP

[2]Migration aperture is defined by Yilmaz (2001) as the spatial extent that the actual summation spans in Kirchhoff migration.

and PS waves with topography can be represented by equation 5.4. Times $t(\vec{x}_s, \vec{x_\xi})$ and $t(\vec{x_\xi}, \vec{x}_g)$ are obtained from forward modeling, such as ray tracing, over a previously provided velocity model. In the case of PS-waves are required P wave velocity at the source side and S wave velocity at the receiver side. Figure 5.1 shows the flow chart for this Kirchhoff multicomponent PreSDM from topography.

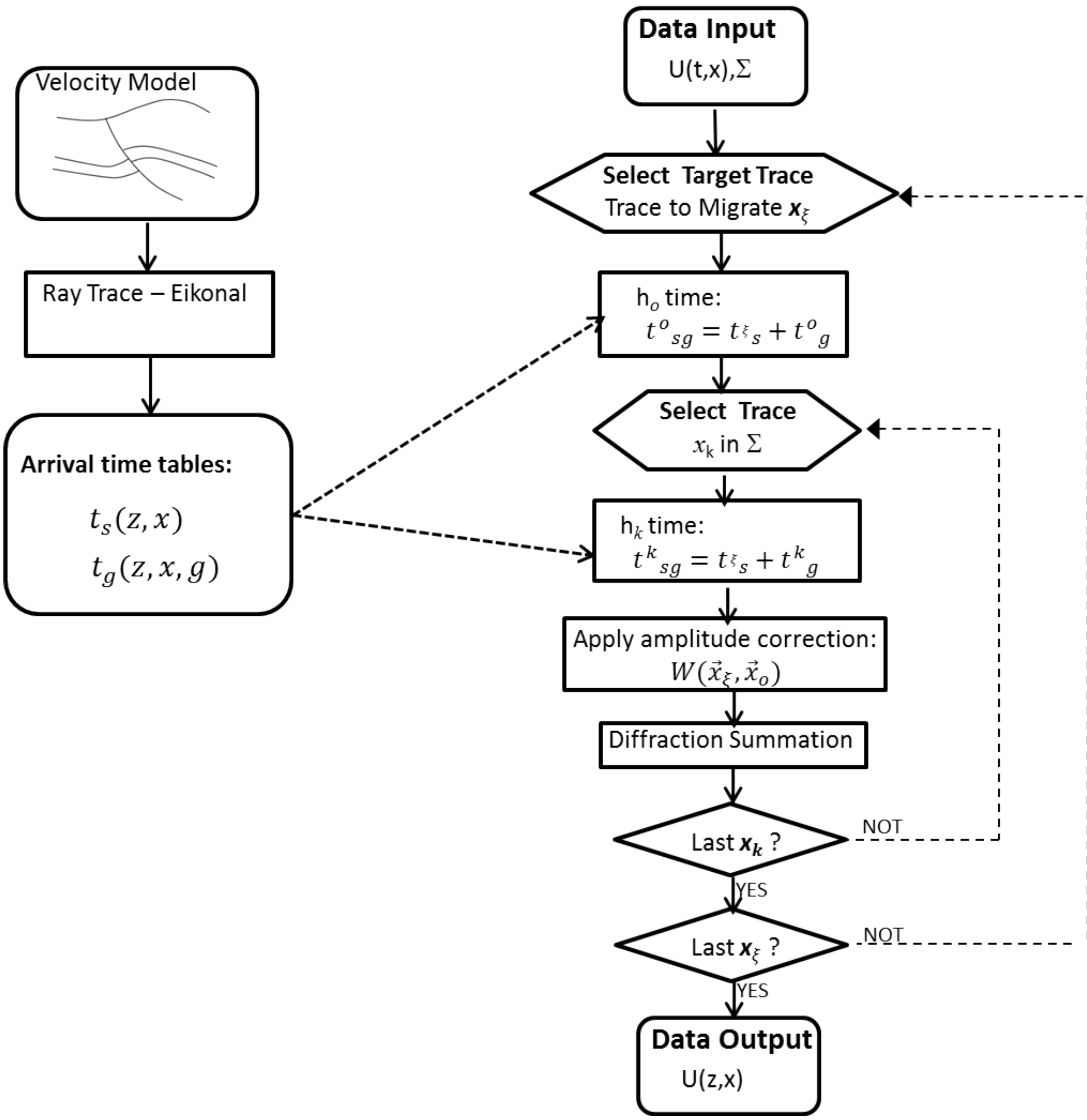

Figure 5.1: Flow chart for a Kirchhoff multicomponent PreSDM with topography.

5.2.2 PSPI method

The 2-D scalar wave equation after the Fourier transform in the coordinates x and t, that is as a function $\tilde{\tilde{U}}(k_x, \omega, z)$, can be separated into two one-way wave equations. The down-going wave is

$$\frac{\partial \tilde{\tilde{U}}(k_x, z, \omega)}{\partial z} = i k_z \tilde{\tilde{U}}(k_x, z, \omega) \quad , \tag{5.5}$$

where

$$k_z = \frac{\omega}{v} \sqrt{1 - \left(\frac{k_x v}{\omega}\right)^2} \quad .$$

Equation 5.5 has the solution

$$\tilde{\tilde{U}}_{z+\Delta z}(\omega, k_x) = \tilde{\tilde{U}}_z(\omega, k_x) e^{(i k_z \Delta z)} \quad , \tag{5.6}$$

which can be verified by substitution. This is the *Phase shift* extrapolation equation.

The migration method based on this approach is known as *Phase-Shift migration.* However, it cannot handle lateral velocity variations. A method known as *Phase Shift plus Interpolation*, shortened to *PSPI*, was proposed to overcome this shortcoming (Gazdag and Sguazzero, 1984b). Basically, a number of Phase-shift migrations, each one with a different velocity corresponding to lateral variations, is carried out, and the results are interpolated.

The approach of Margrave and Ferguson (1999) allows more continuous variation of the velocity in x (see also Ferguson and Margrave, 2005; Bale, 2006). The preSDM algorithm of Al-Saleh et al. (2009), based on this approach, is used in this work. The extrapolation equation (backward propagation) for the upgoing wavefield $\tilde{U}(x, \omega)$, following Al-Saleh (2006), is

$$\tilde{U}_{n\Delta z}(x, \omega) = \frac{1}{2\pi} \int \int_{-\infty}^{\infty} \tilde{U}_{(n-1)\Delta z}(x', \omega) e^{-i k_x x'} \, \mathrm{d}x' e^{i\sqrt{k_n^2 - k_x^2}\Delta z} e^{-i k_x x} \, \mathrm{d}k_x \quad ,$$

where Δz is the depth step size, n is the number of the depth step, ω is the temporal frequency, k_x is the wavenumber in the direction x, and k_n is the magnitude of the wavenumber vector at the time n. An analogous expression can be written for the downgoing wavefield at the source side,

$$\tilde{D}_{n\Delta z}(x,\omega) = \frac{1}{2\pi}\int\int_{-\infty}^{\infty}\tilde{D}_{(n-1)+\Delta z}(x',\omega)e^{-ik_x x'}\,\mathrm{d}x' e^{-i\sqrt{k_n^2-k_x^2}\Delta z}e^{-ik_x x}\,\mathrm{d}k_x \quad .$$

As for the source it was used the free-space Green function G_0, using a Hankel function of the first kind $H_0^{(1)}$, evaluated at the depth level below its nominal location on the surface (see Al-Saleh et al., 2009).

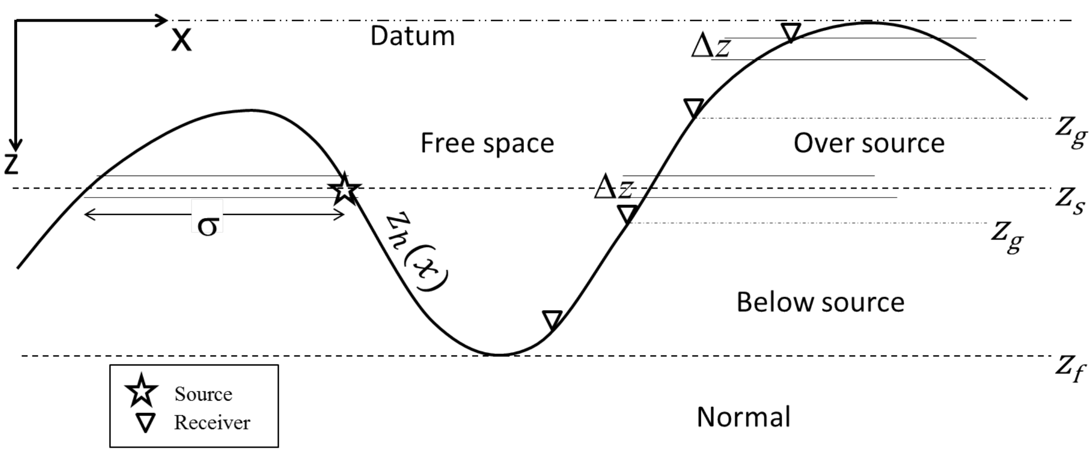

Figure 5.2: Illustration of the space domain types in the PSPI migration from topography.

The deconvolution imaging condition, following Al-Saleh (2006) and according to Claerbout (1971), is

$$I(x,z) = \int_{\omega_i}^{\omega_f}\frac{U(x,z,\omega)D^*(x,z,\omega)}{D(x,z;\omega)D^*(x,z,\omega)+\mu I_{max}(z)}\mathrm{d}\omega \tag{5.7}$$

where the asterisk ($*$) indicates a conjugate, and $\mu I_{max}(z)$ is a stabilizing factor. The integral over ω amounts to $t=0$, corresponding to the imaging condition.

From this approach Al-Saleh et al. (2009) derived the algorithm for preSDM from topography. Figure 5.2 illustrates the relevant properties of topography. The surface elevation as a function of the horizontal coordinate is represented by $z_h(x)$. The receiver elevations are z_g, the source elevation is z_s, and the lowest topography elevation is z_f.

The flow chart of Figure 5.3 illustrates the migration procedure. The extrapolation below z_f is just the usual for a flat surface. It is represented by the function Φ. Above it we

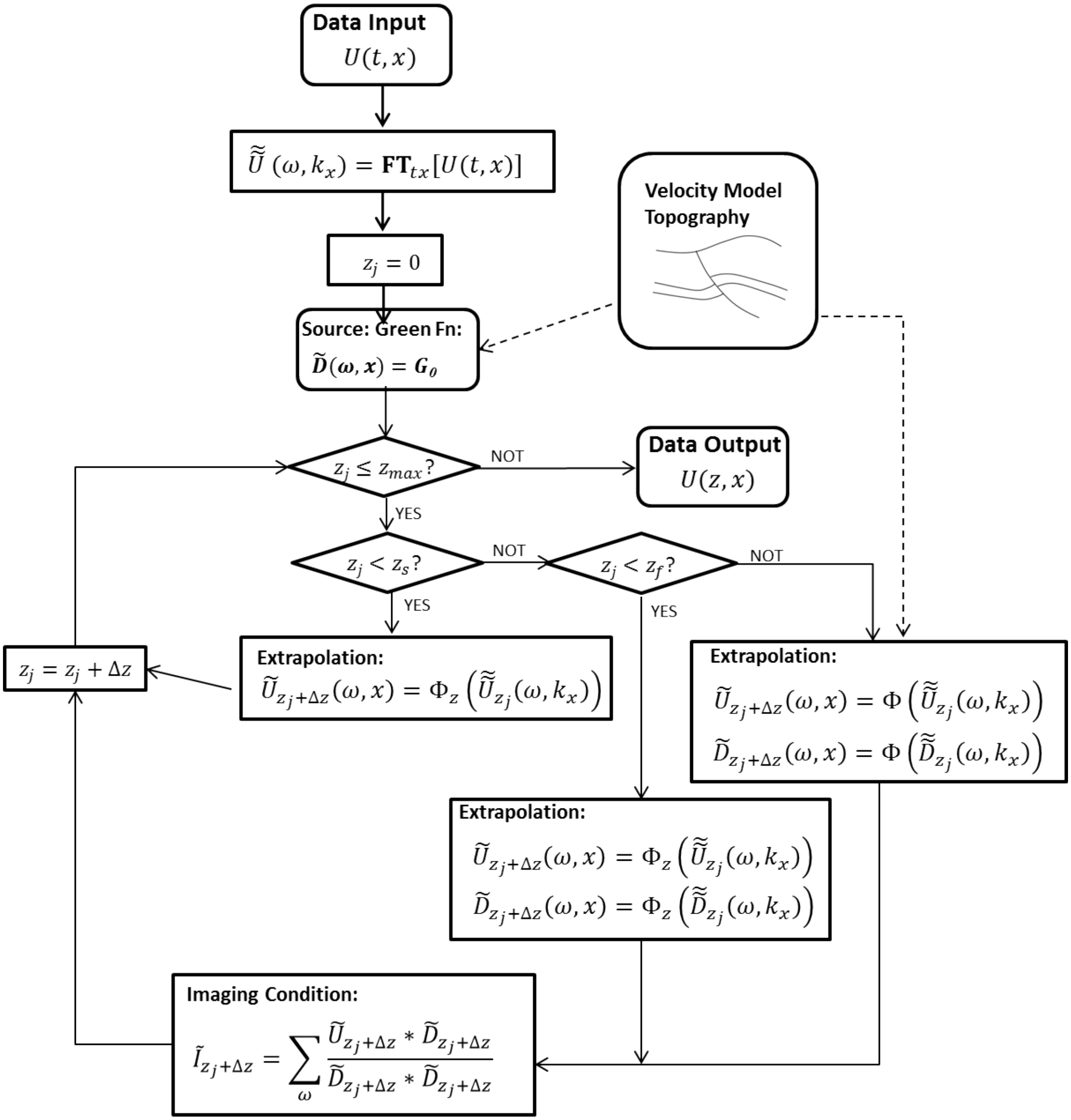

Figure 5.3: Flow diagram for prestack PSPI migration with topography.The depths z_s,z_g, and z_{tm} are illustrated in figure 5.2. The extrapolation function Φ_z is explained in figure 5.4.

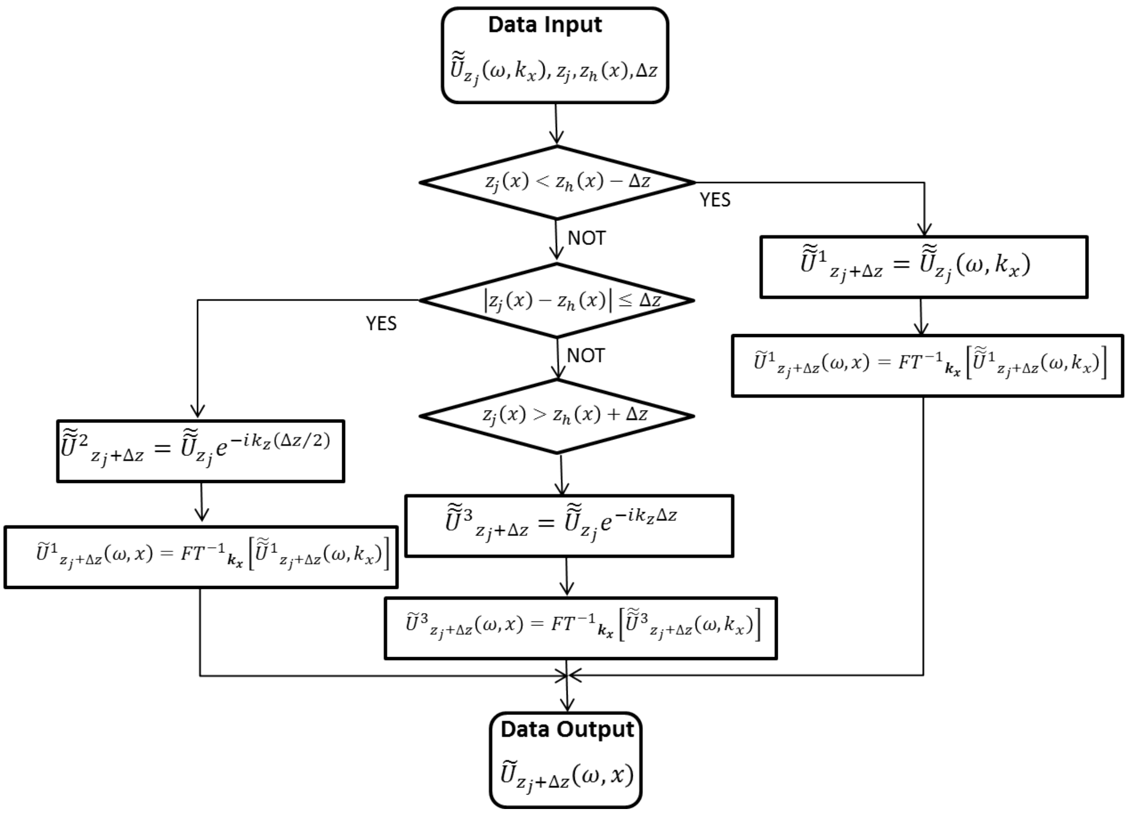

Figure 5.4: Flow chart of the function Φ_z that carries out the phase-shift extrapolation with topography.

define the *topography zone*, where the extrapolation depends on the location of the current elevation z_j compared with the source location z_s. The extrapolation in the topography zone is represented by the function Φ_z, described in Figure 5.4. It allows the variation of properties in the horizontal direction x, since at the same level it is possible to have locations inside of the terrain, on the surface, or above the surface, which define what kind of extrapolation is required.

5.3 Application to synthetic data

These methods were tested on a synthetic data set. The following paragraphs describe first the data set, then the wave mode separation application is presented and finally the migration methods are applied.

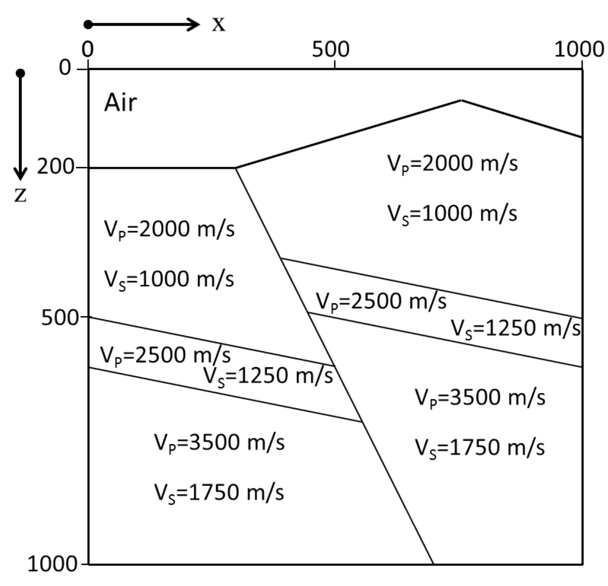

Figure 5.5: Geological model with topography and structure to test the PreSDM methods. The surface shows a 135 m high hill. A dipping layer with an inverse fault is the target.

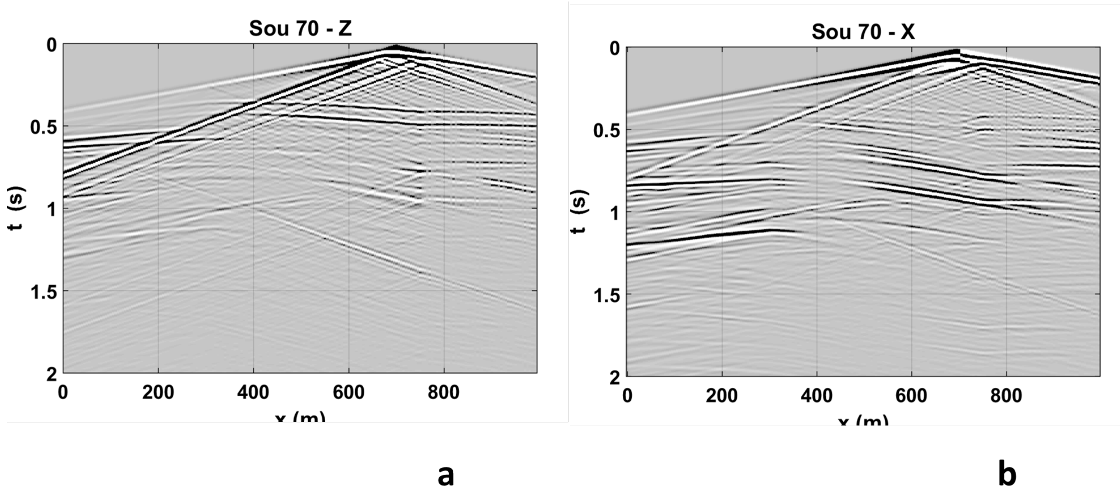

Figure 5.6: An example of the synthetic records obtained with elastic FD difference modeling, corresponding to shot 70 (x=700 m). (a) Vertical component (b) horizontal component.

5.3.1 Synthetic data generation

Figure 5.5 illustrated the geological model used to generate the synthetic data. Its dimensions are 1000 m horizontal and 1000 m vertical. Rough topography is represented by a hill with a slope of 16° and a height of 135 m above the ground plane. The complex geological structure includes a fault with 65° slope and a dipping layer with about 12° slope, which is assumed to be the imaging target. The velocities of this layer are V_P of 2500 m/s and V_S 1250 m/s.

The synthetic data were generated with the finite difference (FD) method, using a 2D, elastic, isotropic algorithm (Hayashi et al., 2001), which allows implementing an irregular surface. Forty one shots were generated, from location $x = 100$ m to $x = 900$ m at intervals of 20 m. The receivers are on the free surface, separated 5 m, for a total of 200. Time sampling is 2 ms, and the record length is 2 s. The source is a symmetrical Ricker wavelet with a center frequency of 20 Hz and a length of 100 ms, starting at zero time.

Figure 5.6 shows an example of one of the resulting shot gathers, whose source is located at x 700 m. Figure 5.6a corresponds to the vertical component and Figure 5.6b to the horizontal component. Many events can be observed on both records, principally P-waves on the vertical component and S-waves on the horizontal, as expected.

5.3.2 Wave mode separation

The wave mode separation method of Chapter 4 was applied to the synthetic data just described. A Gaussian gate (equation 4.23) was applied to the input with a standard deviation σ of 30 m, equivalent to six receiver spacings.

The result is illustrated by Figure 5.8, corresponding to the shot gathers of Figure 5.6. Figure 5.8a corresponds to the P-wave and Figure 5.8b to the S-wave. Arrival times calculated with ray-tracing (using Norsar-2D®) show up in Figure 5.7, over low gain records, P-wave arrivals in Figure 5.7a and S-wave arrivals in Figure 5.7b. Notice that events identified as leakage have been attenuated in Figure 5.8 compared to Figure 5.6. Events properly identified as the corresponding wave-mode by ray tracing appear stronger after wave mode separation. Notice that some leakage energy is still present in the right-hand side of Figure 5.8(b).

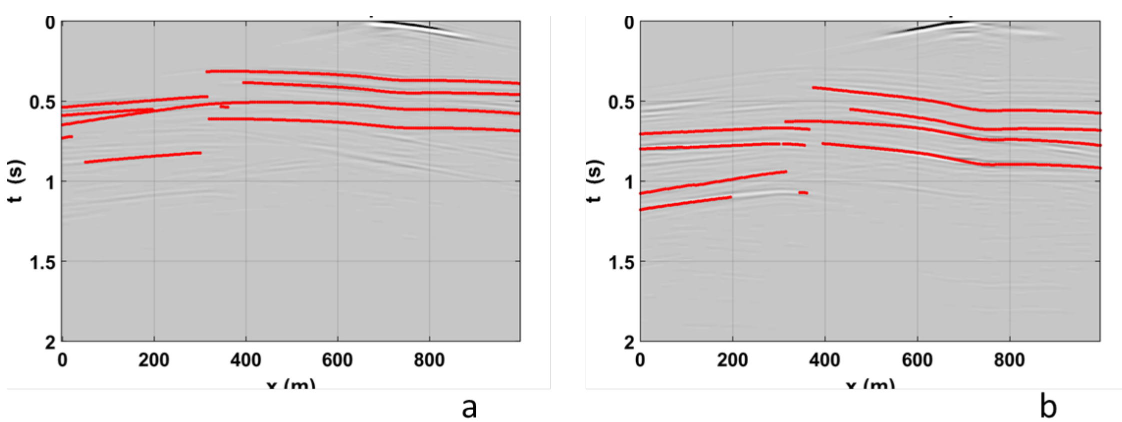

Figure 5.7: Arrival times obtained by ray-tracing for the synthetic record shot 70 (x=700 m) on a low gain seismic record. (a) P-waves (b) S-waves.

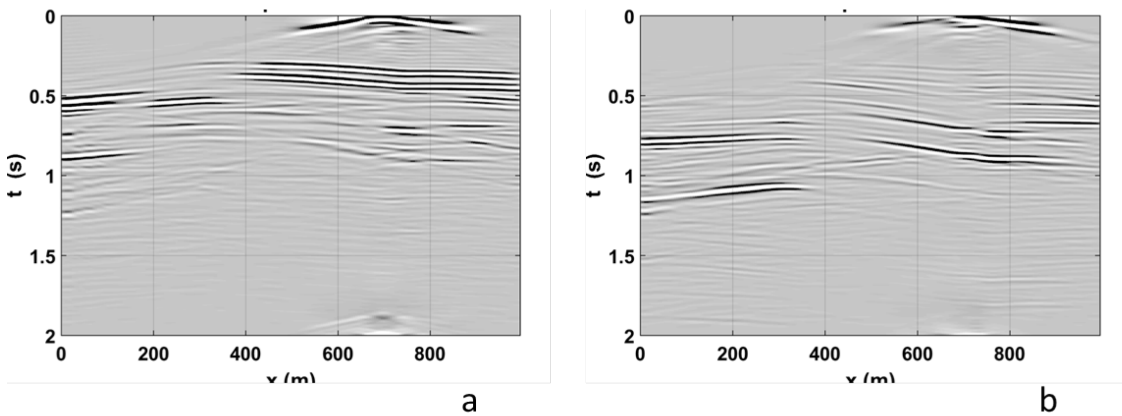

Figure 5.8: Seismic events after wave mode separation for the synthetic gather corresponding to shot 70 (x=700 m). (a) P-waves (b) S-waves. Notice that leakage events (compare with Figures 5.6 and 5.7) have been attenuated specially at the far offsets, however other remain.

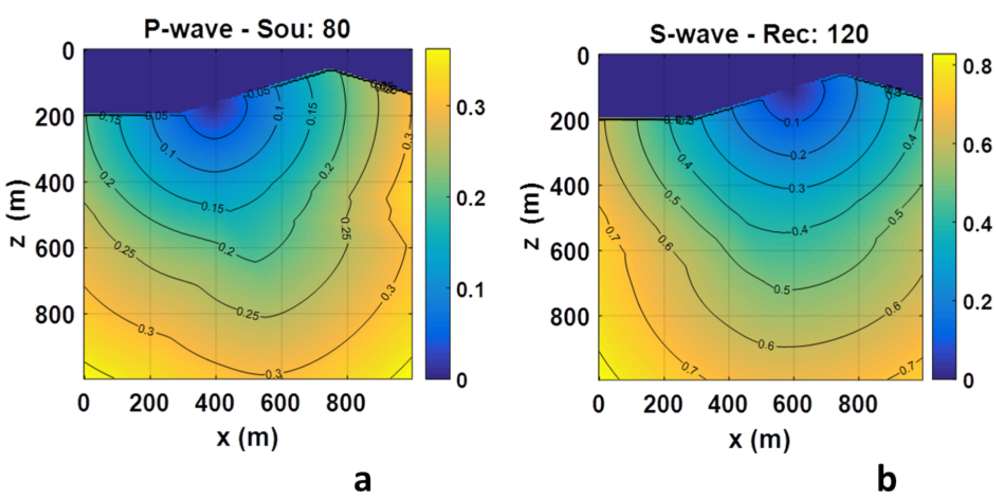

Figure 5.9: Arrival times table examples for Kirchhoff migration (a) P-wave shot at x=400 m (b) S-wave, receiver at x=600 m.

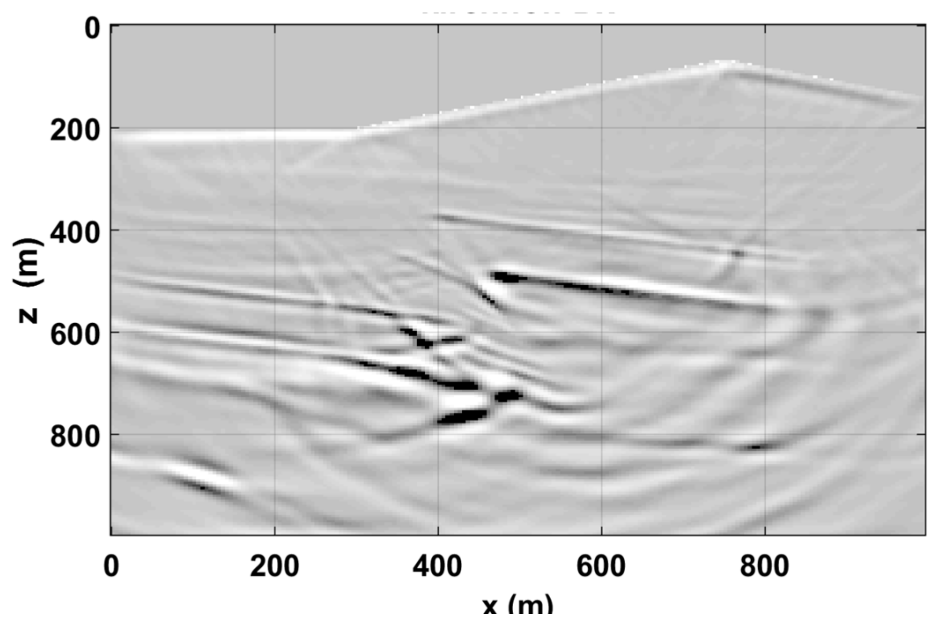

Figure 5.10: Kirchhoff PreSDM for the PS-wave using the horizontal component, without wave mode separation.

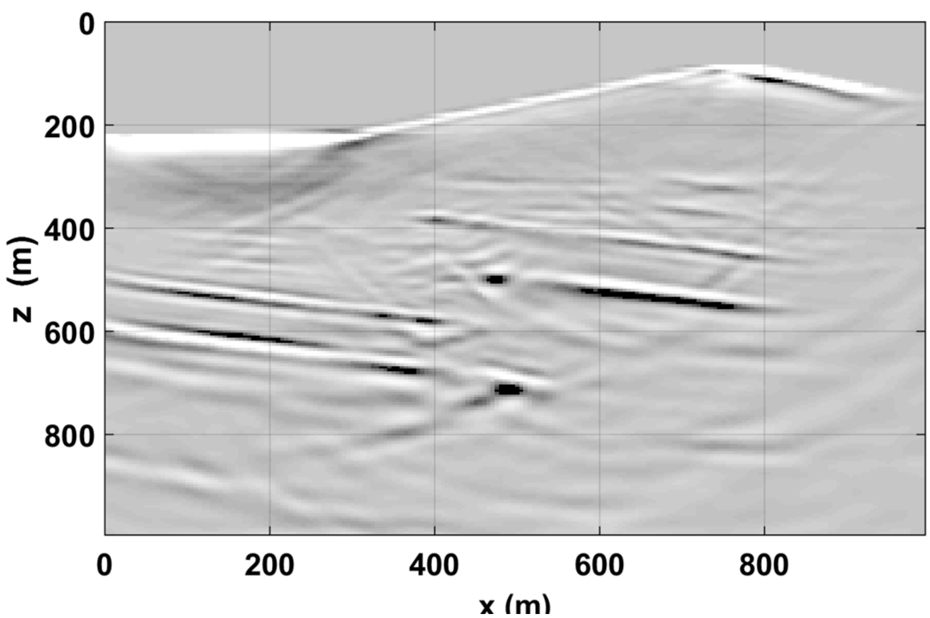

Figure 5.11: Kirchhoff PreSDM for the PS-wave after wave mode separation.

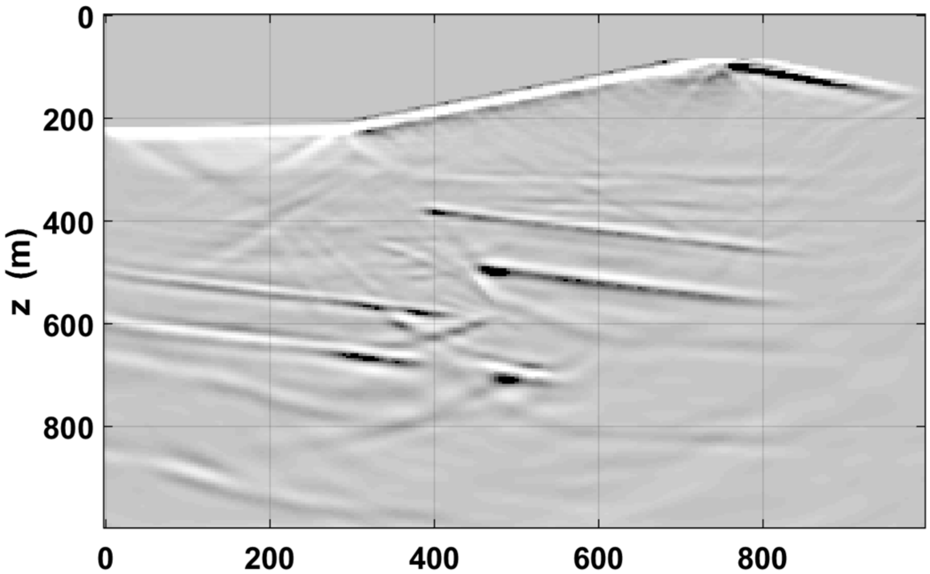

Figure 5.12: PSPI PreSDM for the PS-wave using the horizontal component, without wave mode separation.

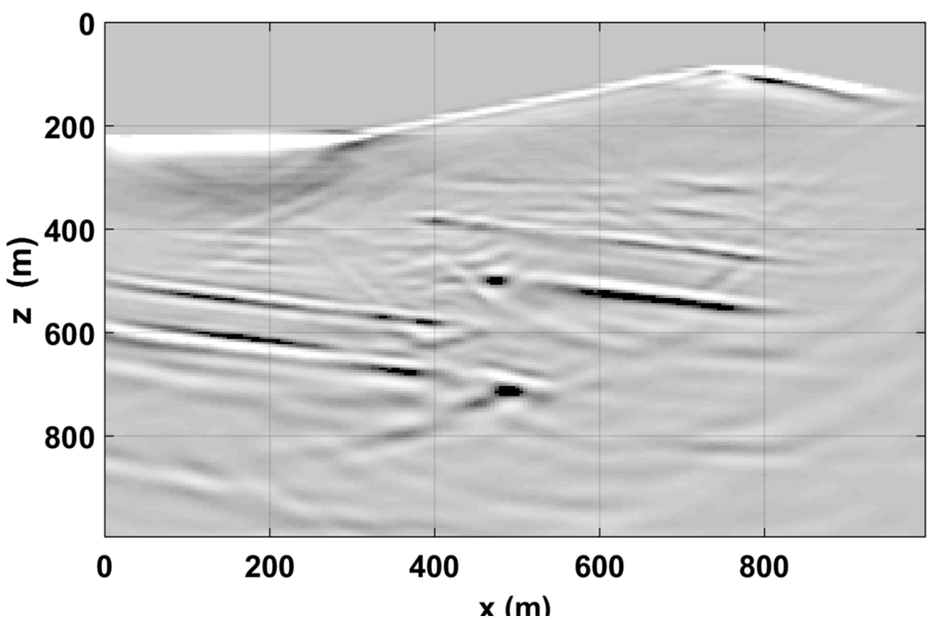

Figure 5.13: PSPI PreSDM for the PS-wave after wave mode separation.

5.3.3 Application of Kirchhoff migration

Figure 5.9 illustrates the arrival times calculated with the eikonal equation method, corresponding to the P-wave (source side) in Figure 5.9a and to the S-wave (receiver side) in Figure 5.9(b). Figures 5.10 and 5.11 illustrate the results of Kirchhoff migration for the PS-wave, without and with wave mode separation. The depth location of the events agree with the original geological model (Figure 5.5). Subtle differences in amplitude can be noticed after wave mode separation . Strong artifacts are present in both cases, which can be attributed partially to the shortcomings of the algorithm when applied to complex areas (Gray et al., 2001). Perhaps the PS waves travelpath can increase this effect.

5.3.4 Application of PSPI migration

Figure 5.12 shows the resulting migrated PS data using the PSPI method without wave mode separation. Figure 5.13 presents the result after wave mode separation. The depths of events also correspond closely to the expected depths in the geological model. However similarity to the Kirchhoff migration in the previous section should be noted; there is just a subtle difference, such that the benefit of wave mode separation is not apparent.

5.4 Discussion

Differences in the results that appear as noise can be attributed to differences between algorithms. Kirchhoff results appear noisier, especially at deeper depths. Differences can also be related to the wave mode, interfering coherent noise results in noisier PS-wave images than PP-wave section.

Real data are affected by many factors and uncertainties not taken into account here, such as attenuation, noise and heterogeneity;, which would require specific consideration. As for future work, the resulting migrated data can be an appropriate subject for amplitude investigations that can provide useful data for AVO of both wave modes.

The wave mode separation appears effective up to a point (Figure 5.8). However, the benefit of wave mode separation is not apparent in the data after PreSDM. The Kirchhoff migration algorithm has well known shortcomings that have been discussed in the literature (e.g. Biondi, 2006; Gray et al., 2001). This result can also be attributed to shortcomings of the mode separation method for such a complex problem. For example, the local Tau-p transform applied for wave mode separation also can introduce boundary artifacts.

5.5 Conclusions

- Both depth migration methods from the topography gave correct reflector depths, and show the right geometry of the geological structure. Artifacts are partially attributable to the migration algorithms.
- The Kirchhoff result is noisier than PSPI, which can be expected by the high frequency approximation in the presence of a complex structure (Gray et al., 2001).
- The differences in amplitude can be related to the migration algorithms, besides the differing PP and PS reflection coefficients.
- The resolution of the PS-wave is better, however it appears noisier.
- Reasonable results of wave mode separation appear in individual shots. However, the migration results are not as rewarding, which can be attributable to attenuated and migration shortcomings and perhaps remaining free surface effects.
- Additional more extended test, such as other migration approaches, can contribute to evaluate the potential of the wave separation method in complex areas.

Chapter 6

Conclusions and future work

6.1 Summary

The following topics have been addressed in this Thesis:

- The near surface S-wave velocity (V_S) model: this model is analyzed using data from an experimental uphole survey (with energy sources inside the borehole), carried out on a site of Colombia. Picking S-wave events directly generated by the sources enabled a reliable NSL velocity model to be obtained; however the very shallow NSL section (less than 15 m depth) produced many interfering events, which makes more difficult to obtain that model. Tomography allowed to obtain a more robust model, that included the surroundings of the borehole. Analogously, S-wave refractions allowed to obtain a V_S model of the NSL for the surface 2-D seismic line. However, in this case it does not appears to be possible to obtain the velocity model of the very shallow NSL, since the surface sampling of the 2-D line is not enough. By the way, the very shallow section velocity is important since it is usually too low, which increases its effect in the delay time anomalies of seismic reflections.

- The generation of S-waves by explosive sources in the uphole and in the 2-D surface line: S-waves generated by the explosive sources were identified in the uphole, which is supported by theoretical models, and was tested with some methods. Analyzing a shot of a standard land surface 2D-3C seismic line at the uphole location, an analogous S-wave event was found, which, besides yielding the S-wave refractions used for the NSL velocity model, suggests the possibility of a much more extended phenomena, the presence of SS-wave reflections in the surface seismic line.

- Receiver statics correction for PS-waves: Two PS-wave statics correction methods currently used were analyzed, and their main shortcomings were identified. These are the requirements of a NSL V_S model in the datum statics method, and the requirement of an identifiable PS reflection event, with its corresponding stacking velocity, in the method termed here common receiver stack statics (CRSS). In addition, the datum statics correction method appears inaccurate, and CRSS too laborious, despite being more reliable. Therefore, a new PS-waves receiver statics correction method is proposed, to overcomes these drawbacks. This method uses common receiver gathers (CRG) to obtain the differential statics delay caused by S-waves in adjacent receivers, and is abbreviated here CRGS for Common Receiver Gather Statics. This method was tested with synthetic and real data, yielding encouraging results. Compared with the CRSS method, CRGS require neither a stacking velocity model, nor a guide horizon, and is automatic. Compared to the datum statics method, the new one does not require an NSL velocity model, and yields a shorter wavelength solution.

- P and S wave mode separation on a sloping surface: A method for wave-mode separation in the presence of topography is proposed. The method takes into account the free-surface response applied to an inclined free surface, with horizontal variations in the properties (or V_P and V_S). To this purpose rotation of the data is required, together with a plane-wave decomposition using a local τ-p transform. Applying this method to a simple slope ray-tracing model and an FD model with a hill confirmed the effectiveness of this approach.

- Pre-Stack Depth Migration of PP and PS waves in the presence of topography: Two methods for preSDM, Kirchhoff and PSPI, were implemented for rough topography. Scalar algorithms used for conventional seismic data served as the basis for this new application. The Kirchhoff method required interval velocity models for both wave modes to generate arrival-time tables to be applied to the data. The PSPI method requires extrapolation in rough terrain (with variations in space) applied to both wavefields (source or P and receiver or S) in the frequency domain. Both methods were tested with synthetic data. Both methods allowed to obtain coherent seismic images of PP and PS-waves, with the correct geometry. However a number of artifacts are present. The scalar approach, and the approximations of the methods, can explain these artifacts. The wave-mode separation done prior to applying these preSDM methods contributes marginally to the result

6.2 Discussion

More extended application of S-waves can provide a source of useful information to seismic technologies. Experiments and theoretical models have shown that this wave mode is more common than usually expected; however extracting it from the raw multicomponent records has proved challenging. This thesis provides some methods and also discusses some ideas for future research that can be rewarding, mainly oriented to land data. However, they are based on a simplified model: an elastic, isotropic, and 2-D medium.

The near-surface has been addressed on a number of points: the velocity models, the differential time delay of reflections (or statics), the rough topography, and the free surface effect. Some of them are general issues of the multicomponent method, and some are specific to complex settings. Solution methods have been proposed, which would be advisable to test more extensively, by application to diverse cases on real and synthetic data. In addition, to obtain better geological information, there are some other topics not included here that deserve study, such as the complex wavefield generated and propagated through the near surface, and the effect of the NSL properties such as viscoelasticity and anisotropy. These topics could even provide useful information about the NSL, applicable to the improvement of reflections from deeper interfaces. They would benefit seismic exploration and, in addition, could also benefit other fields whose focus is the near surface, such as Civil Engineering.

On the other hand, the real subject of seismic exploration is information about the deeper geological formations, their shape and, if possible, their lithological properties. The multicomponent method can provide additional information, but it is currently less extensively applied than it could be. The migration methods proposed in this work can provide additional images, which can be tested with real data. However wave propagation in the land is an elastic phenomenon: P-waves interact with S-waves, and without an elastic approach even the P wave can be unreliable, as shown by Marelli et al. (2012). Hence, research on algorithms for elastics waves imaging is advisable.

There are powerful tools in wave propagation theories and signal processing that can be explored with this purpose. For example, the statics correction method proposed in this Thesis (CRGS) shows that PS-waves are more common than expected, even if they are not easily identified in the data by the naked eye. Besides that, the simple models used for basic processing probably do not contribute too much, since they cannot be used to identify these events. Methods guided by the data, instead of by simplified models, could be rewarding.

In addition, current powerful inversion algorithms, such as the FWI approach, can provide the mean to solve specific issues, such as the generation of velocity models, or the near-surface properties to invert its effect in the data (e.g. Romdhane et al., 2011; Groos et al., 2017).

A drawback for the application of experimental multicomponent methods to varied instances is the requirement for real data examples, preferably in varied environments and with appropriate sampling. These data are not commonly available. Synthetic data (with appropriate algorithms) or physical modeling could provide the required data, in the meanwhile.

6.3 Future work

6.3.1 Topics for research

A number of topics can be addressed as future work, as follows:

- Application of uphole data to obtain the V_S at the NSL, together with other methods such as surface waves or refractions.

- Work on theory and through experiments to analyze the S-waves generated by the explosive sources in boreholes and in 2-D surface lines

- Investigation of S-wave reflections generated by explosive sources in standard multicomponent data (SS-reflections), including their processing (see section 6.3.2).

- Investigation about methods to obtain the NSL elastic parameters, and to filter the events generated at the NSL. FWI appears a promising technique to this purpose.

- Extended testing of the receiver statics correction method to real data in different settings, such as more complex structures.

- Application of the wave mode separation method to real data, and comparison with other separation methods in complex areas.

- Elastic migration methods with topography, RTM and Kirchhoff, and test with real data.

- Work on methods to obtain the velocity model for depth imaging. FWI is a promising approach regarding this issue.

6.3.2 A new processing flow suggested

Taking into account the results of this Thesis, a processing flow for land multicomponent (3-C) data can be suggested for discussion and testing:

1. Wave-mode separation into P and S using the algorithm of Figure 4.8.

2. Processing of the PP-wave using the conventional method (Figure 1.5a).

3. Calculation of the statics correction of PS-wave for the receiver using the algorithm of Figure 3.7.

4. Processing of the PS wave following an algorithm close to the one presented in Figure 1.5b.

5. Calculation of the source statics correction of SS-wave, with a first approximation from the receiver statics of PS-wave, and perhaps using a velocity model obtained from an uphole (analogous to the method of chapter 2). For this purpose, the algorithm of Figure 3.7 can also be explored, using CSG instead of CRG.

6. Processing of the SS wave using a flow close to Figure 1.5a.

After this processing flow, it would be possible to obtain three seismic sections, PP, PS and SS, consequently more complete information useful for seismic exploration from a conventional 3-C seismic survey.

Bibliography

Achenbach, J. D., 1973, Wave propagation in elastic solids: Elsevier Publishers, Amsterdam.

Agudelo, W., Pineda, E., Gomez, R., Guerrero, J., Rojas, N., Stewart, R. R., and Coevering, N. V., 2013, Using converted-wave seismic data for lithology discrimination in a complex fluvial setting: Tenerife oil-field, Middle Magdalena Valley, Colombia: The Leading Edge, **33**, 72–78.

Aki, K., and Richards, P. G., 1980, Quantitative seismology: theory and methods: W. H. Freeman and Company, New York.

Al-Dulaijan, K., and Stewart, R. R., 2010, Using surface wave methods for static corrections: a near surface study at Spring Coulee: 80th Ann. Internat. Mtg., Soc. Expl. Geophys., Expanded Abstracts, 1897–1891.

Al-Saleh, S. M., 2006, Designing explicit wavefield extrapolators for depth migration and migration velocity analysis: Ph.D. thesis, Univ. of Calgary.

Al-Saleh, S. M., Margrave, G. F., and Gray, S. H., 2009, Direct downward continuation from topography using explicit wavefield extrapolation: Geophysics, **74**, S105–S112.

Anno, P. D., 1986, Two critical aspects of shear wave analysis: statics solutions and reflection correlations, *in* Danbom, S. H., and Domenico, S. N., Eds., Shear-wave exploration, Society of Exploration Geophysicists: Geophysical Developments Series, 48–61.

Askari, R., 2013, Surface wave analysis and its application to the calculation of converted wave static corrections: Ph.D. thesis, Univ. of Calgary.

Bale, R. A., 2006, Elastic wave-equation depth migration of seismic data for isotropic and azimuthally anisotropic media: Ph.D. thesis, Univ. of Calgary.

Bancroft, J. C., 2007, A practical understanding of pre- and poststack migrations, Course Notes: Society of Exploration Geophysicists.

Barkved, O., Bartman, B., Compani, B., Gaiser, J., Dok, R. V., Johns, T., Kristiansen, P., Probert, T., and Thompson, M., 2004, The many facets of multicomponent seismic data: Oilfield Review, 42–56.

Behr, J. M., 2005, Multicomponent receivers for P-wave seismic over rough topography: motivation and results, *in* 2005 CSEG National Convention, Memories, 7–10.

Berryhill, J. R., 1979, Wave-equation datuming: Geophysics, **44**, 1329–1344.

Bevc, R. A., 1995, Imaging under rugged topography and complex velocity structure: Ph.D. thesis, Stanford University.

Beylkin, G., 1987, Discrete Radon transform: IEEE Transactions on Acoustic, Speech, and Signal Processing, **ASSP-35**, 162–172.

Biondi, B., 2006, 3D seismic imaging: SEG Investigations in Geophysics No. 14.

Boas, M., 2006, Mathematical methods in the physical sciences: John Wiley & Sons, third edn.

Cary, P. W., 1998, P/S wavefield separation in the presence of statics: CREWES Reseach Report, **10**, 30.1–30.8.

Cary, P. W., 2001, Multicomponent seismic exploration in Canada - one person's perspective: CSEG Recorder, 62–67.

Cary, P. W., and Eaton, D. W., 1993, A simple method for resolving large converted-wave P-SV statics: Geophysics, **58**, 429–433.

Cary, P. W., and Zhang, A., 2011, True-amplitude PS prestack time migration via 5d interpolation, *in* Memories CSEG Convention 2011.

Claerbout, J., 1985, Imaging the Earth's Interior: Penwell Publishing.

Claerbout, J. F., 1971, Toward a unified theory of reflector mapping: Geophysics, **36**, No. 3, 467–481.

Cova, R. J., 2017, Near-surface S-wave traveltime corrections and inversion: a raypath-consistent and interferometric approach: Ph.D. thesis, Univ. of Calgary.

Cox, M., 1998, Static corrections of seismic reflection surveys, Geophysical Reference Series: Society of Exploration Geophysicists, Tulsa, OK, USA.

Dankbaar, J. W. M., 1985, Separation of P- and S-waves: Geophysical Prospecting, **33**, 970–986.

de Meersman, K., and Roizman, M., 2009, Converted wave receiver statics from first break mode conversions, *in* CSPG CSEG CWLS Convention Memories, Calgary 2009.

Deans, S. R., 1983, The Radon Transform and some of its applications: John Wylie and Sons, NY.

Disher, D. A., and Naquin, P. J., 1984, Statistical automatic statics analysis: Geophysics, **35**, 574–585.

Donati, M. S., and Stewart, R. R., 1995, P and S wave separation at a liquid-solid interface, *in* CREWES Research Report, vol. 7, 12.1–12.19.

Dufour, J., Lawton, D., and Gorek, S., 1996, Determination of S-wave static corrections from S-wave refractions on P-S data, *in* 66th Ann. Internat. Mtg., Soc. Expl. Geophys., Expanded Abstracts, 1551–1554.

Ermolaeva, E., and Stewart, R. R., 2017, Elastic wave imaging using the SV-P event: modeling and data processing, *in* 87th Ann. Internat. Mtg., Soc. Expl. Geophys., Expanded Abstracts, 2565–2569.

Etgen, J. T., 1988, Prestacked migration of P and SV-waves, *in* 58th Ann. Internat. Mtg., Soc. Expl. Geophys., Expanded Abstracts, 972–975.

Evans, R., 1984, Effects of the free surface on shear wavetrains: Geophys. J. R. astr. Soc., **76**, 165–172.

Ferguson, R. J., and Margrave, G. F., 2005, Planned seismic imaging using explicit one-way operators: Geophysics, **70**, S101–S109.

Garotta, R., 1999, Shear waves from acquisition to interpretation: Distinguished Instructor Series No. 3, SEG.

Gazdag, J., and Sguazzero, P., 1984a, Migration of seismic data: Proceedings of the IEEE, **10**, 1302–1315.

Gazdag, J., and Sguazzero, P., 1984b, Migration of seismic data by phase shift plus interpolation: Geophysics, **49**, 124–131.

Gray, S. H., Etgen, J., Dellinger, J., and Whitmore, D., 2001, Seismic migration problemas and solutions: Geophysics, **66**, 1622–1640.

Gray, S. H., and Marfurt, K. J., 1995, Migration from topography: improving the near surface image: Canadian Journal of Exploration Geophysics, **31**, 18–24.

Grech, M. G., 2002, Enhanced seismic depth imaging of complex fault-fold structures: Ph.D. thesis, Univ. of Calgary.

Groos, L., Schfer, M., Forbriger, T., and Bohlen, T., 2017, Application of a complete workflow for 2d elastic full-waveform inversion to recorded shallow-seismic Rayleigh waves: Geophysics, **82**, R109–R117.

Guevara, S. E., Margrave, G. F., and Agudelo, W., 2013, Near-surface S-wave velocity from an uphole experiment using explosive sources, *in* 83th Ann. Internat. Mtg., Soc. Expl. Geophys., Expanded Abstracts, 1694–1698.

Guevara, S. E., Margrave, G. F., and Stewart, R. R., 2007, P-wave enhancement in rough terrain using multicomponent seismic data: Catatumbo, Colombia: 2007 CSPG CSEG Convention Memories, 477–481.

Hardage, B. A., and Wagner, D., 2014, Generating direct-S modes with simple, low-cost, widely available seismic sources: Interpretation, **2**, SE1–SE15.

Harrison, M. P., 1992, Processing of P-SV surface-seismic data: anisotropy analysis, dip moveout and migration: Ph.D. thesis, Univ. of Calgary.

Hayashi, K., Burns, D. R., and Toksoz, M. N., 2001, Discontinuous-grid finite-difference seismic modeling including surface topography: Bull. Seism. Soc. of America, **91**, 1750–1764.

Heelan, P., 1953, Radiation from a cylindrical source of finite length: Geophysics, **18**, 685–696.

Hokstad, K., 2000, Multicomponent Kirchhoff migration: Geophysics, **65**, 861–873.

Isaac, J. H., and Margrave, G. F., 2011, The effect of receiver statics on CCP stacks: An example from Spring Coulee, Alberta, *in* CREWES Research Report, vol. 23, 54.1–54.10.

Jolly, R. N., 1956, Investigation of shear-waves: Geophysics, **21**, 905–938.

Kim, D. S., Bang, E. S., and Kim, W. C., 2004, Evaluation of various downhole data reduction methods for obtaining reliable V_S profiles: Geotechnical Testing Journal, **27**, 1–13.

Kjartansson, E., 1979, Constant Q-wave propagation and attenuation: Journal of Geophysical Research, **84**, 4737–4748.

Koefoed, O., 1955, On the effect of Poisson's ratios of rock strata on the reflection coefficients of plane waves: Geophysical Prospecting, **3**, 381–387.

Krebes, E. S., 1989, Seismic theory and methods: Geophysics 551: University of Calgary: course lecture notes.

Krebes, E. S., 2009, Seismic wave propagation: Geophysics 645: University of Calgary: course lecture notes.

Kuo, J. T., and Dai, T. F., 1984, Kirchhoff elastic wave migration for the case of noncoincident source and receiver: Geophysics, **49**, 1223–1238.

Lash, C. C., 1985, Shear waves produced by explosive sources: Geophysics, **50**, 1399–1409.

Lee, M. W., and Balch, A. H., 1982, Theoretical seismic wave radiation from a fluid-filled borehole: Geophysics, **47**, 1308–1314.

Levander, A., 1988, Fourth-order finite-difference P-SV seismograms: Geophysics, **52**, 1425–1436.

Li, X. X., 1997, Residual statics analysis using prestack equivalent offset migration: M.Sc. thesis, Univ. of Calgary.

Li, X. Y., Dai, H., and Mancini, F., 2007, Converted-wave imaging in anisotropic media: theory and case studies: Geophysical Prospecting, **55**, 345–363.

Lines, L. R., and Treitel, S., 1984, Tutorial: A review of least-squares inversion and its application to geophysical problems: Geophysical Prospecting, **32**, 159–186.

Lu, H. X., and Hall, K. W., 2008, Preliminary processing results: Spring Coulee, Alberta: CREWES Research Report, **20**, 10.1–10.15.

Macelwane, J. B., and Sohon, F. W., 1936, Introduction to theoretical seismology: John Wiley and Sons, NY.

Malvern, L. E., 1969, Introduction to the mechanics of a continuous medium: Prentice Hall, Inc.

Marelli, S., Maurer, H., and Manukyan, E., 2012, Validity of the acoustic approximation in full-waveform seismic crosshole tomography: Geophysics, **77**, R129–R139.

Marfurt, K. J., Schneider, R. V., and Mueller, M. C., 1996, Pitfalls of using conventional and discrete Radon transforms on poorly sampled data: Bull. Seism. Soc. of America, **91**, 1750–1764.

Margrave, G. F., 2007, Methods of seismic data processing: University of Calgary: course lecture notes.

Margrave, G. F., 2013, Q tools: Summary of CREWES software for Q modelling and analysis, *in* CREWES Research Report, vol. 25, 56.1–56.22.

Margrave, G. F., and Ferguson, R. J., 1999, Wavefield extrapolation by non-stationary phase shift: Geophysics, **64**, 1067–1078.

Margrave, G. F., Lamoureux, M. P., and Henley, D. C., 2011, Gabor deconvolution: estimating reflectivity by nonstationary deconvolution of seismic data: Geophysics, **76**, W15–W30.

Mason, M. V., 2013, Multicomponent seismic imaging of sand reservoirs: Middle magdalena valley, colombia: M.Sc. thesis, University of Houston.

McMechan, G. A., 1983, $p-x$ imaging by localized slant stack of T-x data: Geophys. J. R. astr. Soc., **72**, 213–221.

McMechan, G. A., and Chen, H. W., 1990, Implicit statics corrections in prestack migration of common-source data: Geophysics, **55**, 757–760.

Meissner, R., 1965, P- and SV- waves from uphole shooting: Geophysical Prospecting, **13**, 433–459.

Milkereit, B., 1987, Decomposition and inversion of seismic data - an instantaeous slowness approach: Geophysical Prospecting, **35**, 875–894.

Miller, G. F., and Pursey, H., 1954, The field and radiation impedance of mechanical radiators on the free surface of a semi-infinite isotropic solid: Proceedings of the Royal Society of London. Series A, Mathematical and Physical Sciences, **223**, 521–541.

Miong, S. K., Stewart, R. R., and Wong, J., 2007, Shallow VSP for near-surface structure and statics, *in* Memories 2007 CSPG CSEG Convention, 340–344.

Mosher, C. C., Keho, T. H., Weglein, A. B., and Foster, D. J., 1996, The impact of migration on AVO: Geophysics, **61**, 1603–1615.

Muskat, M., and Meres, M. W., 1940, Reflection and transmission coefficients for plane waves in elastic media: Geophysics, **5**, 115–148.

O'Doherty, R. F., and Anstey, N. A., 1971, Reflections on amplitudes: Geophysical Prospecting, **19**, 430–458.

Ostrander, W. J., 1984, Plane-wave reflection coefficients for gas sands at nonnormal angles of incidence: Geophysics, **49**, 1637–1648.

Parry, D. G., 1996, A multi-method near-surface geophysical study on the Nose Hill upland: M.Sc. thesis, University of Calgary.

Pelissier, M. A., Hoeber, H., van de Coevering, N., and Jones, I. F., 2007, Classics of elastic wave theory: SEG Geophysics Reprint Series No. 24.

Polškov, M. K., Brodov, L. J., Mironova, L., Michon, D., Garotta, R., Layotte, P. C., and Coppens, F., 1980, Utilisation combinée des ondes longitudinales et transversales en sismique reflexion: Geophysical Prospecting, **28**, 185–207.

Prieux, V., Brossier, R., Operto, S., and Virieux, J., 2013, Multiparameter full waveform inversion of multicomponent ocean-bottom-cable data from the Valhall field. part 2: imaging compressive-wave and shear-wave velocities: Geophysical Journal International, **194**, 1665–1681.

Reshef, M., 1991, Depth migration from irregular surfaces with depth extrapolation methods: Geophysics, **56**, 119–122.

Robinson, E. A., 1982, Spectral approach to geophysical inversion by Lorentz, Fourier and Radon transforms: Proceedings of the IEEE, **70**, 1039–1054.

Robinson, E. A., and Treitel, S., 2000, Geophysical signal analysis: Society of Exploration Geophysics.

Romdhane, A., Grandjean, G., Brossier, R., Rejiba, F., Operto, S., and Virieux, J., 2011, Shallow-structure characterization by 2D elastic full-waveform inversion: Geophysics, **76**, R81–R93.

Ronen, J., and Claerbout, J. F., 1985, Surface-consistent residual statics estimation by stack-power maximization: Geophysics, **50**, 2759–2767.

Salinas, T. G., 1996, The influence of near-surface time anomalies in the imaging process: M.Sc. thesis, Colorado School of Mines.

Schafer, A. W., 1993, Binning, static correction, and interpretation of P-SV surface-seismic data: M.Sc. thesis, University of Calgary.

Schneider, W. A., 1971, Developments in seismic data processing and analysis (1968-1970): Geophysics, **36**, 1043–1073.

Schultz, P. S., 1976, Velociy analysis by wavefront synthesis: Ph.D. thesis, University of Stanford.

Sharpe, J. F., 1942, The production of elastic waves by explosion pressures. II: results of observations near an exploding charge: Geophysics, **7**, 311–321.

Shearer, P. M., 1999, Introduction to seismology: Cambridge University Press.

Sheriff, R. E., 1991, Encyclopedic dictionary of exploration seismology: Society of Exploration Geophysicists.

Sheriff, R. E., and Geldart, L. P., 1995, Exploration seismology: Cambridge University Press.

Shtivelman, V., and Canning, A., 1988, Datum correction by wave-equation extrapolation: Geophysics, **53**, 1311–1322.

Socco, L. V., Foti, S., and Boiero, D., 2010, Surface-wave analysis for building near-surface velocity models: established approaches and new perspectives: Geophysics, **75**, 75A83–75A102.

Stanton, K. A., 2017, Vector interpolation and regularized elastic imaging of multicomponent seismic data: Ph.D. thesis, University of Alberta.

Stewart, R. R., Gaiser, J. E., Brown, R. J., and Lawton, D. C., 2002, Converted-wave seismic exploration: methods: Geophysics, **67**, 1348–1363.

Stewart, R. R., Gaiser, J. E., Brown, R. J., and Lawton, D. C., 2003, Converted-wave seismic exploration: applications: Geophysics, **68**, 40–57.

Stewart, R. R., and Marchisio, G., 1991, Side-scanning seismic: analysis and a physical modeling study, *in* CREWES Research Report, vol. 3, 243–251.

Stümpel, H., Kähler, S., Meissner, R., and Milkereit, B., 1984, The use of seismic shear waves and compressional waves for lithological problems of shallow sediments: Geophysical Prospecting, **32**, 663–675.

Suarez, G., and Stewart, R. R., 2009, Seismic source comparison for compressional and converted-wave generation at Spring Coulee, Alberta, *in* 79th Ann. Internat. Mtg., Soc. Expl. Geophys., Expanded Abstracts, 99–103.

Taner, M. T., Koehler, F., and Alhilali, K. A., 1974, Estimation and correction of near-surface anomalies: Geophysics, **39**, 441–463.

Tessmer, G., and Behle, A., 1988, Common reflection point data-stacking technique for converted waves: Geophysical Prospecting, **36**, 671–688.

Thomsen, L., 1986, Weak elastic anisotropy: Geophysics, **51**, 1954–1966.

Thomsen, L., 1999, Converted-wave reflection seismology over inhomogeneous, anisotropic media: Geophysics, **64**, 678–690.

Treitel, S., Gutowski, P. R., and Wagner, D. E., 1982, Plane-wave decomposition of seismograms: Geophysics, **47**, 1375–1401.

Van der Baan, M., 2006, PP/PS wavefield separation by independent component analysis: Geophys. J. Int., **166**, 339–348.

Wang, W., and McMechan, G. A., 2015, Vector-based elastic reverse time migration: Geophysics, **80**, S245–S258.

Wapenaar, C. P. A., Herrmann, P., Verschuur, D. J., and Berkhout, A. J., 1990, Decomposition of multicomponent seismic data into primary P- and S-wave responses: Geophysical Prospecting, **38**, 633–661.

White, J. E., and Sengbush, R. L., 1963, Shear waves from explosive sources: Geophysics, **28**, 1001–1019.

Wiest, B., and Edelmann, H. A. K., 1984, Static corrections for shear wave sections: Geophysical Prospecting, **32**, 1091–1102.

Wiggins, J. W., 1984, Kirchhoff integral extrapolation and migration of nonplanar data: Geophysics, **49**, 1239–1248.

Wiggins, R. A., Larner, K. L., and Wisecup, R. D., 1976, Residual statics analysis as a general linear inverse problem: Geophysics, **41**, 922–938.

Yan, J., and Sava, P., 2008, Isotropic angle-domain elastic reverse-time migration: Geophysics, **73**, S229–S239.

Yilmaz, O., 2001, Seismic data analysis: processing, inversion and interpretation of seismic data: Society of Exploration Geophysics, Investigations in Geophysics No. 10.

Zuleta-Tobon, L., 2012, Near-surface characterization and Vp/Vs analysis of a shale gas basin: M.Sc. thesis, Univ. of Calgary.

Appendix A

Theoretical background overview

Some basic theoretical principles of elastic wave propagation are presented in the following pages. The purpose is to provide a rapid reference guide to the background ideas, and to the terms used in the main text, from an applied point of view. The bibliography would be a guide for deeper analyses.

A.1 Seismic wave propagation

The theoretical principles of seismic wave propagation are due to some great scientists of the 19th century, including Navier, Cauchy and Poisson (see e.g. Pelissier et al., 2007). Examples of references useful for seismic exploration include the theoretically oriented Achenbach (1973) and Aki and Richards (1980), and the more applied Sheriff and Geldart (1995) and Shearer (1999).

Seismic waves are energy disturbances that propagate through a material medium, locally generating oscillations about the rest location, without permanent effect in the medium properties. A *particle* is defined as an (*infinitesimal* component of a medium that preserves its properties, which allows to apply the methods of *continuum mechanics* (Malvern, 1969).

It is assumed in this work an *elastic* medium, that do not attenuate under propagation, *isotropic*, namely its properties do not change with the direction, and 2-D. Although it is a relatively simple model, it allows quite useful analysis.

An energy perturbation in a material medium generates *displacements* in it, which can change its shape or *strain*, and consequently generates internal *stress*. This energy perturbation propagates through the medium as a seismic wave.

Two properties of the material medium determine the wave behavior: *inertia* or resistance to the change from their rest or movement state, and *elasticity* or resistance to deformation (Achenbach, 1973). These properties are expressed by two physical laws: Newton's Second Law for the inertia, and Hooke's Law for elasticity, which allows to derive the equations that govern seismic wave propagation.

A.1.1 The 1-D wave equation

The simplest 1-D wave equation provides the basic concepts, as shown in the following. The Newton's Second Law, $Force$ $=$*mass* times *acceleration*, in the case of a 1-D displacement of a particle from its equilibrium position reads

$$\frac{\partial \sigma}{\partial x} = \rho \frac{\partial^2 u}{\partial t^2} \quad , \tag{A.1}$$

where x is the spacial coordinate, σ is the unit force or *stress*, ρ is the density and u is the particle displacement from the rest position, and $\frac{\partial^2 u}{\partial t^2}$ is the particle acceleration.

Hooke's Law states the relation between the deformation of the elastic medium and the unit force applied

$$\sigma = E \frac{\partial u}{\partial x} \quad , \tag{A.2}$$

where E is the *elastic constant*, a property of the medium, and $\frac{\partial u}{\partial x}$ is the *strain*, namely the unit deformation in the x direction[1].

Inserting equation (A.2) into (A.1) the 1-D wave equation results:

$$E \frac{\partial^2 u}{\partial x^2} = \rho \frac{\partial^2 u}{\partial t^2} \quad , \tag{A.3}$$

whose solution has the shape

$$u = f(x - c_1 t) \quad , \tag{A.4}$$

where f is a general function.

Some remarks of interest are:

[1]Equations involving specific parameters of a medium are called *Consitutive Equations*.

- If $x - c_1 t$ is constant then it defines a *wavefront*, such that the displacement u is in phase for a x value.

- From the solution of equation A.4, replacing in equation A.3, ${c_1}^2 = E/\rho$, where c_1 is the *velocity*: for a *wavefront*, assuming that $x = 0$ at $t = 0$, then for any x,

$$x - c_1 t = 0 \quad \text{, therefore} \quad c_1 = \frac{x}{t} = v \quad ,$$

  namely the propagation velocity.

- Replacing the wave propagation velocity v, the standard representation of the wave equation can be obtained:

$$v^2 \frac{\partial^2 u}{\partial x^2} = \frac{\partial^2 u}{\partial t^2}. \tag{A.5}$$

A.1.2 Elastic waves in a 3-D isotropic medium

Strain and *stress* in the case of a multidimensional medium require subscripts for the space dimensions. In Cartesian coordinates the 3 dimensions x, y and z, are represented by x_1, x_2 and x_3. The indices are represented in general by letters, i, j, k or l. This greatly reduces writing. The stress is symbolized by σ_{ij}, where i identifies the stress direction and j the normal to the face where it acts (Krebes, 1989). Thereby the *strain* in the direction i on the face normal to x_j is defined as

$$\epsilon_{ij} = \frac{\partial u_i}{\partial x_j} \quad . \tag{A.6}$$

Thus, the general form of Hooke's Law reads:

$$\sigma_{ij} = \sum_{k=1}^{3} \sum_{l=1}^{3} c_{ijkl} \epsilon_{kl} \quad , \tag{A.7}$$

where all the possible 3-D stresses and strains are represented, and c_{ijkl} represents all the elastic constants relating these stresses and strains.

It has been shown that the maximum possible *anisotropy* (different elastic properties in any direction), requires 21 elastic constants (e.g. Krebes, 1989; Aki and Richards, 1980). The isotropic medium, which is addressed in this thesis, requires only two independent elastic constants, which are most commonly represented by *Lame's* parameters, λ and μ (see e.g. Macelwane and Sohon, 1936).

Setting the equilibrium equations for a particle, and applying the Second Newton's Law, the *equation of motion* that governs wave propagation in a 3-D isotropic elastic medium is

$$\rho\frac{\partial^2 u_i}{\partial t^2} = \frac{\partial \sigma_{ii}}{\partial x_i} + \frac{\partial \sigma_{ij}}{\partial x_j} + \frac{\partial \sigma_{ik}}{\partial x_k} \quad , \tag{A.8}$$

and the isotropic *constitutive equations* result from Hooke's Law

$$\sigma_{ii} = (\lambda + 2\mu)\frac{\partial u_i}{\partial x_i} + \lambda\left(\frac{\partial u_j}{\partial x_j} + \frac{\partial u_k}{\partial x_k}\right) \quad , \tag{A.9}$$

and

$$\sigma_{ij} = \mu\left(\frac{\partial u_j}{\partial x_i} + \frac{\partial u_i}{\partial x_j}\right) \quad . \tag{A.10}$$

Replacing A.9 and A.10 into A.8 it results:

$$\begin{aligned}\rho\frac{\partial^2 u_i}{\partial t^2} \quad = \quad & \frac{\partial}{\partial x_i}\left[\lambda\left(\frac{\partial u_i}{\partial x_i} + \frac{\partial u_j}{\partial x_j} + \frac{\partial u_k}{\partial x_k}\right) + 2\mu\frac{\partial u_i}{\partial x_i}\right] + \\ & \frac{\partial}{\partial x_j}\left[\mu\left(\frac{\partial u_i}{\partial x_j} + \frac{\partial u_j}{\partial x_i}\right)\right] + \frac{\partial}{\partial x_k}\left[\mu\left(\frac{\partial u_i}{\partial x_k} + \frac{\partial u_k}{\partial x_i}\right)\right] \quad .\end{aligned} \tag{A.11}$$

The *divergence* θ, which describes the volume change (see e.g. Boas, 2006), is defined as

$$\theta = \left(\frac{\partial u_1}{\partial x_1} + \frac{\partial u_2}{\partial x_2} + \frac{\partial u_3}{\partial x_3}\right) \quad , \tag{A.12}$$

and the *Laplacian operator* ∇^2 is defined as

$$\nabla^2 = \frac{\partial^2}{\partial x_1^2} + \frac{\partial^2}{\partial x_2^2} + \frac{\partial^2}{\partial x_3^2} \quad . \tag{A.13}$$

Therefore, after rearranging and factoring equation A.11, we obtain

$$\rho\frac{\partial^2 u_i}{\partial t^2} = (\lambda + \mu)\frac{\partial \theta}{\partial x_i} + \mu\nabla^2 u_i \quad , \tag{A.14}$$

which is valid for each one of the three components.

These equations describe the complete elastic wave field 3-D for a homogeneous isotropic medium. It is possible to identify two coupled wave modes from them, by applying two vector calculus operations: the *divergence* and the *curl*. The divergence states the volume change of the displacement, and the curl states the rotation of the displacement. The resulting two *elastic* wave modes are P or *compressional* (or primary) and S or *shear* (or secondary), which are defined as follows:

1) The P-wave equation is:

$$(\lambda + 2\mu)\nabla^2\theta = \rho\frac{\partial^2\theta}{\partial t^2} \quad , \tag{A.15}$$

and the P wave velocity (analogous to the 1-D case illustrated in Section A.1.1) is expressed by:

$$V_P = \sqrt{\frac{\lambda + 2\mu}{\rho}} \quad . \tag{A.16}$$

2) The S wave equation is

$$\mu\nabla^2\vec{\omega} = \rho\frac{\partial^2\vec{\omega}}{\partial t^2} \quad , \tag{A.17}$$

where $\vec{\omega}$ is the *rotational* vector, whose component is

$$\omega_i = \left(\frac{\partial u_j}{\partial x_k} - \frac{\partial u_k}{\partial x_j}\right)\hat{i} \quad , \tag{A.18}$$

and the S wave velocity is

$$V_S = \sqrt{\frac{\mu}{\rho}} \quad . \tag{A.19}$$

A.2 Seismic waves in the frequency domain

The wave propagation solutions can be decomposed into sinusoidal functions, also called *harmonic functions*. An harmonic function that represents a solution of a 1-D wave equation is:

$$u = U_0 \cos 2\pi f(x/v \pm t) \tag{A.20}$$

where x is the space location, t is the time, f is the *time frequency*, namely the number of cycles by a time unit, measured in *cycles per second* (*Hertz*), U_0 is the *amplitude*, namely the maximum displacement, and v is the propagation velocity. This is called a *monochromatic wave* by analogy with an electromagnetic wave, in which one frequency corresponds to a single color.

Other characteristics of the harmonic waves are the period T or time of cycle, defined by

$$T = \frac{1}{f},$$

and λ, the wavelength or length of a cycle, defined by

$$\lambda = vT;$$

The wavelength relates velocity and frequency according to

$$\lambda = v/f \quad . \tag{A.21}$$

Frequency can be represented in radians per second by ω, according to:

$$\omega = 2\pi f = \frac{2\pi}{T} \quad . \tag{A.22}$$

The *spacial frequency* k, is defined as the number of cycles per space unit,

$$k = \frac{1}{\lambda} \quad .$$

In the x direction, it is k_x, measured in radians per meter, and defined as

$$k_x = \frac{2\pi f}{V}.$$

A monochromatic wave can be expressed as a complex exponential function according to Euler's Formula (see e.g. Boas, 2006), as

$$u = U_0 \exp i(k_x x - \omega t) \quad , \quad \text{where} \quad i = \sqrt{-1} \quad . \tag{A.23}$$

In 3-D becomes

$$u = U_0 \exp i(\vec{k} \cdot \vec{x} - \omega t), \tag{A.24}$$

where

$$\vec{k} \cdot \vec{x} = k_x x + k_y y + k_z z.$$

A.2.1 The Fourier analysis

Real seismic disturbances can be decomposed as monocromatic harmonic waves (e.g. Aki and Richards, 1980; Sheriff and Geldart, 1995). This decomposition is carried out using the Fourier transform of FT (see e.g. Boas, 2006) which in time is defined as:

$$FT(\varphi(t)) = \tilde{\varphi}(\omega) = \int_{-\infty}^{\infty} \varphi(t) \exp(-i\omega t)\, \mathrm{d}t. \tag{A.25}$$

The inverse Fourier transform is:

$$FT^{-1}(\tilde{\varphi}(\omega)) = \varphi(t) = \frac{1}{2\pi} \int_{-\infty}^{\infty} \tilde{\varphi}(\omega) \exp(i\omega t)\, \mathrm{d}\omega \quad ; \tag{A.26}$$

the variables t and ω are known as duals of each other.

The FT in a general variable α can be represented as follows:

$$\tilde{\psi}(k_\alpha) = FT_\alpha(\psi(\alpha)) \qquad \text{or} \qquad \psi(\alpha) \xleftrightarrow{FT} \tilde{\psi}(k_\alpha)$$

where k_α is the dual of α.

A couple of relevant properties of the Fourier Transform are the *derivative theorem*:

$$\frac{\partial \psi(\alpha)}{\partial \alpha} \xleftrightarrow{FT} ik_\alpha \tilde{\psi}(k_\alpha) \quad , \tag{A.27}$$

and the *shift theorem*:

$$\psi(\alpha + \Delta\alpha) \xleftrightarrow{FT} e^{ik_\alpha \Delta\alpha} \tilde{\psi}(k_\alpha) \quad . \tag{A.28}$$

Since the seismic wave is a function of time and space, an usual 2-D Fourier transform is

$$FT(\varphi(t,x)) = \tilde{\tilde{\varphi}}(\omega, k_x) = \int_{-\infty}^{\infty} \int_{-\infty}^{\infty} \varphi(t,x) \exp(i(\omega t - k_x x))\, \mathrm{d}t\, \mathrm{d}x \tag{A.29}$$

A.2.2 The scalar 2-D wave equation

The scalar wave equation is the basis of most seismic processing technology. It corresponds to the acoustic wave equation, that governs wave propagation in a medium without shear resistance

$$\nabla^2\psi = \frac{1}{v^2}\frac{\partial^2\psi}{\partial t^2} \quad , \tag{A.30}$$

where v is the propagation velocity. In 2-D this equation reads

$$\left(\frac{\partial^2}{\partial x^2} + \frac{\partial^2}{\partial z^2}\right)\psi = \frac{1}{v^2}\frac{\partial^2\psi}{\partial t^2} \quad . \tag{A.31}$$

Applying the property of equation A.27 to the Fourier transform in the time domain,

$$\tilde{\psi} = FT_t(\psi) \quad ,$$

we obtain the relation:

$$\left(\frac{\partial^2}{\partial x^2} + \frac{\partial^2}{\partial z^2}\right)\tilde{\psi} + \frac{1}{v^2}\omega^2\tilde{\psi} = 0 \quad , \tag{A.32}$$

which is known as the Helmholtz equation.

Applying the Fourier transform in the x-space domain

$$\tilde{\tilde{\psi}} = FT_x(\tilde{\psi}) \quad ,$$

another useful representation results

$$\left(\frac{\partial^2}{\partial z^2} + \frac{1}{v^2}\omega^2 - k_x^2\right)\tilde{\tilde{\psi}} = 0 \quad ; \tag{A.33}$$

following Bale (2006), equation A.33 can be factorized as

$$\left(\frac{\partial}{\partial z} + ik_z\right)\left(\frac{\partial}{\partial z} - ik_z\right)\tilde{\tilde{\psi}} = 0 \quad , \tag{A.34}$$

where k_z, is the wave number in the vertical direction, defined by:

$$k_z^2 = \frac{\omega^2}{v^2} - k_x^2 \tag{A.35}$$

Equation A.34 can be separated into two one-way equations:

$$\left(\frac{\partial}{\partial z} + ik_z\right)\tilde{\tilde{\psi}} = 0 \tag{A.36}$$

and

$$\left(\frac{\partial}{\partial z} - ik_z\right)\tilde{\tilde{\psi}} = 0 \quad , \tag{A.37}$$

where A.36 corresponds to up-going waves, and A.37 to down-going waves.

A.3 Extending the media models: anisotropy and anelasticity

In the previous analysis, an isotropic elastic medium was assumed. However, it is a first approach, since the real earth properties can change with direction (*anisotropy*), and there is energy loss through their propagation (*anelasticity*).

The generalized Hooke's Law allows defining variation of the elastic properties in any direction, according to equation A.7, where the index correspond to any of the three coordinate axes. In the extreme anisotropic case, there are 21 independent elastic constants (e.g. Krebes, 1989; Aki and Richards, 1980).

Two anisotropic models defined by five elastic constants, have achieved practical application in the seismic method of exploration, since they are analogous to practical situations: *polar anisotropy*, (also called VTI or *vertical transverse isotropy*), analogous to horizontal strata in geology, and *azimuthal anisotropy* (called HTI or *horizontal transverse isotropy*), analogous to vertical fractures, common in geological formations.

A simplified approach, the *weak anisotropy* model, was developed by Thomsen (1986), who found that the anisotropy quantified as the difference in wave velocity with direction, is less than 20 %, which corresponds to much of the practical cases of interest. In addition to the velocities V_P and V_S, three parameters have been introduced, known as the *Thomsen's constants* (Thomsen, 1986), ε_t, γ_t and δ_t, defined as

$$\varepsilon_t = \frac{V_P(\pi/2) - V_{P0}}{V_{P0}} \quad ,$$

$$\gamma_t = \frac{V_{SH}(\pi/2) - V_{S0}}{V_{S0}} \quad ,$$

and

$$\delta_t = 4\left[\frac{V_P(\pi/4)}{V_{P0}} - 1\right] - \left[\frac{V_P(\pi/2)}{V_{P0}} - 1\right] \quad ,$$

where $V_\varphi(\alpha)$ is the velocity V_φ in the direction of the angle α.

Attenuation of seismic waves caused by energy loss is apparent in real data, however, it is not considered in the elastic model, and is usually neglected in practical applications. The parameter that characterizes seismic attenuation is known as Q, or *quality factor*, a property of the medium defined as the ratio between the energy stored and the energy lost. Among the anelasticity theories, a linear, frequency independent viscoelastic model, known as the *constant Q model*, has become more usual in practical applications (Margrave, 2013). It implies dispersion, and phase change of the seismic perturbation, as progressing in time (Kjartansson, 1979).

A.4 Derivation of the NMO equation

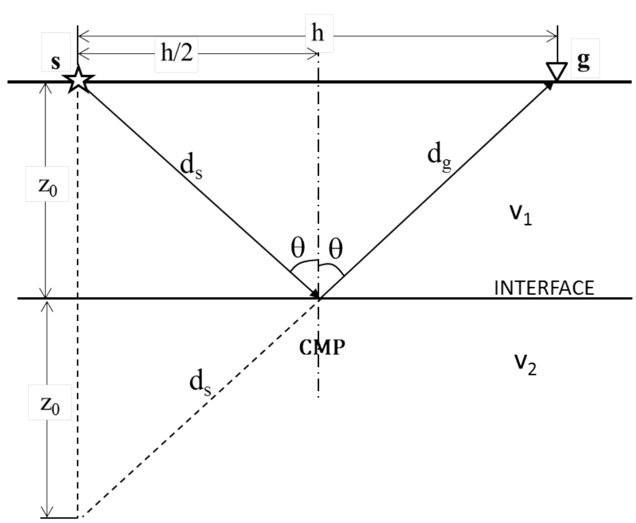

Figure A.1: Ray diagram to derivate the NMO equation.

The Normal Moveout (NMO) is the delay of a seismic reflection caused by the distance between source and receiver or *offset*, h. The corresponding equation can be derived assuming a flat horizontal reflecting surface and a constant velocity layer. It is illustrated in Figure A.1. The wave path for a PP reflection from source to receiver is indicated by two arrows with length d_s and d_g, and the same angles of incidence and reflection θ, according to Snell's Law. The dashed lines establish an auxiliary construct to apply the Pythagoras' Theorem, as follows

$$(d_s + d_g)^2 = (2z_0)^2 + h^2 \quad . \tag{A.38}$$

We have

$$t(h) = (d_s + d_g)/v_1 \quad ,$$

or

$$d_s + d_g = t(h)v_1 \quad .$$

Then, from Equation A.38

$$(t(h)v_1)^2 = (2z_0)^2 + h^2 \quad ,$$

and solving for t

$$t(h)^2 = \left(\frac{2z_0}{v_1}\right)^2 + \left(\frac{h}{v_1}\right)^2 \quad . \tag{A.39}$$

The zero-offset two way travel time, t_0, is defined as

$$t_0 = \frac{2z_0}{v_1} \quad ,$$

then from Equation A.39

$$t(h)^2 = t_0^2 + \left(\frac{h}{v_1}\right)^2 \quad . \tag{A.40}$$

Appendix B

The radiation pattern of an energy source inside a cylindrical borehole

Some authors have published theoretical analyses of seismic wave generation in boreholes. Heelan (1953) developed the equations for elastic waves generated at a cylindrical empty borehole. Lee and Balch (1982) derived the equations for a fluidfilled cylindrical borehole in an elastic isotropic homogeneous medium. The following summarizes this theoretical model.

Taking into account the problem symmetry, cylindrical coordinates were used for the derivation, with vertical axis z, angle θ on the horizontal plane, and radius r from the z axis. The borehole model is presented in Figure B (from Lee and Balch, 1982), with the vertical axis at z, and diameter a, and filled with a fluid with P-wave velocity V_{P_1} and density ρ_1. The source is a function of time $W(t)$ (a wavelet), with a volume displacement ΔV_0. The borehole is surrounded by an elastic medium, whose properties are the P-wave velocity V_{P_2}, the S-wave velocity V_{S_2}, and the density ρ_2.

After this model, the corresponding equations are derived using Bessel functions, appropriate to solve differential equations with cylindrical symmetry. The boundary conditions at $r = a$ to be satisfied by stresses and displacements in this problem are:

$$(\sigma_{rz})_1 = (\sigma_{rz})_2 = 0$$

$$(u_r)_1 = (u_r)_2$$

$$(\sigma_{rr})_1 = (\sigma_{rr})_2 \, .$$

The resultant displacements are expressed in polar coordinates for convenience, as a function of the distance R to the origin, and the angle to the borehole axis, ϕ. Then when a volume displacement source is assumed, the particle displacements u_R (radial or P) and u_ϕ

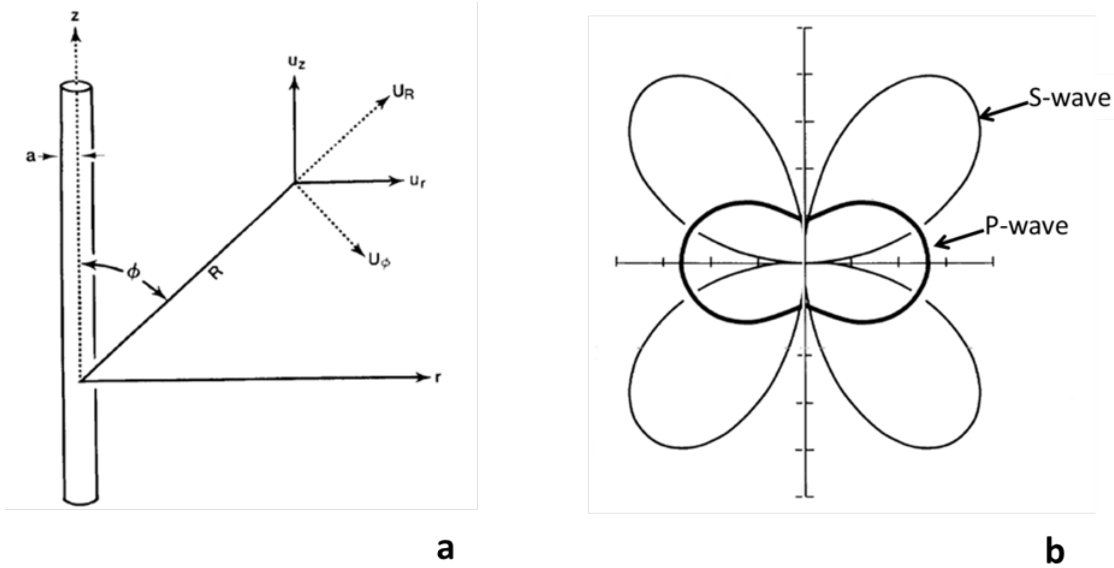

Figure B.1: Model of explosive source inside a filled borehole, according to Lee and Balch (1982). (a) The model geometry. (b) An example of the radiation pattern of the source (from Lee and Balch, 1982).

(tangential, S, or shear) in the solid are given by

$$u_R = \frac{\rho_1 \Delta V_0 \left(1 - 2{V_{S_2}}^2 \cos^2\phi / {V_{P_2}}^2\right) \dot{W}(t - R/V_{P_2})}{4\pi\rho_2 \left(\rho_1/\rho_2 + (V_{S_2}/V_{P_1})^2 - {V_{S_2}}^2 \cos^2\phi/{V_{P_2}}^2\right) V_{P_2} R} \quad , \tag{B.1}$$

$$u_\phi = \frac{\rho_1 \Delta V_0 \sin\phi \cos\phi \dot{W}\left(t - R/V_{S_2}\right)}{2\pi\rho_2 \left(\rho_1/\rho_2 + (V_{S_2}/V_{P_1})^2 - \cos^2\phi\right) V_{S_2} R} \quad , \tag{B.2}$$

where subscript 1 stands for inside the borehole (fluid medium) and subscript 2 stands for outside the borehole (elastic medium). The resulting radiation pattern is illustrated in Figure B(b). Notice the high energy content of the S-wave.

Appendix C

Free surface response in the presence of Topography

C.1 The free-surface effect

The reflection data recorded at the land surface does not correspond to the body wave propagated in the medium, but rather to the image on the vertical and horizontal components of the result of the interaction of reflected waves arriving from depth with the free surface. Reflections and wave mode conversions are generated at the free surface. This property is known as the *free-surface effect*. The free-surface effect depends on the angle of incidence and the elastic properties of the near-surface. Studies about it have been published, frequently related to earthquake seismology (e.g. Meissner, 1965; Evans, 1984).

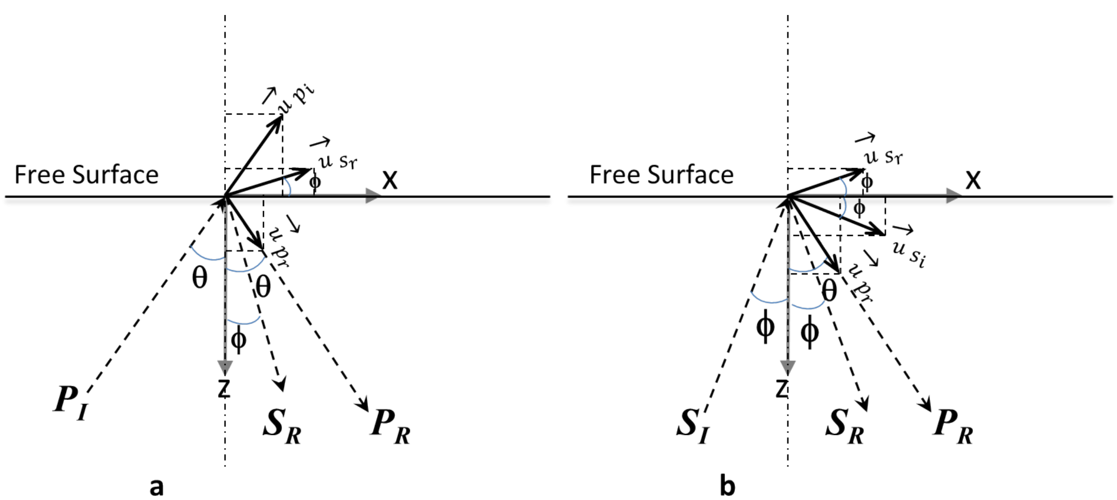

Figure C.1: Free surface effect: decomposition of P and S waves arriving to the surface. (a) P-wave, (b) S wave. Coordinate axes are x increasing to the right and z increasing downward. P_I corresponds to the incident P-wave, S_I to the incident S-wave, P_R to the reflected P-wave, and S_R to the reflected S-wave.

Figure C.1 shows the relationship between incident P-wave (Figure C.1a) and S-wave

(Figure C.1b) and the corresponding reflections at the free surface. At the free surface, the stresses must sum to null. The stresses are related to the displacements by the elastic wave propagation equations. Hence the displacements in the vertical (z) and horizontal (x) directions depend on the stresses equilibrium equations. Additionally, the displacements depend on the angles of incidence and the velocities of the media. An isotropic 2-D medium is assumed. For P-wave incidence, the stress equilibrium equations are:

$$\sum \sigma_{zz} = \sigma_{zz}^{P_i} + \sigma_{zz}^{S_r} + \sigma_{zz}^{P_r} = 0, \tag{C.1a}$$

$$\sum \sigma_{xz} = \sigma_{xz}^{P_i} + \sigma_{xz}^{S_r} + \sigma_{xz}^{P_r} = 0. \tag{C.1b}$$

For the S-wave incidence these equations are

$$\sum \sigma_{zz} = \sigma_{zz}^{S_i} + \sigma_{zz}^{S_r} + \sigma_{zz}^{P_r} = 0, \tag{C.2a}$$

$$\sum \sigma_{xz} = \sigma_{xz}^{S_i} + \sigma_{xz}^{S_r} + \sigma_{xz}^{P_r} = 0. \tag{C.2b}$$

The stresses for an isotropic medium, as shown in appendix A (equations **??** and **??**), are in 2-D

$$\sigma_{zz} = 2\mu\frac{\partial u_z}{\partial z} + \lambda\left(\frac{\partial u_z}{\partial z} + \frac{\partial u_x}{\partial x}\right) \tag{C.3a}$$

$$\sigma_{xz} = \mu\left(\frac{\partial u_z}{\partial x} + \frac{\partial u_x}{\partial z}\right) \tag{C.3b}$$

Let's assume a monochromatic plane wave propagation:

$$\vec{u} = U \exp\left(i\omega\left(\frac{\vec{n}}{v}\cdot\vec{x} - t\right)\right)\vec{d} \tag{C.4}$$

where U is the amplitude, $\vec{n} = [n_x, n_z]$ the ray direction vector, v the wave velocity, $\vec{x} = [x, z]$ the space coordinate vector, and $\vec{d} = [d_x, d_z]$ the polarization vector.

This plane wave can be decomposed into equations C.3 to solve equations C.1 and C.2. The ray direction and polarization vectors for incident and reflected waves are in Table C.1.

Seismic event	$\vec{d}$		$\vec{n}$	
	d_x	d_z	n_x	n_z
P_I	$\sin\theta$	-$\cos\theta$	$\sin\theta$	-$\cos\theta$
P_R	$\sin\theta$	$\cos\theta$	$\sin\theta$	$\cos\theta$
S_I	$\cos\phi$	$\sin\phi$	$\sin\phi$	-$\cos\phi$
S_R	$\cos\phi$	-$\sin\phi$	$\sin\phi$	$\cos\phi$

Table C.1: Propagation direction $\vec{n}$ and polarization angles $\vec{d}$ for P- and S-wave incident to the free surface.

The derivatives in equation C.3, using C.4, are

$$\frac{\partial u_x}{\partial x} = \frac{n_x}{v} U \exp\left(i\omega\left(\frac{\vec{n}}{v}\cdot\vec{x} - t\right)\right) d_x \quad , \qquad \frac{\partial u_x}{\partial z} = \frac{n_z}{v} U \exp\left(i\omega\left(\frac{\vec{n}}{v}\cdot\vec{x} - t\right)\right) d_x \quad ,$$

$$\frac{\partial u_z}{\partial z} = \frac{n_z}{v} U \exp\left(i\omega\left(\frac{\vec{n}}{v}\cdot\vec{x} - t\right)\right) d_z \quad , \text{and} \qquad \frac{\partial u_z}{\partial x} = \frac{n_x}{v} U \exp\left(i\omega\left(\frac{\vec{n}}{v}\cdot\vec{x} - t\right)\right) d_z \quad ,$$

which, after simplifying, become:

$$\frac{\partial u_x}{\partial x} = \frac{U}{v} n_x d_x \quad , \quad \frac{\partial u_x}{\partial z} = \frac{U}{v} n_z d_x \quad , \quad \frac{\partial u_z}{\partial z} = \frac{U}{v} n_z d_z \quad \text{and} \quad \frac{\partial u_z}{\partial x} = \frac{U}{v} n_x d_z \quad .$$

Therefore equations C.3, after replacing and simplifying (Krebes, 2009), become:

$$\sigma_{zz} = \frac{U}{v}\left(2\mu(n_z d_z) + \lambda\left(n_z d_z + n_x d_x\right)\right) \tag{C.5a}$$

$$\sigma_{xz} = \frac{U}{v}\mu\left(n_x d_z + n_z d_x\right) \tag{C.5b}$$

From these relations and the incidence and polarization angles (table C.1), the stresses for each mode can be defined. Thereby the normal stresses σ_{zz} are:

$$\sigma_{zz}^{P_i} = \frac{U_{P_i}}{V_P}\left(2\mu\cos^2\theta + \lambda\right) \tag{C.6a}$$

$$\sigma_{zz}^{S_i} = \frac{U_{S_i}}{V_S}\left(2\mu\cos\phi\sin\phi\right) \tag{C.6b}$$

$$\sigma_{zz}^{P_r} = \frac{U_{P_r}}{V_P}\left(2\mu\cos^2\theta + \lambda\right) \tag{C.6c}$$

$$\sigma_{zz}^{S_r} = \frac{U_{S_r}}{V_S}\left(-2\mu\cos\phi\sin\phi\right) \tag{C.6d}$$

and the shear stresses σ_{xz} are

$$\sigma_{xz}^{P_i} = \frac{U_{P_i}}{V_P}\mu\left(-2\sin\theta\cos\theta\right) \tag{C.7a}$$

$$\sigma_{xz}^{S_i} = \frac{U_{S_i}}{V_S}\mu\left(1-2\cos^2\phi\right) \tag{C.7b}$$

$$\sigma_{xz}^{P_r} = \frac{U_{P_r}}{V_P}\mu\left(2\sin\theta\cos\theta\right) \tag{C.7c}$$

$$\sigma_{xz}^{S_r} = \frac{U_{S_r}}{V_S}\mu\left(2\cos^2\phi-1\right) \tag{C.7d}$$

where the P and S superindex correspond to the wave mode, and in turn their subindex i and r correspond to incident and reflected.

Using equations C.6 and C.7, the stress equilibrium equations (C.1 and C.2) can be expressed as a function of the angles and elastic properties. Hence for incident P_i, and equations C.1:

$$\frac{U_{P_i}}{V_P}\left(2\mu\cos\theta^2+\lambda\right)+\frac{U_{S_r}}{V_S}\left(-2\mu\cos\phi\sin\phi\right)+\frac{U_{P_r}}{V_P}\left(2\mu\cos^2\theta+\lambda\right)=0 \tag{C.8a}$$

$$\frac{U_{P_i}}{V_P}\mu\left(-2\sin\theta\cos\theta\right)+\frac{U_{S_r}}{V_S}\mu\left(2\cos^2\phi-1\right)+\frac{U_{P_r}}{V_P}\mu\left(2\sin\theta\cos\theta\right)=0 \tag{C.8b}$$

For incident S_i, and equations C.2:

$$\frac{U_{S_i}}{V_S}\left(2\mu\cos\phi\sin\phi\right)+\frac{U_{S_r}}{V_S}\left(-2\mu\cos\phi\sin\phi\right)+\frac{U_{P_r}}{V_P}\left(2\mu\cos^2\theta+\lambda\right)=0 \tag{C.9a}$$

$$\frac{U_{S_i}}{V_S}\mu\left(1-2\cos^2\phi\right)+\frac{U_{S_r}}{V_S}\mu\left(2\cos^2\phi-1\right)+\frac{U_{P_r}}{V_P}\mu\left(2\sin\theta\cos\theta\right)=0 \tag{C.9b}$$

P-wave incidence: the resulting strains in x and z-directions for P-wave incidence (see Figure C.1a) are:

$$u_P^z = U_{P_i}(-\cos\theta)+U_{P_r}\cos\theta+U_{S_r}(-\sin\phi) \tag{C.10a}$$

$$u_P^x = U_{P_i}\sin\theta+U_{P_r}\sin\theta+U_{S_r}\cos\phi \tag{C.10b}$$

The unit displacement in x and z can be obtained dividing by the incident wave amplitude.

Dividing equations C.10 by U_{P_i}:

$$\frac{u^z}{U_{P_i}} = (-\cos\theta) + \frac{U_{P_r}}{U_{P_i}}\cos\theta + \frac{U_{S_r}}{U_{P_i}}(-\sin\phi) \tag{C.11a}$$

$$\frac{u^x}{U_{P_i}} = \sin\theta + \frac{U_{P_r}}{U_{P_i}}\sin\theta + \frac{U_{S_r}}{U_{P_i}}\cos\phi \tag{C.11b}$$

Dividing stress equations C.8 by U_{P_i}:

$$\frac{1}{V_P}\left(1 + \frac{U_{P_r}}{U_{P_i}}\right)\left(2\mu\cos^2\theta + \lambda\right) + \frac{2\mu}{V_S}\frac{U_{S_r}}{U_{P_i}}\left(\cos\phi\sin\phi\right) = 0 \tag{C.12a}$$

$$\left(-1 + \frac{U_{P_r}}{U_{P_i}}\right)\left(2\sin\theta\cos\theta\right)\frac{\mu}{V_P} + \frac{\mu}{V_S}\frac{U_{S_r}}{U_{P_i}}\left(1 - 2\cos^2\phi\right) = 0 \tag{C.12b}$$

After solving for U_{P_r}/U_{P_i} from equation C.12a, replacing in equation C.8b and some algebra, the unit reflected S-wave amplitude,

$$\frac{U_{S_r}}{U_{P_i}} = \frac{V_S}{V_P}\frac{4\left(\sin\theta\cos\theta\right)\left(2\mu\cos^2\theta + \lambda\right)}{4\mu\left(\cos\phi\sin\phi\sin\theta\cos\theta\right) - \left(2\mu\cos^2\theta + \lambda\right)\left(1 - 2\cos^2\phi\right)} \quad . \tag{C.13}$$

Analogously, it is possible to obtain the unit reflected P-wave amplitude:

$$\frac{U_{P_r}}{U_{P_i}} = \frac{4\mu\left(\cos\phi\sin\phi\right)\left(\sin\theta\cos\theta\right) - \left(2\mu\cos^2\theta + \lambda\right)\left(2\cos^2\phi - 1\right)}{4\mu\left(\cos\phi\sin\phi\right)\left(\sin\theta\cos\theta\right) - \left(2\mu\cos^2\theta + \lambda\right)\left(1 - 2\cos^2\phi\right)} \quad . \tag{C.14}$$

Replacing C.13 and C.14 in C.11a and simplifying:

$$\frac{u^z}{U_{P_i}} = \frac{\left(2\mu\cos^2\theta + \lambda\right)4\left[-2\cos\theta\left(2\cos^2\phi - 1\right) + 4\sin\phi V_S/V_P\sin\theta\cos\theta\right]}{4\mu\left(\cos\phi\sin\phi\sin\theta\cos\theta\right) + \left(2\mu\cos^2\theta + \lambda\right)\left(2\cos^2\phi - 1\right)} = R_S^z \quad , \tag{C.15}$$

and replacing C.13 and C.14 in C.11b and simplifying:

$$\frac{u^x}{U_{P_i}} = \frac{4\sin\theta\cos\theta\cos\phi\left[2\mu\sin\theta\sin\phi + V_S/V_P\left(2\mu\cos^2\theta + \lambda\right)\right]}{4\mu\left(\cos\phi\sin\phi\sin\theta\cos\theta\right) + \left(2\mu\cos^2\theta + \lambda\right)\left(2\cos^2\phi - 1\right)} = R_S^z \quad . \tag{C.16}$$

Equations C.15 and C.16 correspond to the free surface coefficients for the P-wave incidence.

S**-wave incidence:** For the incident S-wave the vertical (u^z) and horizontal (u^x) displacements are:

$$u_S^z = U_{S_i}(\sin\phi) + U_{P_r}\cos\theta + U_{S_r}(-\sin\phi) \quad , \tag{C.17a}$$

$$u_S^x = U_{S_i}\cos\phi + U_{P_r}\cos\theta + U_{S_r}\cos\phi \quad , \tag{C.17b}$$

which can be expressed as the unit displacement in x and z dividing by the incident wave amplitude U_{S_i}:

$$\frac{u^z}{U_{S_i}} = (\sin\phi) + \frac{U_{P_r}}{U_{S_i}}\cos\theta + \frac{U_{S_r}}{U_{S_i}}(-\sin\phi) \quad , \tag{C.18a}$$

$$\frac{u^x}{U_{S_i}} = \cos\phi + \frac{U_{P_r}}{U_{S_i}}\cos\theta + \frac{U_{S_r}}{U_{S_i}}\cos\phi \quad . \tag{C.18b}$$

Dividing equations C.9a and C.9b by U_{S_i}:

$$\frac{2\mu}{V_S}\left(-1 - \frac{U_{S_r}}{U_{S_i}}\right)(\cos\phi\sin\phi) + \frac{1}{V_P}\frac{U_{P_r}}{U_{S_i}}\left(2\mu\cos^2\theta + \lambda\right) = 0 \tag{C.19a}$$

$$\left(1 - \frac{U_{S_r}}{U_{S_i}}\right)\frac{\mu}{V_S}\left(1 - 2\cos^2\phi\right) + \frac{\mu}{V_P}\frac{U_{P_r}}{U_{S_i}}(2\sin\theta\cos\theta) = 0 \tag{C.19b}$$

After some algebra, the unit reflected S-wave amplitude is:

$$\frac{U_{S_r}}{U_{S_i}} = \frac{-4\mu(\cos\phi\sin\phi)(\sin\theta\cos\theta) - (2\mu\cos^2\theta + \lambda)(1 - 2\cos^2\phi)}{4\mu(\cos\phi\sin\phi\sin\theta\cos\theta) + (2\mu\cos^2\theta + \lambda)(2\cos^2\phi - 1)} \tag{C.20}$$

Analogously it is obtained the reflected P amplitude, using equations C.19:

$$\frac{U_{P_r}}{U_{S_i}} = \frac{V_S}{V_P}\frac{4\mu(\cos\phi\sin\phi)(2\cos^2\phi - 1)}{4\mu(\cos\phi\sin\phi\sin\theta\cos\theta) + (2\mu\cos^2\theta + \lambda)(2\cos^2\phi - 1)} \tag{C.21}$$

Replacing C.20 and C.21 in C.18a and simplifying:

$$\frac{u^z}{U_{S_i}} = \frac{4\mu\cos\phi\sin\phi\cos\theta\left[2\sin\phi\sin\theta + V_P/V_S\,(2\cos^2\phi - 1)\right]}{4\mu(\cos\phi\sin\phi\sin\theta\cos\theta) + (2\mu\cos^2\theta + \lambda)(2\cos^2\phi - 1)} = R_S^z \tag{C.22}$$

Analogously, replacing C.20 and C.21 in C.18b and simplifying:

$$\frac{u^x}{U_{S_i}} = \frac{2\cos\phi(2\cos^2\phi - 1)\left[2\mu V_P/V_S\sin\phi\sin\theta + (2\mu\cos^2\theta + \lambda)\right]}{4\mu(\cos\phi\sin\phi\sin\theta\cos\theta) + (2\mu\cos^2\theta + \lambda)(2\cos^2\phi - 1)} = R_S^x \tag{C.23}$$

Equations C.22 and C.23 correspond to the free surface coefficients for the S-wave incidence.

Using the following identities:

$$V_P^2 = \frac{\lambda + 2\mu}{\rho}, \quad V_S^2 = \frac{\mu}{\rho}, \quad p = \frac{\sin\theta}{V_P} = \frac{\sin\phi}{V_S} \quad \text{and} \quad \cos^2\theta + \sin^2\theta = 1\,,$$

the following useful relations result:

$$\mu = \rho V_P^2, \quad \lambda = \rho(V_P^2 - 2V_S^2),$$

$$\sin\theta = pV_P, \quad \sin\phi = pV_S\,,$$

$$\cos\theta = \sqrt{1 - p^2V_P^2}\,, \quad \cos\phi = \sqrt{1 - p^2V_S^2}.$$

These relations allow to obtain the free surface response equations as a function of velocities V_P and V_S, and the angles of incidence and reflection:

$$R_P^Z = \frac{(V_P^2 - 2V_S^2(1-\cos^2\theta))\,(-2\cos\theta(2\cos^2\phi - 1) - 4\,(V_S/V_P)\sin\theta\cos\theta\sin\phi)}{4V_S^2\sin\theta\cos\theta\sin\phi\cos\phi + (2\cos^2\phi - 1)\,(V_P^2 - 2V_S^2(1-\cos^2\theta))} \quad \text{(C.26a)}$$

$$R_P^X = \frac{4\sin\theta\cos\theta\sin\phi\,(2V_S^2\sin\theta\sin\phi + (V_S/V_P)\,(V_P^2 + 2V_S^2(1+\cos^2\theta)))}{4V_S^2\sin\theta\cos\theta\sin\phi\cos\phi + (2\cos^2\phi - 1)\,(V_P^2 - 2V_S^2(1-\cos^2\theta))} \quad \text{(C.26b)}$$

$$R_S^Z = \frac{4V_S^2\cos\phi\sin\phi\cos\theta\,(2\sin\theta\sin\phi + (V_P/V_S)\,(2\cos^2\phi - 1))}{4V_S^2\sin\theta\cos\theta\sin\phi\cos\phi + (2\cos^2\phi - 1)\,(V_P^2 - 2V_S^2(1-\cos^2\theta))} \quad \text{(C.26c)}$$

$$R_S^X = \frac{2\cos\phi(2\cos^2\phi - 1)((2V_SV_P\sin\phi\sin\theta) + (V_P^2 - 2V_S^2(1-\cos^2\theta)))}{4V_S^2\sin\theta\cos\theta\sin\phi\cos\phi + (2\cos^2\phi - 1)\,(V_P^2 - 2V_S^2(1-\cos^2\theta))} \quad \text{(C.26d)}$$

Equivalently, they can be defined as a function of the velocities V_P and V_S and the slowness p (see equations 4.6).

C.2 The rotation of recorded data for a sloping free surface

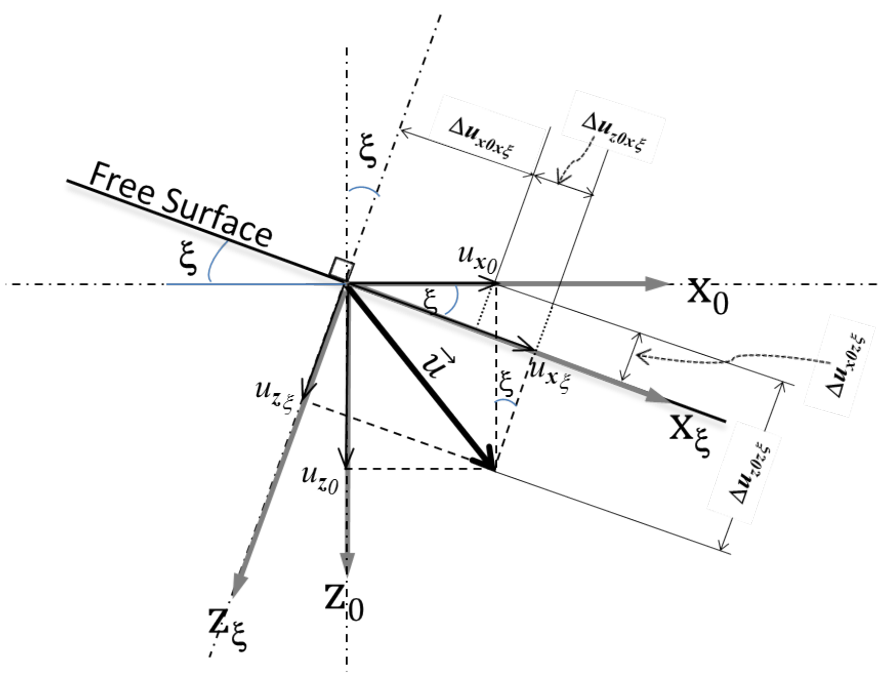

Figure C.2: [Free surface effect: rotation of a seismic displacement vector detected by vertical and horizontal sensors to the surface normal coordinate axes.

Figure C.2 shows the relation between the recorded data, in coordinates horizontal and vertical x_0 and z_0, and the data in coordinates normal to the surface x_ξ and z_ξ. The following relations for the rotated coordinates can be obtained from the figure:

$$u_{x_\xi} = \Delta u_{z_0 x_\xi} + \Delta u_{x_0 x_\xi} \quad \text{and} \quad u_{z_\xi} = \Delta u_{z_0 z_\xi} - \Delta u_{x_0 z_\xi}$$

where

$$\frac{\Delta u_{z_0 x_\xi}}{u_{z_0}} = \sin\xi \quad , \quad \frac{\Delta u_{x_0 x_\xi}}{u_{x_0}} = \cos\xi \quad , \quad \frac{\Delta u_{z_0 z_\xi}}{u_{z_0}} = \cos\xi \quad \text{and} \quad \frac{\Delta u_{x_0 z_\xi}}{u_{x_0}} = \sin\xi \quad .$$

Therefore

$$u_{x_\xi} = u_{x_0} \ \cos\xi + u_{z_0} \ \sin\xi \tag{C.27}$$

$$u_{z_\xi} = u_{x_0} \ (-\sin\xi) + u_{z_0} \ \cos\xi \tag{C.28}$$

.

Appendix D

Finite difference modeling with topography

Among the seismic wave modeling techniques, finite difference has shown great accuracy and computational efficiency. The code used for modeling is based on an elastic isotropic 2-D Finite-difference algorithm with the staggered grid approach, due to Levander (1988).

The code is implemented using the 2-D equations of motion and the constitutive laws for an isotropic medium, such that only first order derivatives are required. The 2-D elastic equations of motion in the cartesian plane (see section A.1.2) are:

$$\rho\frac{\partial \dot{u}_x}{\partial t} = \frac{\partial \sigma_{xx}}{\partial x} + \frac{\partial \sigma_{xz}}{\partial z} \tag{D.1}$$

$$\rho\frac{\partial \dot{u}_z}{\partial t} = \frac{\partial \sigma_{zz}}{\partial z} + \frac{\partial \sigma_{xz}}{\partial x} \tag{D.2}$$

where the dot means time derivative, namely,

$$\dot{u}_x = \frac{\partial u_x}{\partial t} \quad \text{, that is to say} \quad \frac{\partial^2 u_x}{\partial t^2} = \frac{\partial \dot{u}_x}{\partial t} \quad .$$

The constitutive equations are:

$$\begin{aligned}
\sigma_{xx} &= (\lambda + 2\mu)\frac{\partial u_x}{\partial x} + \lambda\frac{\partial u_z}{\partial z} \\
\sigma_{zx} &= \mu\left(\frac{\partial u_x}{\partial z} + \frac{\partial u_z}{\partial x}\right) \\
\sigma_{zz} &= (\lambda + 2\mu)\frac{\partial u_z}{\partial z} + \lambda\frac{\partial u_x}{\partial x}
\end{aligned}$$

which can be derived with respect to time,

$$\dot{\sigma}_{xx} = (\lambda + 2\mu)\frac{\partial \dot{u}_x}{\partial x} + \lambda\frac{\partial \dot{u}_z}{\partial z} \tag{D.3}$$

$$\dot{\sigma}_{xz} = \mu\left(\frac{\partial \dot{u}_x}{\partial z} + \frac{\partial \dot{u}_z}{\partial x}\right) \tag{D.4}$$

$$\dot{\sigma}_{zz} = (\lambda + 2\mu)\frac{\partial \dot{u}_z}{\partial z} + \lambda\frac{\partial \dot{u}_x}{\partial x} \tag{D.5}$$

Equations D.1 to D.5 define a coupled system, which can be solved numerically.

These differential equations are casted as finite differences, using regular discrete sampling in time and space. After noticeable practical experience and theoretical developments, it has been found that a *staggered grid* approach, using a 4th order differential approximation in space and 2nd order differential approximation in time, qualifies as highly accurate and efficient (Levander, 1988). Hayashi et al. (2001) provides additional capabilities such as surface topography, variable grid size and viscoelastic attenuation. From them just the surface topography is considered in the following.

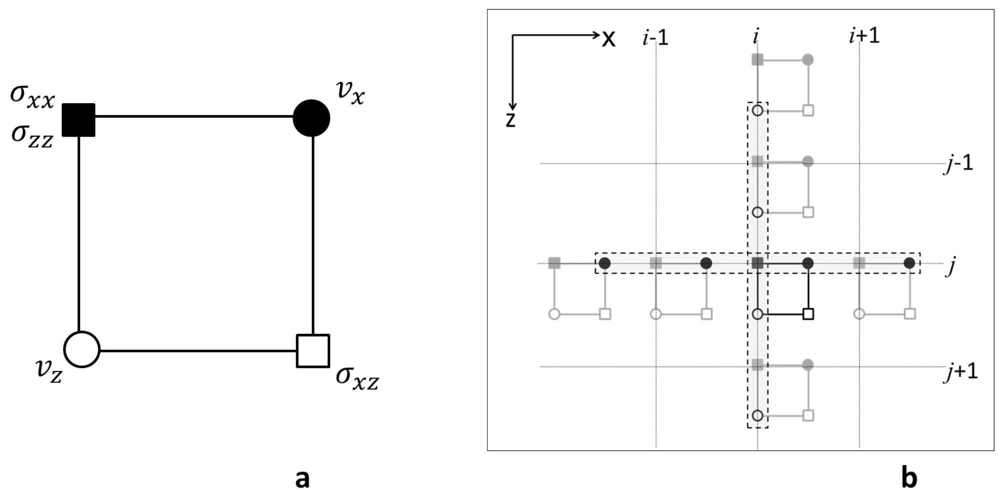

Figure D.1: The staggered grid stencil used for the elastic Finite Differences method. (a) Definition of the discrete derivatives at a grid location. (b) The derivative stencil in the staggered grid: example for the σ_{zz} calculation.

The staggered grid is illustrated in figure D.1. Figure D.1a shows the relative location in space of the finite difference data. The calculation of a new differential data is illustrated by figure D.1b, using the vertical normal stress σ_{zz} as an example. The subindex i corresponds to the x-coordinate axis and j to the z-coordinate. It is defined a *stencil* for the velocity derivatives to calculate the stress σ_{zz}. We can define a discrete approximation for the particle strain velocity in x as

$$\frac{\partial \dot{u}_x}{\partial x} \approx D_x v_x$$

which approximated as a 4th order finite difference in space is:

$$D_x v_x \mid_{i,j} = \frac{1}{\Delta x}\left[c_0\left(v_x \mid_{i+1/2,j} - v_x \mid_{i-1/2,j}\right) - c_1\left(v_x \mid_{i+3/2,j} - v_x \mid_{i-3/2,j}\right)\right] \tag{D.6}$$

where $c_0 = 9/8$ and $c_1 = 1/24$, obtained by a Taylor Series approximation (Levander, 1988). The symbol '$|_n$' means "evaluated at n". An analogous equation defines $D_z v_z$.

The σ_{zz} stress difference approximation, according to equation D.5, and standing k for the time sample, is:

$$\sigma_{zz} \mid_{i,j}^{k+1} = \sigma_{zz} \mid_{i,j}^{k} + \Delta t\left[(\lambda + 2\mu) D_z v_z \mid_{i,j} + \lambda D_x v_x \mid_{i,j}\right] \tag{D.7}$$

Therefore, after replacing equation D.6 and its analogous for $D_z v_z$ into equation D.7, the stencil illustrated in Figure D.1b is completed, and $\sigma_{zz} \mid_{i,j}^{k+1}$ can be solved. Analogously all the equations are solved to obtain the wavefield at each location, therefore a forward step in time for all the elastic wavefield.

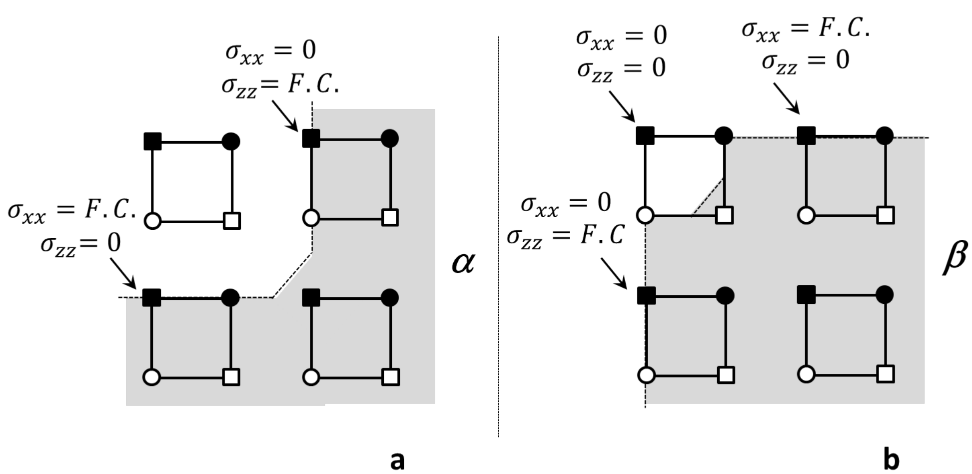

Figure D.2: The topography grid used for the elastic Finite Differences method. (a) inner corner or α and (b) outer corner or β. The gray color identifies the solid medium and the white color the air. *F. C.* indicates "free surface condition".

The free surface with topography is defined by Hayashi et al. (2001) based in the location of the stencil with respect to a grid *corner*, as illustrated in figure D.2. The purpose is to keep the stresses condition at the free surface, namely null stress in the surface, normal or shear (see Appendix C). Two corner types are defined, identified as the inner corner or α and the outer corner or β. Only the σ_{zz} and σ_{xx} of the outer corners are set to zero. The velocities are set to zero out of the solid. The σ_{xz} in the boundary are calculated like in the model interior. *F.C.* indicates the "free surface condition", whose normal stresses perpendicular to the boundary are set to zero, and normal stresses parallel to the boundary are updated using velocity derivatives parallel to the boundary.

Appendix E

The *Tau-p* Transform

The *Tau-p* transform is the application to the seismic method of the *Radon transform*, a reversible mathematical operation that allows one to obtain a function from its projections (Deans, 1983). This tool has been applied to many fields such as medicine, electron microscopy, image processing, and astronomy.

In seismic data processing it is known as the *Tau-p* transform or *Slant Stack*. It works on a seismic gather, namely a function in time-space coordinates, $u(t, x)$, corresponding to seismic traces recorded on the surface. The projections are lines of common slope in $t - x$, identified as the horizontal slowness (or ray parameter) known as p. The slope p is defined as:

$$p = \frac{\sin\theta}{V} = \frac{\Delta t}{\Delta x} \tag{E.1}$$

where θ is the angle of incidence to the surface, V is the velocity, Δt is the differential arrival time between two space locations, and Δx is the distance between the two space locations (see figure 4.5a).

Following Robinson (1982), the Radon transform involves summing all the amplitudes $u(t, h)$ along a given line of slope p_0 (a *slant stack*), which intercepts the axis $x = 0$ at τ_0, and plots the result at the corresponding point (τ_0, p_0) on the p, τ plane. That is to say, it transforms a line to a point, without losing any information, since a line is completely described by its intercept and slope. It has been shown that the *Tau-p* transform allows decomposin a seismic data field into plane waves (Treitel et al., 1982).

The *Tau-p* Transform of the seismic gather $u(t, h)$ is expressed by the equation

$$\hat{u}(\tau, p) = \int_{-\infty}^{\infty} u(\tau + px, x)\mathrm{d}x; \tag{E.2}$$

the inverse *Tau-p* transform, following Claerbout (1985), is expressed as

$$u(x,t) = \rho(t) * \int_{-\infty}^{\infty} \hat{u}(t - px, p)\mathrm{d}p, \tag{E.3}$$

where $*$ denotes *convolution* and $\rho(t)$ is a filter[1],

The $Tau{-}p$ transform following the previous definitions show some shortcomings, such as the asymmetry of the inverse transform, and the uneven sampling generated by the distance variation between samples, as the space variable increases for a range of slopes (Margrave, 2007). Methods to obtain more accurate (and efficient) calculations have been developed, as follows.

The Fourier-transform domain allows carrying out the $Tau{-}p$ transform, according to the *Fourier-slice theorem* (Deans, 1983; Robinson, 1982), which says that the Fourier Transform of a linear projection (slice) of a 2-D function is the same as the Fourier Transform of the function evaluated at an angle corresponding to the slice direction.

Thus, we evaluate the FT of $u(t,x)$ along a projection, the line $\omega = k_x/p$, which is the same as saying $k_x = p\omega$, then:

$$U(p\omega,\omega) = \int_{-\infty}^{\infty}\int_{-\infty}^{\infty} u(t,x)e^{-i(p\omega x - \omega t)}\mathrm{d}x\mathrm{d}t$$

A change of variable, $\tau = t - px$, results in

$$U(p\omega,\omega) = \int_{-\infty}^{\infty} e^{i\omega\tau}\left[\int_{-\infty}^{\infty} u(\tau + px, x)\mathrm{d}x\right]\mathrm{d}\tau = \int_{-\infty}^{\infty} e^{i\omega\tau}\hat{u}(\tau,p)\mathrm{d}\tau$$

The expression between brackets is the Radon Transform in the time domain (equation E.2), therefore, $U(p\omega,\omega)$ is the Fourier transform of the $Tau - p$ transform.

A least squares solution, known as the Discrete Radon Transform (Beylkin, 1987) has allowed to develop efficient calculation methods. Following Mosher et al. (1996) and Marfurt et al. (1996), the inverse Radon transform is

$$u(\omega,x) = \underset{\sim}{\mathcal{R}}^H(\omega,p,x)U_R(\omega,p) \tag{E.4}$$

[1]Using an explicit expression for the $\rho(t)$ filter, equation E.3 is $u(x,t) = \frac{d}{dt}H_i\int_{-\infty}^{\infty}\hat{u}(t-px,p)\mathrm{d}p$ where H_i denotes the Hilbert transform (Robinson, 1982).

where $\underset{\sim}{\mathcal{R}}$ is a matrix operator with discrete elements defined by

$$R_{jk} = e^{i\omega p_j x_k} \tag{E.5}$$

and the $Tau - p$ transform can be obtained by

$$U_R(\omega, p) = [\underset{\sim}{\mathcal{R}}^H \underset{\sim}{\mathcal{R}}]^{-1} \underset{\sim}{\mathcal{R}}^H u(\omega, x) \tag{E.6}$$

where the exponents $\mathcal{A}^H$ means the transpose conjugate matrix, and $\mathcal{A}^{-1}$ means the inverse of matrix $\mathcal{A}$.